6

Shock Ignition of Particles

S.M. Frolov and A.V. Fedorov

6.1 Introduction

Ignition and combustion of fine solid particles and liquid fuel drops ("particles," for short) are important issues for various branches of science and technology, such as aerospace and chemical technologies, chemical propulsion, ground transportation, and industrial safety. These issues were noticed by numerous researchers both at the end of the foregoing century and presently, and many relevant publications are available. Detailed reviews of the current status of the research can be found elsewhere [1–5].

Particle ignition and combustion are phenomena comprising all the main constituents of the combustion process; namely, fast exothermic chemical reactions complicated by diffusion of reactants and products, thermal energy deposition and spreading of heat in the medium, and convective flows. The classical theory implies that particle combustion is diffusion-limited and therefore chemical kinetic aspects are usually not considered in the analysis [6–15]. In addition, the classical theory considers an isolated particle in an unconfined state. Within these presumptions, notable progress in understanding relevant physical and chemical processes has been achieved recently. However, for problems dealing with transient modes of combustion, such as ignition or extinction, it is necessary to consider the effects of finite-rate chemical kinetics. Moreover, in practice, particle ignition and combustion occur in the presence of neighboring particles or confinement surfaces. The corresponding effects are usually referred to as "spray" (or "collective") and "confinement" effects.

Spray effects manifest themselves in two-phase reactive flows. In existing computational approaches, chemical reaction rates are determined by considering particles as distributed mass, momentum, and energy sources. As a matter of fact, spray ignition and combustion phenomena are a complex combination of chemical kinetics and diffusion-controlled flames around individual particles, their groups, and gas-phase partially premixed flames.

F. Zhang (ed.), *Shock Wave Science and Technology Reference Library: Heterogeneous Detonation*, DOI: 10.1007/978-3-540-88447-7_6,

For modeling ignition and combustion of particles in sprays and clouds, several approaches are used by analyzing the evolution of (1) two or more particles [16, 17], (2) a regular sequence of particles [18, 19], (3) a group of chaotically distributed particles [20, 21], or (4) a particle suspension [22]. Advantages and drawbacks of these approaches are discussed elsewhere [2–7]. Note that only the most detailed description of the flow fields in the space between particles has been obtained in the analysis of two interacting particles and the linear array of particles. "Group" and "suspension" theories do not take into account transient heat and mass transfer processes in the particle vicinity, nor the dependence of the rates of these processes on the distance between particles.

At present, ignition and combustion of particles in combustion chambers are modeled without regard for many factors affecting both local and integral combustor performance. Dynamic and thermal effects of particles on the flow are modeled in terms of the averaged interphase mass, momentum, and energy fluxes [22]. The effect of turbulence on phase interaction is modeled by turbulent dispersion of particles [5]. Mixing of gas-phase species (vapors and reaction products) is modeled by micromixing models which do not account for the difference in species diffusion coefficients. Finite instantaneous depths of penetration of heat and diffusion fluxes from each individual particle are also not taken into account. As a matter of fact, in computational algorithms, the increments of thermal energy and gas-phase species mass arising from particle or drop ignition and combustion are smeared uniformly throughout a corresponding computational cell, which is usually several orders of magnitude larger than the characteristic particle size. As a consequence, gas-phase chemical processes (intrinsically local) are treated as volumetric processes. In view of this, computational cell size becomes an important artificial parameter of a solved problem. Its value determines the dynamics of the local and integral phenomena studied. However, particles are known to be surrounded by finite-dimensional spatial regions with highly nonuniform distributions of temperature and species concentrations. The dimensions of such regions depend on time and the instantaneous mutual position of neighboring particles. In such conditions, preignition processes as well as ignition and combustion cannot be considered as processes in a well-stirred reactor represented by a computational cell.

In this chapter we concentrate on fundamental issues of shock-induced particle and drop ignition and provide an overview of the problems of adequate mathematical modeling of relevant phenomena. Subsequent stages of ignition process development (combustion, extinction, etc.) are beyond the scope of this chapter. As examples of solid particles, magnesium and aluminum are mainly considered. Their oxidation rates either depend on the oxide film thickness (aluminum) or are independent of it (magnesium). As examples of liquid fuel drops, single-component n-alkane drops are considered.

6.2 Ignition of Solid Particles

6.2.1 Experimental and Theoretical Findings

Ignition of solid particles in a high-temperature gas flow behind a shock wave propagating in a gas–particle suspension was studied experimentally elsewhere [23–47]. Figure 6.1 shows a typical schematic of experimental conditions in a shock tube [46, 47]: before firing; after firing, but before the shock wave has reached the end wall; and after shock wave reflection. In the experiments on particle ignition behind the incident shock wave, region 2 is the test region. If particle ignition is studied behind the reflected shock wave, region 5 serves as the test region. Pressure and temperature in regions 2 and 5 are set by adjusting the initial conditions in the driver (region 4) and driven sections (region 1) of the shock tube before firing and by monitoring the shock wave velocity along the tube in the course of the experiments. To estimate the conditions in the experiments, ideal compressible gas relations and Rankine–Hugoniot relationships are usually used.

The shock tube can be either vertical or horizontal. Vertical shock tubes have the advantage of creating dust suspensions, which are homogeneous in tube cross section. However, gravitational dust sedimentation can lead to dust density variation along the tube. To avoid the effect of sedimentation, various dust dispersion techniques are used. For example, in [24, 32, 37, 47], it was reported that dust powders were mounted on a horizontal shelf or knife blade, at a short distance from the end wall. The incident shock wave swept over the particles, entraining them in the postshock flow and thus creating

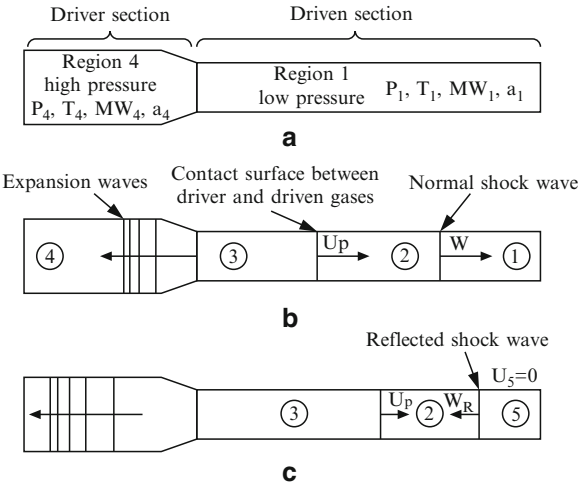

Fig. 6.1. Typical experimental conditions in a shock tube [46, 47]: **a** before firing of the tube; **b** after firing, but before reflection of the incident shock wave; and **c** after reflection of the incident shock wave from the end wall

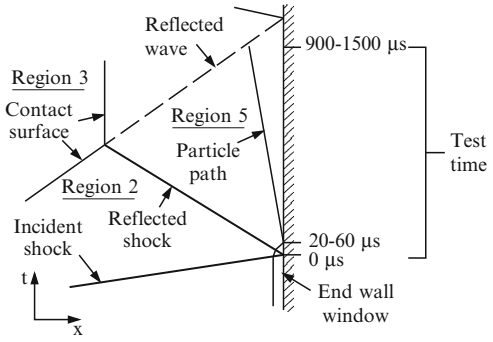

Fig. 6.2. Flow field in time (t)–distance (x) coordinates near the shock-tube end wall showing flow interactions and particle position versus time [46, 47]

a particle suspension. After the shock wave had been reflected off the end wall, the particles in suspension were heated and ignited if the temperature, pressure, and composition conditions behind the reflected shock wave were appropriate for ignition.

Figure 6.2 shows a typical flow field wave diagram for the shock tube near the end wall, with axial position on the horizontal axis and time on the vertical axis [46, 47]. The incident shock wave first approaches and is then reflected from the end wall, positioned on the right side of the x-axis. Then the reflected shock wave moves away from the end wall until it reaches the contact surface, which is moving toward the end wall at the same velocity as the gas in region 2. Through this interaction, a normal shock is transmitted through the contact surface, moving away from the end wall, and a shock wave, Mach wave, or expansion wave, depending on the thermodynamic properties of the gases in regions 2 and 3, is reflected back toward the end wall. This wave then returns to the end wall and is reflected from it, ending the test period. The gas in region 5 is a stagnant, hot, high-pressure mixture in which solid particles are ignited. Thus, the test time is the time between the arrival of the incident shock wave at the end wall and the arrival of the wave reflected from the contact surface at the drifting particles. In experiments [46, 47], the test time ranged from 900 to 1,500 μs.

The experimental data on the ignition delay time $t_{\rm ign}$ as a function of the initiating shock wave Mach number M_0 are available for various metals – volatile (magnesium, zinc, etc.), intermediate (aluminum, iron, copper, lead, titanium, hafnium, etc.), and refractory (tantalum, tungsten, niobium), nonmetallic inorganic elements (boron, silicon, carbon, etc.), various organic dusts (cornstarch, wheaten flour, etc.), and monopropellants and high explosives (RDX, TNT, etc.).

For a suspension of magnesium particles of mean initial radius $r_{\rm s0} = 17\,\mu$m, the dependence of $t_{\rm ign}$ on postshock temperature T_0 was obtained, for example,

in [27]. At temperatures $T_0 = 1{,}538$–$2{,}500\,\mathrm{K}$, the ignition delay time of magnesium particles varied from 0.1 to 0.05 ms.

For a suspension of fine aluminum particles ($r_{s0} = 5$–$10\,\mu\mathrm{m}$), the t_{ign} versus T_0 dependence was obtained, for example, in [47]. Aluminum particles were ignited in atmospheres consisting of argon and various amounts of H_2O, CO_2, and O_2 at the end wall of a shock tube. At pressures and temperatures of about 0.85 MPa and 2,600 K, the measured ignition delays were in the range from 150 to 900 μs. Interestingly, aluminum particles ignited in a mixture of H_2O/Ar showed ignition delay times 3–6 times greater than those from CO_2/O_2/Ar mixtures.

In the literature, there are still inconsistencies in available experimental data. For example, in some experimental studies the ignition delays were found to reduce when the measurements were made behind the reflected shock wave rather than behind the incident shock wave [36, 37]. In other studies (e.g., [30, 34, 35, 41]) some dusts were more easily ignited behind the incident shock wave than behind the reflected shock wave.

Experimental studies of combustion of various metal particles [48–58] indicate the important role of heterogeneous reactions. It is known that during the oxidation of metal particles in a gaseous oxidizer, an oxide film separates the metal and the oxidizer. The rate of reaction is then governed by the protective properties of this film. In [8, 9], this implication was used to model ignition of individual metal particles in a high-temperature oxidizing atmosphere. Particle ignition was found to occur owing to thermal breakdown, when the rate of heat evolution during oxidation becomes larger than the rate of heat removal from the particle surface.

Ignition of volatile metals, owing to their low boiling points (about 1,360 K for Mg), can occur in a vapor phase according to [6]. However, metal oxide layers were always observed on the surface of particles, which indicates the significance of heterogeneous reactions during ignition [55–58]. Ignition of boron particles is inhibited by a thin layer of B_2O_3 on the particle surface, and the high vaporization temperature of boron (about 4,100 K) limits oxidation to slower heterogeneous surface reactions.

There exist a number of theoretical models of particle ignition [59–84]. In most of the models, the metal particle ignition law is represented in the form of an Arrhenius expression with certain values of the preexponential factor K in the oxide film growth rate and the activation energy E of the oxidation process. These kinetic constants are found by fitting experimental and theoretical dependencies of t_{ign} on M_0.

The models differ considerably in their predicting capabilities. For example, the values of t_{ign} predicted in [62] appeared to be an order of magnitude larger than the values measured in dynamic conditions behind a shock wave [27]. The authors of [72–77] found the values of K and E for the dynamic model of particle ignition in the flow behind a propagating shock wave. They took particle motion and low-temperature oxidation into account. The resultant values of K and E appeared to be different from those in the static

ignition model, which does not account for the relative motion of solid particles and gas.

A simple estimate for the particle velocity relaxation time, $\tau_{\rm vel}$, in the gas flow using the Stokes law $\tau_{\rm vel} = (2/9)\rho_{\rm s} r_{\rm s0}^2/\mu$ shows that at $r_{\rm s0} = 1$ and $5\,\mu$m, $\tau_{\rm vel} = 0.02$ and 0.5 ms, respectively. Here, $\rho_{\rm s}$ is the particle material density and μ is the gas viscosity. According to the ignition delay data [63], the effect of velocity relaxation for fine particles may be insignificant at low flow velocities. The velocity of very fine particles rapidly achieves the ambient gas velocity, and the heating conditions quickly become similar to those in a quiescent atmosphere. Besides the differences in K and E values at static and dynamic conditions, there is also a considerable scatter in the values of the determining parameters in available mathematical models of particle ignition. As a result, the constants in the models differ considerably, sometimes by orders of magnitude; therefore, it is worth discussing these problems, first for the example of metal particle ignition in static conditions.

In general, all mathematical models of metal particle ignition in the quiescent atmosphere are based on two approaches [59–71]. The first approach applies the thermal explosion theory developed by Semenov. The second is based on the "reduced film" concept. The critical analysis of these approaches [78] resulted in the following findings:

1. Two unknown constants, K and E, in the models are determined from experimental dependencies at essentially different conditions. In [59, 60], they were found for small values of $r_{\rm s0}$ based on the critical "breakdown" temperature of a liquid magnesium particle. In [65, 66], they were found for large values of $r_{\rm s0}$ for solid magnesium particles. As a result, the values of the constants in these papers are different.
2. Only models based on the second approach contain information on the dependence of the medium critical temperature on oxygen concentration and particle radius as well as the dependence of the ignition delay time on the particle radius.
3. None of the papers cited contain a qualitative study of the solutions of the corresponding Cauchy problem for the models using the first approach or the corresponding boundary-value problem for the models using the second approach. Mathematical issues such as solvability of governing transcendental equations for determining K and E were not addressed. Moreover, no comparison of the data on the temperature growth dynamics by different models has been made [78].

6.2.2 Static Conditions

6.2.2.1 General Mathematical Model

Consider a metal particle placed in a hot flow of oxidizing gas. It is assumed that an exothermic oxidation reaction and an endothermic phase transition

(melting, vaporization, etc.) take place on the particle surface. The particle is assumed to occupy region Ω in the space with Cartesian coordinates (x_1, x_2, x_3). The mathematical model governing the evolution of the temperature field in the particle is based on the energy conservation equation [85]

$$c_s \rho_s \frac{\partial T}{\partial t} = \lambda_s \Delta T, \quad t > 0, \quad (x_1, x_2, x_3) \in \Omega \subset R^3 \tag{6.1}$$

supplemented with the initial condition

$$t = 0: \quad T = T_0(x_1, x_2, x_3), \tag{6.2}$$

boundary conditions on the reactive particle surface $\Gamma_1 \subset \partial\Omega$

$$(x_1, x_2, x_3) \in \Gamma_1: \quad \lambda_s \frac{\partial \mathrm{T}}{\partial n} = Q_{\mathrm{chem}} - Q_{\mathrm{conv}} - Q_{\mathrm{phase}}, \tag{6.3}$$

and symmetry condition on the internal surface $\Gamma_2 \subset \partial\Omega$

$$(x_1, x_2, x_3) \in \Gamma_2: \quad \frac{\partial T}{\partial n} = 0. \tag{6.4}$$

To complete the statement of the problem one has to specify source terms in (6.3) as well as the metal oxidation kinetics. The latter is usually expressed in the form of an additional differential equation

$$\frac{\mathrm{d}h}{\mathrm{d}t} = \varphi(h, T) \tag{6.5}$$

with the corresponding initial condition. In (6.1)–(6.5), t is time, $T = T(x_1, x_2, x_3, t)$ is the particle temperature, $h = h(t)$ is the oxide film thickness, $\Delta \equiv \partial^2/\partial x_1^2 + \partial^2/\partial x_2^2 + \partial^2/\partial x_3^2$ is the Laplace operator, $\partial\Omega$ is the boundary of region Ω, ∂n is the element of the normal vector to the particle surface, c is the specific heat, λ is the thermal conductivity, φ is a function, and indices s and 0 relate to particle material and initial conditions, respectively. Equation (6.3) includes source terms corresponding to heat fluxes between the particle and ambient medium owing to convective heat transfer, Q_{conv}, heterogeneous chemical reaction, Q_{chem}, and phase transition, Q_{phase}. The generalized model of (6.1)–(6.5) can be simplified in some particular cases.

6.2.2.2 Point Model of Particle Ignition without Metal Vaporization

Assume that a solid particle is spherical and the temperature field in it is uniform. For the sake of argument, consider a magnesium particle. Then, averaging (6.1)–(6.4) over the particle volume, one obtains the following heat balance equation:

$$\frac{4}{3}\pi r_s^3 c_s \rho_s \frac{\mathrm{d}T}{\mathrm{d}t} = 4\pi r_s^2 q \rho_{\mathrm{ox}} \frac{\mathrm{d}h}{\mathrm{d}t} - 4\pi r_s^2 \frac{\lambda Nu}{2r_s}(T - \tilde{T}). \tag{6.6}$$

The kinetic equation (6.5) can be expressed in the form

$$\frac{\mathrm{d}h}{\mathrm{d}t} = k_0 C_{\mathrm{ox}} \psi(T) \exp(-E/RT). \tag{6.7}$$

In (6.6) and (6.7), q is the chemical reaction heat related to metal oxide mass, ρ_{ox} is the metal oxide density, Nu is the Nusselt number determined as $Nu = 2.0 + 0.5\,Re^{0.5}$ with the Reynolds number $Re = 2r_{\mathrm{s}}U\rho/\mu$ based on the relative velocity U of gas and the particle, $\tilde{T}$ is the ambient gas temperature, k_0 and E are the parameters in the empirical kinetic law for the oxide film growth, C_{ox} is the mass concentration of the oxidizer, $\psi(T)$ is a function, and R is the gas constant. To take into account thermal deceleration of oxidation at high temperatures comparable with the magnesium boiling temperature T_{m}, it is usually assumed that $\psi(T) = T_{\mathrm{m}} - T$. At considerably lower temperatures, $\psi(T) = 1$.

6.2.2.3 Point Model of Particle Ignition with Metal Vaporization

In the literature, there are some indications of the importance of metal and its oxide vaporization at the particle surface [77,86]. Mathematical models of this phenomenon are of interest for the general theory of thermal explosion in systems with two chemical reactions exhibiting different activation energies and characteristic times [87]. The model taking into account metal vaporization follows from (6.1)–(6.5) with a nonzero source term describing the phase transition, i.e., $Q_{\mathrm{phase}} \neq 0$. Within this model, particle temperature evolution is governed by the following equation [64]:

$$\frac{1}{3}\frac{c_{\mathrm{s}} r_{\mathrm{s}}}{qk}\frac{\mathrm{d}T}{\mathrm{d}t} = \exp(-E/RT) - c\exp(-L/RT) - \bar{\alpha}(T - \tilde{T}) \equiv g_1(T), \tag{6.8}$$

where $\bar{\alpha} = \lambda Nu/(2qr_{\mathrm{s}}\rho_{\mathrm{s}}k)$, $k = k_0 c_{\mathrm{ox}}$, $c = v/k$, and L and v are the latent heat and reference rate of metal vaporization.

6.2.2.4 Remarks on Point Models

In the models of particle ignition described in the previous sections, a number of simplifying assumptions are adopted which are not always justified.

For metal combustion the assumption of a spherically symmetric ignition process is usually adopted; however, experimental observations show that nonsymmetrical combustion modes also exist. The oxide layer possesses spherical symmetry only during the low-temperature induction phase of ignition. At high temperatures, the layer becomes nonuniform, which leads to the appearance of liquid "beads" and "caps" of oxide on the surface of the solid or liquid metal [84, 88]. It can therefore become necessary to refrain from making the assumption of spherical symmetry and to include symmetry-breaking conditions when modeling combustion of metal particles. The models which are in current use are lacking in this respect.

To calculate the heat flux to the particle surface, Newton's law of cooling $Q_{\text{conv}} = k_{\text{h}}\left(\tilde{T} - T\right)$, is applied with T treated as the mean particle temperature; however, Newton's law is known to be valid only for steady-state heat transfer and the consequences of its application to intrinsically transient problems of particle heating and ignition are not quite clear. Moreover, the heat flux is determined by the particle surface temperature T_{i} rather than the mean particle temperature. Thus, it is assumed that the thermal conductivity of particle material is infinitely large. However, this assumption can be violated when ignition of a relatively large particle of low-conductivity material is considered or when the chemical reaction rate at a particle surface is sensitive to the surface temperature. Therefore, for better representation of the generalized model of (6.1)–(6.5), the point models have to use some correction factors for Newton's law which would allow one to take into account the transient heat transfer of metal particles with gas and the nonuniform temperature distribution inside the particles.

The application of convective heat transfer correlations of the Ranz–Marshall type [89] for modeling heat fluxes between solid particles and gas under conditions of nonzero velocity slip in two-phase flows is also not fundamentally substantiated. Such correlations were derived from the measurements in steady-state flows and their use in transient two-phase flow conditions is questionable.

Regarding the overall kinetic law of particle ignition, it is usually derived by fitting the measured ignition delays and the results of calculations based on the standard particle ignition model with several unknown Arrhenius parameters (e.g., preexponential factor and activation energy). The Arrhenius parameters of the overall reaction rate constants are then found by applying the least-squares procedure. In view of the above assumptions adopted in the standard model of particle heating, the Arrhenius parameters thus obtained can appear to have little in common with the actual values relevant to the problem under consideration. There are many examples in the literature when the values of preexponential factors and activation energies determined for particular conditions of particle ignition (e.g., large samples of cubic or cylindrical geometry, etc.) were applied for other conditions (fine particles of spherical or flaked shape, thin filaments, etc.). In view of these implications, there is a need for reliable models of solid particle heating to provide the basis for improved modeling of particle ignition and combustion.

One of the promising approaches was reported by Avdeev et al. [90, 91], who derived the correction factors for Newton's law, which allow one to take into account the transient heat transfer of metal particles with gas and the nonuniform temperature distribution inside the particles. It was implied that these correction factors can modify the conditions of particle ignition in the oxidizer gas. The dynamics of metal particle heating in a quiescent gas was calculated using three models: (1) a detailed model based on the conjugate partial derivative equations of thermal conductivity in gas and particles, (2)

a standard point model based on the ordinary differential equation for the mean particle temperature T and Newton's law $Q_{\text{conv}} = k_{\text{h}}\left(\tilde{T} - T\right)$, and (3) a new point model, based on the ordinary differential equation for mean particle temperature T and Newton's law in the form $Q_{\text{conv}} = k_{\text{h,eff}}\left(\tilde{T} - T_{\text{i}}\right)$, where $k_{\text{h,eff}}$ is the effective heat transfer coefficient accounting for the transient particle heating. The approximate dependence of $k_{\text{h,eff}}$ on the governing parameters and time was derived from the analytical solution for a particle with constant surface temperature. The dependence of the surface temperature on the mean particle temperature $T_{\text{i}} = T_{\text{i}}(T)$ was determined by generalizing the results of numerical calculations based on the detailed model.

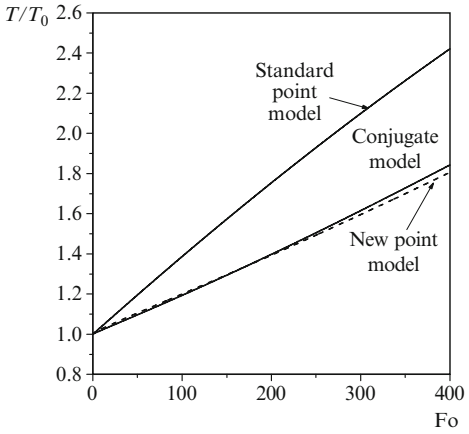

Fig. 6.3. Predicted time histories of aluminum particle heating in air at $\tilde{T}/T_0 = 5.46$ [90]

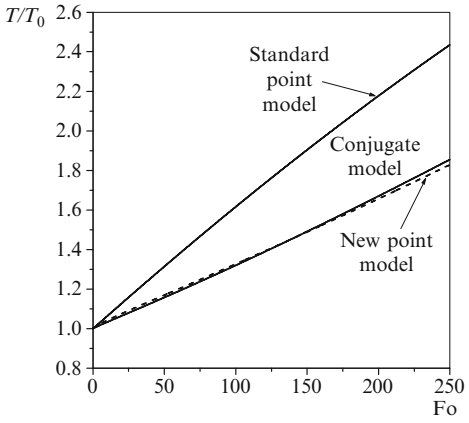

Fig. 6.4. Predicted time history of magnesium particle heating in air at $\tilde{T}/T_0 = 5.46$ [90]

Comparison of the computational results provided by the three models for aluminum, magnesium, boron, and iron particles showed that the new model correlates much better with the detailed model than the standard model. Figures 6.3 and 6.4 show some results of calculations in terms of the mean dimensionless particle temperature T/T_0 versus dimensionless time $Fo = \kappa t/r_{s0}$ for aluminum and magnesium particles predicted by different models.

The maximal deviations of the predicted mean particle temperature from the solution of the conjugate problem were less than 1–2% for the new model and up to 30% for the standard point model. The largest deviations were obtained for higher gas temperatures. The latter finding is particularly important for the problem of metal particle ignition in an oxidizer gas.

The important advantage of the model of Avdeev et al. [90, 91] is that it contains the particle surface temperature T_i, which may differ considerably from the mean temperature T. When solving a problem on particle ignition, the use of T_i instead of T may affect the process evolution in view of the strong dependence of the rate of a heterogeneous reaction on temperature.

6.2.2.5 Two Problems in Particle Ignition Theory

In the Sects. 6.2.2.6 and 6.2.2.7 some important issues are addressed dealing with the solution properties of the point models presented in Sects. 6.2.2.2 and 6.2.2.3. Using the elementary theory of catastrophes, analytical and numerical methods of solving ordinary differential equations, we consider:

1. The structure of catastrophe manifolds (CMs) of the point models and their correspondence to Semenov's critical conditions in the thermal explosion theory.
2. Solvability conditions of transcendental equations for determining parameters K and E. It is implied that there can be nonuniqueness in determining E at a given K.
3. Types of particle temperature histories.
4. Correspondence between particle ignition delay times provided by the models using the first and second approaches.

Consider a small magnesium particle placed into a quiescent gaseous atmosphere at temperature $\tilde{T}$. Within Semenov's model of thermal explosion, the equations of energy balance and oxide film growth kinetics for a particle of initial radius r_{s0} covered with an oxide film of thickness $h \ll r_s$ have the form of (6.6) and (6.7) [64, 68]:

$$mc_s \frac{dT}{dt} = -Sk_h(T - \tilde{T}) + Sq\rho_{ox}\frac{dh}{dt}, \quad \frac{dh}{dt} = K\,e^{-E/RT}, \tag{6.9}$$

where $\psi(T) = 1$ is assumed. In (6.9), k_h is the heat transfer coefficient, $S = 4\pi r_s^2$ is the particle surface area, and $m = (4/3)\pi\rho_s r_s^3$ is the particle

mass. For magnesium particles, $c_s = 1,100\,\mathrm{J\,(kg\ K)^{-1}}$, $\rho_s = 1,740\,\mathrm{kg\,m^{-3}}$, $q = 4.9 \times 10^7\,\mathrm{J\,kg^{-1}}$, and $\rho_{ox} = 3,600\,\mathrm{kg\,m^{-3}}$.

The solution of (6.9) should satisfy the following initial conditions:

$$T(0) = T_0,\ h(0) = h_0. \tag{6.10}$$

Thus, the evolution of particle temperature in the gas with $\tilde{T} > T_0$ is governed by the Cauchy problem of (6.9) and (6.10). The first term of (6.9) is the autonomous ordinary differential equation. It is sufficient to analyze the zero isoclinic line and determine the types of solution of this problem depending on some bifurcation parameters, for example, E, K, and $\tilde{T}$. In view of this, two problems should be solved.

The first problem is a direct problem formulated as follows:

Find the solution of the Cauchy problem (6.9) and (6.10), which is continuously differentiable together with its second derivative in the region $t \geq 0$.

The second problem belongs to the class of inverse problems and is formulated as follows:

Find the solution of the Cauchy problem (6.9) and (6.10) supplemented by some solvability condition with one (E) or two (E and K) unknown parameters such that one or two conditions relating these parameters are satisfied.

6.2.2.6 Direct Problem of Particle Ignition Without Vaporization

The qualitative properties of the direct problem solution can be studied using the methods of elementary catastrophe theory. In the dimensionless form, (6.9) governing particle ignition reads

$$\frac{\mathrm{d}T}{\mathrm{d}t} = \frac{T_{ox}}{t_1}\left(-\alpha(T - \tilde{T}) + \exp(-E/T)\right) \equiv g(T; \alpha, \tilde{T}),$$

where $T_{ox} = 3\xi q/(c_s T_a)$, $\alpha = \lambda Nu\, T_a/(2Kr_s\rho_s\xi q)$, and $t_1 = r_s/(Kt_a)$ are some constants; T_a and t_a are the reference values of temperature and time, and $\xi = \rho_{ox}/\rho_s$. Following [78, 92, 93], consider the zero isoclinic line of the equation as a surface in the space of parameters $(T_{ox}; \alpha, t_1)$. Consider the function $g(T; \alpha, \tilde{T})$ assuming that parameters α and $\tilde{T}$ are the control parameters. This enables one to construct the CM or the equilibrium surface in the $(T_{ox}; \alpha, t_1)$-space:

$$g(T; \alpha, \tilde{T}) = 0, \tag{6.11}$$

$$\frac{\mathrm{d}g}{\mathrm{d}T} = 0. \tag{6.12}$$

The system of (6.11) and (6.12) then allows determination of double-degenerate critical points (DCPs). If one supplements these equations with the equation

$$\frac{\mathrm{d}^2 g}{\mathrm{d}T^2} = 0 \tag{6.13}$$

and considers the solution of (6.11)–(6.13), then this solution determines triple-degenerate critical points (TCPs).

The solution of (6.11)–(6.13) can be found explicitly:

$$X(T;\alpha,\ \tilde{T}) = \left(\frac{E}{2};\ \frac{4}{E}\mathrm{e}^{-2},\ \frac{E}{4}\right) \equiv (T_*;\alpha_*,\ \tilde{T}_*).$$

The set of DCPs forms the curves of the following folds:

$$\alpha = \alpha_{\pm}(\tilde{T}) = \frac{\mathrm{e}^{-E/T_{\pm}}}{T_{\pm} - \tilde{T}}, \quad T_{\pm}(\tilde{T}) = \frac{E}{2}\left(1 \pm \sqrt{1 - \frac{4\tilde{T}}{E}}\right) \tag{6.14}$$

in the plane of control parameters $(\alpha, \tilde{T})$. Note that the condition $\tilde{T} = E/4$ corresponds to a cusp point, where $\alpha = \alpha_*$ and $T = T_{\pm} = T_*$. The separatrix on the plane of control parameters $(\alpha, \tilde{T})$ consists of the cusp point $(\alpha_*, \tilde{T}_*)$ and the fold curves (6.14). Note that DCPs of (6.11) and (6.12) on the fold curves (6.14) of the catastrophe surface (6.11) are the solutions of Semenov equations determining the thermal equilibrium breakdown. The curves $\alpha = \alpha_-(\tilde{T}, E)$ and $\alpha = \alpha_+(\tilde{T}, E)$ at the $(\alpha, \tilde{T})$-plane correspond to the ignition and extinction limits, respectively.

To describe ignition of a particle with $\tilde{T} > T_0$ one has to solve the Cauchy problem (6.9) and (6.10). The following analysis of qualitative features of the solution provides the information on the particle ignition criterion [61]. The ignition time is often determined in the literature as the time taken for the rate of particle temperature variation $\dot{T} = \mathrm{d}T/\mathrm{d}t$ or $g(T)$ to attain the maximum value.

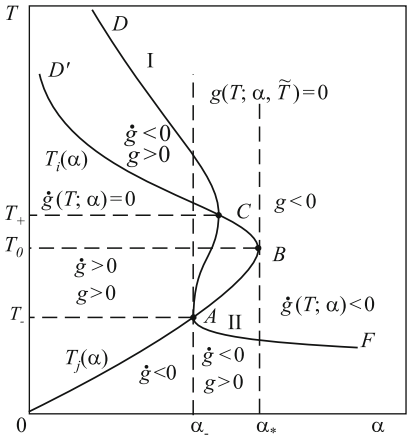

Fig. 6.5. Qualitative shape of ignition manifold in section $\tilde{T} = \text{const}$ $(\tilde{T} < E/4)$

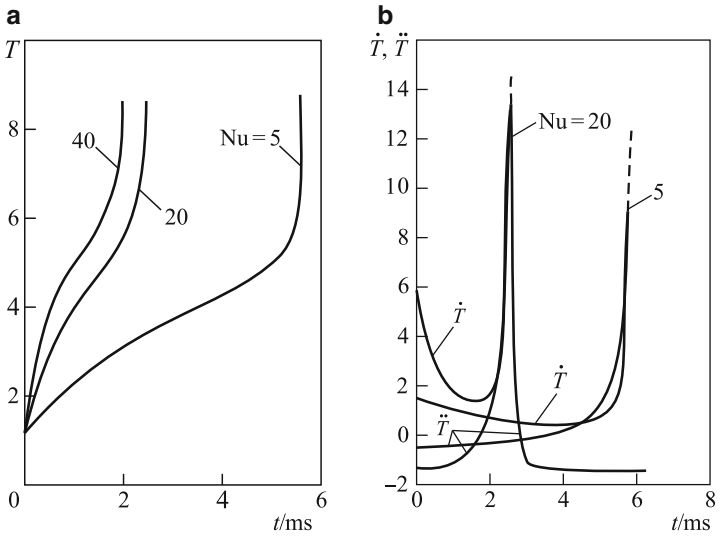

Fig. 6.6. a Typical time histories of magnesium particle temperature at $r_{s0} = 17\,\mu\text{m}$ and $\tilde{T} = 1,538\,\text{K}$. **b** Time histories of first and second temperature derivatives

Table 6.1. Dependence of t_{ign} on $\tilde{T}$ and Nu at $r_{s0} = 22\,\mu\text{m}$ for magnesium particles

$\tilde{T}$ (K)	t_{ign} (ms)		
	[63]	$Nu = 2$	$Nu = 5$
1,023	27	67	No ignition
1,083	21	46	41
1,143	17	36	24
1,203	14	30	18
1,263	13	26	14
1,323	11	23	12

A qualitative shape of the manifold M of catastrophes (ignitions) is shown in Fig. 6.5 in the section $\tilde{T} = \text{const}$ at $\tilde{T} < E/4$. The curves $T_i(\alpha)$ and $T_j(\alpha)$ on which the maxima and minima of the function $g(T; \alpha, \tilde{T})$ are reached, and typical time histories of temperature and temperature derivatives of a magnesium particle are also presented in Figs. 6.5 and 6.6. Curve DC, denoted as I, is a part of the zero isoclinic line of the governing equation, which is responsible for ignition. Curve AF, denoted as II, corresponds to the lower stationary particle state. Curve $DCAF$ is the zero isoclinic line of the first of (6.9), which is denoted as $T^0(\alpha, \tilde{T};\ E)$. Now, one can formulate the following assertion.

Assertion 1: The solution of the Cauchy problem (6.9) and (6.10) at $\alpha < \alpha_-(\tilde{T})$ is stabilized on part I of manifold M, and at $T_0 < T_j(\alpha)$ has two inflection points: $T_j(\alpha)$ and $T_i(\alpha)$. At $T_0 \in (T_j(\alpha), T_i(\alpha))$, it has one inflection point. At $T_0 > T_i(\alpha)$, there are no inflection points. At $\alpha \geq \alpha_-(\tilde{T})$, the

solution of the Cauchy problem is stabilized on part *II* of manifold M at $T_0 < T^0(\alpha, \tilde{T};\ E)$ (Table 6.1).

Note that in the first three cases, Assertion 1 categorizes the solutions of the Cauchy problem in terms of possible regimes of magnesium particle heating with ignition. The last case corresponds to normal particle heating to some stationary state with $T^0(\alpha, \tilde{T};\ E) < T_-$.

The mathematical model is completely defined when the kinetic parameters in the empirical equation for the oxide film thickness are specified. In this case, it becomes possible to solve the problem numerically and determine the particle temperature history. Here, the ignition time will be treated as an instant at which the second derivative of temperature with respect to time, $\ddot{T}$, vanishes for the second time.

6.2.2.7 Direct Problem of Particle Ignition with Vaporization

In this section, the manifold of catastrophes (ignitions) for a model of thermal explosion of a magnesium particle with metal vaporization is analyzed. The types of particle temperature evolution in the plane of model bifurcation parameters are determined and the results obtained by different models are compared.

Within the frame of the point model, the equation governing particle temperature history has the form of (6.8). To analyze qualitatively the solution of the Cauchy problem of (6.8), the zero isoclinic line of this equation in the domain of variables T, $\bar{\alpha}$, $\tilde{T}$, c, E, and L is considered using elementary catastrophe theory.

Equation (6.8) can be rewritten in the form

$$\frac{\mathrm{d}T}{\mathrm{d}\tau} = Q^+(T) - Q^-(T) = \frac{\partial G_1}{\partial T},$$

where $Q^+(T) = \mathrm{e}^{-2/T} - c\,\mathrm{e}^{-2/\gamma T}$, $Q^-(T) = \alpha(T - \tilde{T})$, $\gamma = E/L$, $\alpha = \bar{\alpha}T_\mathrm{M}$, $T_\mathrm{M} = E/(2R)$ is the reference temperature, and $G_1 = \int g_1(T)\mathrm{d}T$ is the potential function. In a similar way as was done before, consider the conditions enabling the determination of TCPs of the potential function $G_1(T)$:

$$\mathrm{e}^{-2/T} - c\,\mathrm{e}^{-2/\gamma T} = \alpha(T - \tilde{T}),$$

$$\frac{2}{T^2}\mathrm{e}^{-2/T} - \frac{2c}{\gamma T^2}\mathrm{e}^{-2/\gamma T} = \alpha,$$

$$\left(\frac{1}{T} - 1\right)\mathrm{e}^{-2/T} - \frac{c}{\gamma}\left(\frac{1}{\gamma T} - 1\right)\mathrm{e}^{-2/\gamma T} = 0.$$

The solution of this system of equations determining the TCP (T_*, α_*, c_*) location in parameter space (T, α, c) is equivalent to the solution of the equations

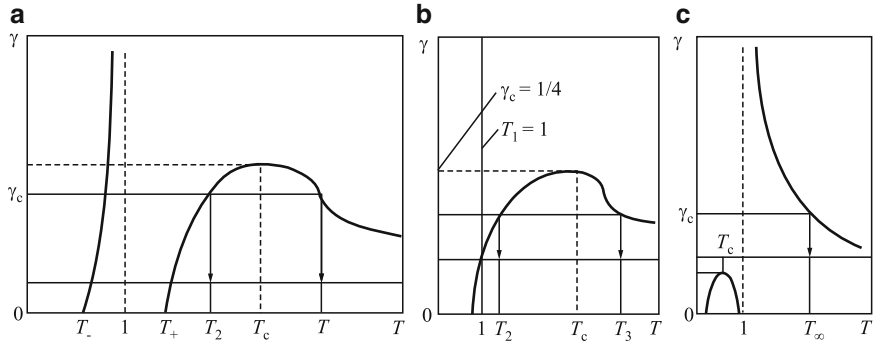

Fig. 6.7. Diagram of zeros for determining the triple-degenerate critical point (TCP) location: **a** $\tilde{T} < 0.5$, **b** $\tilde{T} = 0.5$, and **c** $\tilde{T} > 0.5$

$$\gamma T^2(T-1) = T^2 - 2T + 2\tilde{T}$$

or

$$P(T) \equiv \gamma T^3 - (\gamma+1)T^2 + 2T - 2\tilde{T} = 0. \tag{6.15}$$

It is obvious that the roots of these equations depend parametrically on γ and $\tilde{T}$. At $\tilde{T} < 0.5$, the following representation is valid:

$$\gamma = \frac{(T-T_+)(T-T_-)}{T^2(T-1)}, \tag{6.16}$$

where $T_\pm = 1 \pm \sqrt{1-2\tilde{T}}$. Let us analyze qualitatively the solutions of (6.15) using the diagram of roots $T_* = T_*(\gamma, \tilde{T})$ shown in Fig. 6.7. As a result, the following assertion can be formulated.

Assertion 2: The number and the order of the sequence of the roots of (6.15) are determined depending on γ and $\tilde{T}$ as follows:

1. $\tilde{T} < 0.5$.
   - If $0 < \gamma \le \gamma_c$, there exist three real roots $T_* = T_{1,2,3}(T_- < T_1 < 1 < T_2 < T_c < T_3)$.
   - If $\gamma > \gamma_c$, there exists one real root $T_*(T_- < T_* < 1)$ and two complex conjugate roots.
2. $\tilde{T} = 0.5$.
   - If $0 < \gamma \le \gamma_c = 0.25$, there exist three real roots $T_* = T_{1,2,3}(T_1 = 1 < T_2 < T_c < T_3)$ and $T_2 = T_3$ for $\gamma = \gamma_c$.
   - If $\gamma > \gamma_c$, there exists one real root $T_{*1} = 1$ and two complex conjugate roots.
3. $\tilde{T} > 0.5$. There exists one real root $T_1 > 1$ for all $\gamma > 0$.

The critical parameter here is $\gamma_c = \max\ \gamma(T)|_{T>1} = \gamma_c(\tilde{T})$ at $\tilde{T} \le 0.5$. The function $\gamma_c(\tilde{T})$ is determined parametrically: $\gamma_c = \gamma(T_c)$ as $\tilde{T} = H(T_c)$

owing to the equality $\left.\frac{\mathrm{d}\gamma(T)}{\mathrm{d}T}\right|_{T=T_\mathrm{c}} = 0$. It can be readily shown that at realistic $\tilde{T}$ values (which do not exceed 0.2–0.3), the function $\gamma_\mathrm{c}(\tilde{T})$ is always less than unity. The proof of Assertion 2 follows from the elementary construction of the function $\gamma(T)$ determined by (6.16) and from its continuity at $T > 1$.

For $\tilde{T} \le 0.5$, (6.15) has the following approximate solutions:

$$\text{at } \gamma \ll 1,\ T_{1,2} = T_\mp + \gamma\frac{T_\mp^2}{2} + \gamma^2\frac{T_\mp^3}{2}\left(1 - \frac{3}{2}T_\mp\right) + O(\gamma^3),$$

$$T_3 = \frac{\gamma+1}{\gamma} - (T_{*1} + T_{*2}) + O(\gamma^3) \text{ at } \gamma \gg 1,$$

$$T_* = 1 + \gamma^{-1}(2\tilde{T} - 1) - 2\gamma^{-2}(2\tilde{T} - 1)^2 + O(\gamma^{-3}).$$

In a general case, when γ is finite, the solution of (6.15) can be found numerically. The results are presented in Fig. 6.8 in the form of a diagram of roots $T_* = T_*(\tilde{T}, \gamma)$ for several values of γ.

Note that in cases of practical importance with $\gamma_\mathrm{c} < 1 < \gamma$, the CM possesses a unique TCP similar to the CM in the ignition model, which does not take evaporation into account. The existence of a CM with three TCPs is a new feature in the case when the activation energy of metal evaporation is much larger than that of the oxidation process, i.e., $L \gg E$. This implies the possibility of nontrivial scenarios of particle ignition for a given relation between the governing parameters of the system.

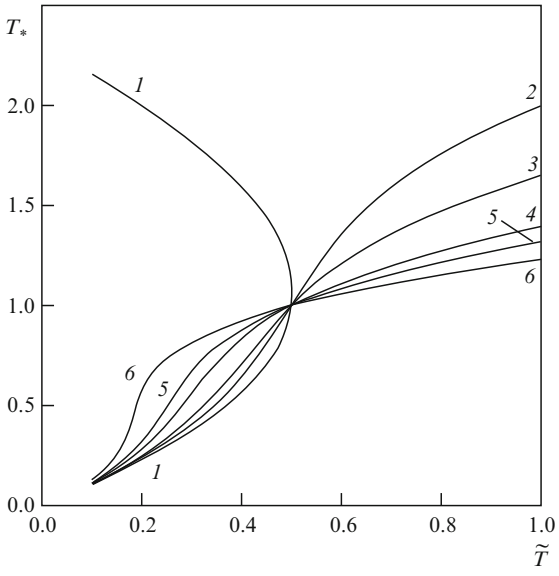

Fig. 6.8. The diagram of roots $T_* = T_*(\tilde{T}, \gamma)$ for determining the TCP location: $\gamma = 0.1$ (*1*), 0.5 (*2*), 0.8 (*3*), 1.5 (*4*), 2.0 (*5*), and 3.0 (*6*) (in the case $\gamma = 0.1$ the branch of the third, largest root is not shown)

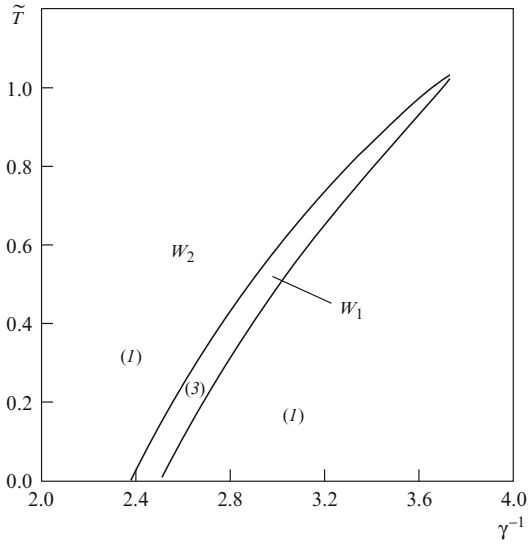

Fig. 6.9. Partition of the parameter plane $(\gamma^{-1},\ \tilde{T})$ into the regions with three (W_1) and one (W_2) TCPs; the *numbers* in *parentheses* show the number of TCPs

Figure 6.9 presents the bifurcation diagram for the roots of (6.15) in the $(\gamma^{-1}, \tilde{T})$-plane. The diagram separates the regions of parameters with different numbers of TCPs and is obtained using curves $\tilde{T} = \tilde{T}_{1,2}(\gamma)$ along which the discriminator of the given cubic equation vanishes. Region W_1 is a set with three TCPs, and region W_2 is a set with one TCP. As a matter of fact, Fig. 6.9 is the Semenov diagram with the curves of total heat supply $Q^+(T)$ and heat removal $Q^-(T)$. The equation $Q^+(T) = 0$ possesses the following roots:

$$T = 0 \text{ and } T = T^0 = \frac{2(\gamma - 1)}{\gamma \ln c^{-1}},$$

where T^0 has the meaning of stationary adiabatic temperature in the system (the temperature up to which the particle is heated in a thermally insulated volume with temperature $\tilde{T}$). It is obvious that depending on the sign of T^0 and the relation between $\tilde{T}$ and T^0, different sorts of tangency of curves $Q^+(T)$ and $Q^-(T)$ can exist (we restrict ourselves to the condition $c < 1$). The analysis of the results can be summarized in the following assertion.

Assertion 3:

1. $T^0 > 0$. Then,
   - If $\tilde{T} < T^0$, there exists one point of tangency (T_K, α_K), and
     - At $\alpha < \alpha_K$, there exist three equilibrium positions: $(0, \tilde{T})$, (T^0, T_K), and (T_K, ∞).
     - At $\alpha > \alpha_K$, there exists one equilibrium position: $(0, \tilde{T})$.

- If $\tilde{T} > T^0$, there exist three points of tangency (T_{K_i}, α_{K_i}), $i = 1, 2, 3$ numbered in the order of increasing α_K, and
  - At $\alpha < \alpha_{K_1}$, there exist three equilibrium positions: $(0, T_{K_1})$, (T_{K_1}, T^0), and (T_{K_3}, ∞).
  - At $\alpha_{K_1} < \alpha < \alpha_{K_2}$, there exists one equilibrium position lying at (T_{K_3}, ∞).
  - At $\alpha_{K_2} < \alpha < \alpha_{K_3}$, there exist three equilibrium positions: $(\tilde{T}, T_{K_2})$, (T_{K_2}, T_{K_3}), and (T_{K_3}, ∞).
  - At $\alpha > \alpha_{K_3}$, there exists one equilibrium position: $(\tilde{T}, T_{K_2})$.

2. $T^0 < 0$. There exist two points of tangency (T_{K_i}, α_{K_i}), $i = 1, 2$ and
   - At $\alpha < \alpha_{K_1}$, there exists a single equilibrium position: (T_{K_2}, ∞).
   - At $\alpha_{K_1} < \alpha < \alpha_{K_2}$, there exist three equilibrium positions: $(\tilde{T}, T_{K_1})$, (T_{K_1}, T_{K_2}), and (T_{K_2}, ∞).
   - At $\alpha > \alpha_{K_2}$, there exists a single equilibrium position: $(\tilde{T}, T_{K_1})$.

The proof of Assertion 3 can be readily seen from curves $Q^{\pm}(T)$ in Fig. 6.10.

Some important properties of the source function $Q^+(T)$ are listed below:

1. $Q^+(T) \to 0$ as $T \to 0$.
2. $Q^+(T) \to (1 - c)$ as $T \to \infty$.
3. If $0 < c < 1$, $\gamma > 1$ or $c > 1$, $\gamma < 1$, then $T^0 > 0$; if $0 < c < 1$, $\gamma < 1$ or $c > 1$, $\gamma > 1$, then $T^0 < 0$.

Turn now to the analysis of particle temperature evolution. For this purpose, consider the typical sections $c = \text{const}$ of the CM specified by the equation $Q^+(T) - Q^-(T) = 0$. Upon determining the TCP coordinates, one can construct the images of the fold curves in the (α, c)-plane. They are the projections of the corresponding DCPs onto the equilibrium surfaces (CMs) in the

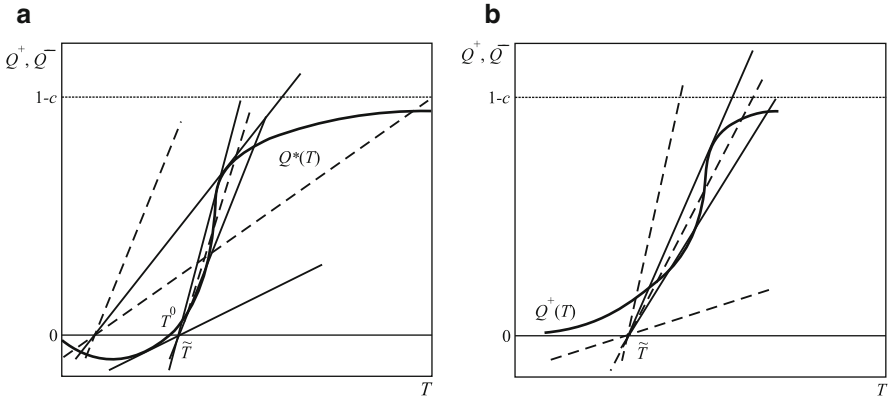

Fig. 6.10. Shapes of Semenov diagrams depending on the stationary adiabatic temperature T^0 (at $c < 1$): **a** $T^0 > 0$, **b** $T^0 < 0$; *dashed curves* show different locations of the heat removal curve $Q^-(T)$, *solid curves* show the limiting (tangent) locations of this curve

(T, α, c)-space. Using the properties of the function $Q^+(T)$ and the estimates for $T_\pm$, one can construct a qualitative shape of the CM in sections $c = \text{const}$ as shown in Fig. 6.11, where typical regions in the phase plane (T, α) are determined. One can observe, for example, the following variants of temperature histories:

- At $(\alpha, T_0) \in D_1'$, a regime with explosion-free particle heating which tends to equilibrium along the lower branch $T_{\rm I}'(\alpha) < \tilde{T}$
- At $(\alpha, T_0) \in D_2'$, an ignition regime with temperature passage to the upper stable branch $T_{\rm III}'(\alpha)$ of stationary states
- At $(\alpha, T_0) \in D_3'$, a regime of extinction with temperature stabilization on the branch $T_{\rm I}'(\alpha)$

The remaining variants can be analyzed in a similar way.

6.2.2.8 Inverse Problem of Particle Ignition

The analysis of the manifold of catastrophes (ignitions) conducted makes it possible to categorize kinetic laws of metal particle oxidation in air with regard to metal vaporization. The equations governing the preignition state of a magnesium particle can be written in the form

$$k\mathrm{e}^{-E'/T} - v\mathrm{e}^{-L'/T} = \alpha_0(T - \tilde{T}),\ k\frac{E'}{T^2}\mathrm{e}^{-E'/T} - v\frac{L'}{T^2}\mathrm{e}^{-L'/T} = \alpha_0, \quad (6.17)$$

where $\alpha_0 = \lambda Nu/c(2r_{\rm s}\rho_{\rm s}q)$, E' and L' are the activation energy and evaporation heat normalized by $RT_{\rm M}$, and $T_{\rm M} = 300\,\mathrm{K}$ is the reference temperature. Following the data of [27], $L' = 53.333$. Then (6.17) can be written for two arbitrary points $(r_{{\rm s}j}, T_j)$, $j = 1, 2$ at the experimental curve describing the dependence of the limiting ignition temperature in air on the particle radius [60]. This allows one to come to a closed system of transcendental equations for determining the unknown quantities E' and k (if they exist) as well as particle temperatures at the ignition limit. In so doing, the following values of the kinetic parameters were derived for $v = 0.15\,\mathrm{m\,s^{-1}}$: $E' = 40.315$ $(E/R = 12,094\,\mathrm{K})$, $k = 0.169\,\mathrm{m\,s^{-1}}$ for fine particles (with the radius ranging from 15 to $60\,\mu\mathrm{m}$), $E' = 96.452$ $(E/R = 28,936\mathrm{K})$, and $k = 6.855 \times 10^5\,\mathrm{m\,s^{-1}}$ for large particles (with the radius ranging from 300 to $600\,\mu\mathrm{m}$).

It is interesting to compare the ignition delay times obtained on the basis of these kinetic parameters with those obtained with the model without metal vaporization taken into account. As is seen from Table 6.2, the differences are insignificant for fine particles. For large particles, the difference does not exceed 11%.

6.2.2.9 Specific Features of Aluminum Particle Ignition

Ignition of aluminum particles differs qualitatively from that of magnesium particles. At normal atmospheric conditions, aluminum particles are known

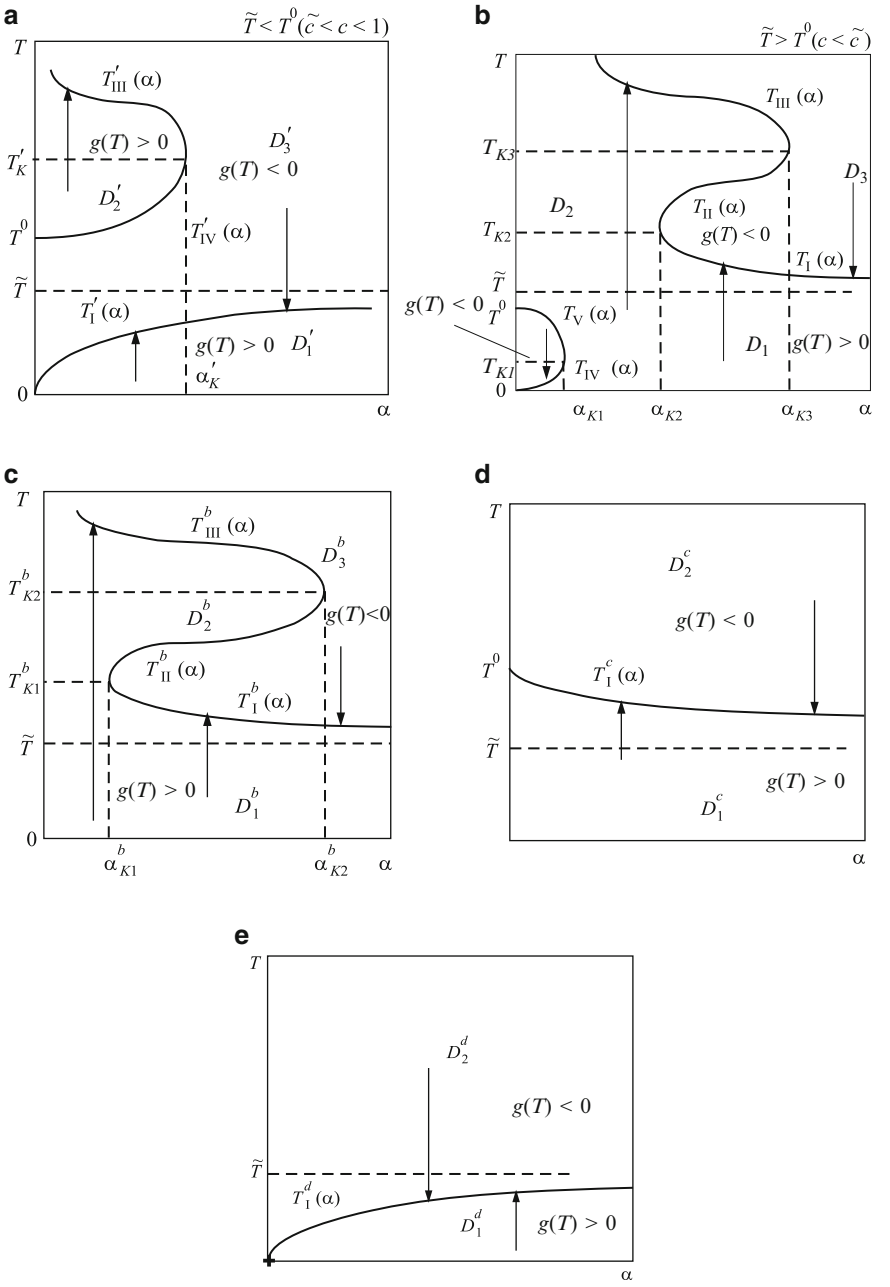

Fig. 6.11. Structure of the ignitions manifold (typical sections $c = \text{const}$): **a**, **b** $0 < c < 1$, $\gamma > 1$; **c** $0 < c < 1$, $\gamma < 1$; **d** $c > 1$, $\gamma < 1$; **e** $c > 1$, $\gamma > 1$; *arrows* indicate possible variants of particle heating/cooling

Table 6.2. Comparison of ignition delay times of a magnesium particle (ms) at $\tilde{T} = 1,538\,\mathrm{K}$ predicted by two models

Particle radius (μm)	15	22	30	60	300	400	500	600
Model (1.2.2)	22.0	39.6	64.0	200.0	2,200	3,800	6,000	8,500
Model (1.2.3)	22.0	39.2	64.1	202.3	1,990	3,460	5,320	7,560

to be covered by an oxide film possessing protective properties which complicate oxygen diffusion to the pure metal. Therefore, the rate of high-temperature oxidation of aluminum particles depends significantly on the oxide film thickness.

Various oxidation laws of aluminum particles have been observed experimentally. In [94, 95], the growth of the oxide film was described by the exponential law

$$\frac{\mathrm{d}h}{\mathrm{d}t} = KC_{\mathrm{ox}}^{n_{\mathrm{ox}}} \exp\left(-\frac{E}{RT}\right) \exp\left(-\frac{h}{h_0}\right),$$

where C_{ox} is the oxidizer concentration near the particle surface and n_{ox} is the reaction order in relation to the oxidizer. Another frequently used equation of oxidation kinetics has the form

$$\frac{\mathrm{d}h}{\mathrm{d}t} = \frac{KC_{\mathrm{ox}}^{n_{\mathrm{ox}}}}{h^n} \exp\left(-\frac{E}{RT}\right).$$

The power exponent n in the last equation determines the dependence of the aluminum oxidation rate on the oxide film thickness. The case with $n = 0$ was considered in Sect. 6.2.2.7 for magnesium particles.

In [96, 97], the oxidation rate of aluminum was assumed to be determined by the kinetics of the heterogeneous reaction and to be independent of the oxide film thickness. It was implied that the heterogeneous reaction occurred only on the portion of the particle surface not covered by oxide crystals. It was assumed in [97] that $n = 1$. This assumption resulted in a parabolic oxidation law, which is valid when the oxidation rate is limited by oxygen diffusion through the oxide film. Thus, the particle ignition model in [97] was based on the heat balance equation supplemented by the equation for the fraction of the particle surface free from the crystalline oxide. The parabolic equation of the oxide-film growth at the aluminum particle surface was also considered in [72], where heat sinks due to particle vaporization and melting as well as radiation heat losses were taken into account in the heat balance equation. Analysis of numerical calculations allowed Medvedev et al. [72] to put forward a particular mechanism of aluminum particle ignition and determine the effect of various initial parameters on the ignition delay.

In the papers mentioned above, various approaches were used to determine the kinetic constants of the empirical ignition law. Among them are the methods of elementary catastrophe theory, the fitting of model predictions with the experimental dependencies of the ignition delay on the shock wave

Mach number [72], and some heuristic conditions relevant to the oxide film melting point [98]. In most papers, the model predictions were compared with the measured ignition delays in terms of a single parameter, namely, the ambient gas temperature. However, it is well known from experiments [99–102] that the ignition delay is affected not only by the ambient gas temperature but also by the particle size and oxidizer concentration in the ambient gas. It is therefore important to have a model capable of predicting aluminum particle ignition delay as a function of different governing parameters of the problem.

6.2.2.10 Point Model of Aluminum Particle Ignition

Consider a spherical aluminum particle of diameter d_s which is suddenly placed in a quiescent gas with temperature $\tilde{T}$ behind a reflected shock wave [103]. Thermal interaction of the particle with hot gas results in a heterogeneous reaction of low-temperature oxidation in a thin (as compared with the particle radius) layer on the particle surface. As a consequence, the mean particle temperature T increases and the particle can be ignited. The heat balance equation for the aluminum particle is expressed in the form

$$mc_{\mathrm{s}}\frac{\mathrm{d}T}{\mathrm{d}t} = -Sk_{\mathrm{h}}(T-\tilde{T}) + Sq\rho_{\mathrm{ox}}\frac{\mathrm{d}h}{\mathrm{d}t}.$$

For the aluminum oxidation kinetics, the following parabolic law is used:

$$\frac{\mathrm{d}h}{\mathrm{d}t} = \frac{KC_{\mathrm{ox}}}{h}\exp\left(-\frac{E}{RT}\right).$$

The initial conditions for these equations are

$$t=0: \quad T=T_0,\ h=h_0,$$

where ρ_{ox} is the aluminum oxide (Al_2O_3) density. Thus, the problem of aluminum particle ignition in a quiescent oxidizing gas is reduced to determining the functions $T(t)$ and $h(t)$ in the region $[0, t_{\mathrm{ign}}]$, where they satisfy the above equations and initial conditions.

There is still a need to determine the unknown parameters K and E. In the literature, different values of these parameters are reported. For example, $E = 17\,\mathrm{kcal\,mol^{-1}}$, $K = 1.9\times10^{-9}\,\mathrm{m^2\,s^{-1}}$, and $n=1$ are reported in [101], while $E = 20\,\mathrm{kcal\,mol^{-1}}$, $K = 18\times10^{3}\,\mathrm{m^2\,s^{-1}}$, and $n=0$ are reported in [96]. In general, one cannot expect the values of K and E to be constant over the wide range of governing parameters as the model under consideration oversimplifies the problem. Therefore, to use this simple model to explain the experimental dependencies of the ignition delay t_{ign} and the minimal temperature of the gas required for particle ignition $\tilde{T}_{\mathrm{lim}}$ on the particle size, it is worth considering K as a function of the ambient temperature and particle radius.

The approach suggested herein is as follows. One can determine the value of the preexponential factor K for any two experimental points $(t_{\mathrm{ign1}}, \tilde{T}_1)$ and $(t_{\mathrm{ign2}}, \tilde{T}_2)$ reported, e.g., in [101]. Then $K(\tilde{T})$ can be approximated by

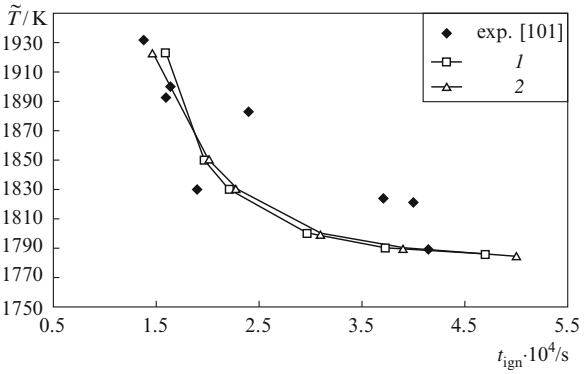

Fig. 6.12. Measured [101] and predicted [103] dependencies of the aluminum particle ($d_s = 6\,\mu$m) ignition delay on the ambient gas (oxygen) temperature. Curves *1* and *2* refer to $K = (a\tilde{T} + b)$ and $K = (a\tilde{T} + b)[\tilde{T} - \tilde{T}_{\lim}(d_s, C_{ox})]$, respectively. *Solid symbols* correspond to experiments [101]

$$K(\tilde{T}) = \begin{cases} f(\tilde{T}), & \tilde{T} > \tilde{T}_* \\ 0, & \tilde{T} \le \tilde{T}_* \end{cases},$$

where $f(\tilde{T})$ is a linear function, and $\tilde{T}_*$ is some reference temperature. Physically, the reference temperature $\tilde{T}_*$ is the minimum temperature at which particle ignition is still possible. According to the above relationship, at $\tilde{T} < \tilde{T}_*$ the particle temperature rises solely owing to heat transfer from the ambient gas and tends to $\tilde{T}_*$ in the limit.

The results of calculations for aluminum particle ($d_s = 6\mu$m) ignition in oxygen are shown in Fig. 6.12 as curve 1 in the plot $\tilde{T}(t_{ign})$. The predictions are compared with the experimental data [101] (solid symbols in Fig. 6.12). A satisfactory agreement of predicted and measured results for intermediate oxygen temperatures exists.

According to experiments [99,100,102], the minimal gas temperature $\tilde{T}_{\lim}$ is also not constant and depends on the particle diameter d_s, oxygen concentration in the ambient gas C_{ox}, and ambient gas temperature $\tilde{T}$. Thus, one can represent the reference temperature $\tilde{T}_*$ as $\tilde{T}_* = \tilde{T}_{\lim}(d_s, C_{ox})$. This dependence can be obtained, e.g., by approximating the experimental data of [102].

Let us study the influence of the particle diameter on the preexponential factor K, using the experimental dependencies of the ignition delay on the particle diameter [99,100]. Note that the results reported in [99,100] are close to each other. As a result of parametric calculations and comparison with the experiments, a certain value of K can be derived, e.g., for $\tilde{T} = 2,510$ K. Now, the preexponential factor can be finally represented as

$$K = (a\tilde{T} + b)[\tilde{T} - T_{\lim}(d_s, C_{ox})].$$

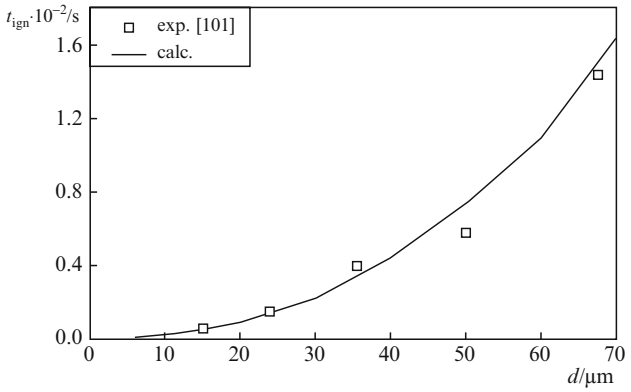

Fig. 6.13. Measured [101] and predicted [103] dependencies of the ignition delay on the aluminum particle diameter

At $\tilde{T} = 2,510\,\mathrm{K}$, the value of K predicted by this empirical formula is the same as that obtained using the experimental data of [100]. The activation energy E entering the governing equations of the model is taken to be $17\,\mathrm{kcal\,mol^{-1}}$ in accordance with [104].

To solve the governing equations, an implicit multistep method [105] was applied. The following values of physical variables were used in the calculations. For aluminum, $\rho = 2,689\ \mathrm{kg\,m^{-3}}$, $c_\mathrm{s} = 1,010\ \mathrm{J\,(kg\,K^{-1})}$, and $\rho_\mathrm{ox} = 3,970\ \mathrm{kg\,m^{-3}}$. For oxygen, $\lambda = 2.4 \times 10^{-2}(\tilde{T}/\tilde{T}_0)^{0.75}\ \mathrm{J\,(m\,s\,K)^{-1}}$, $Nu = 2$, and $q = 35.6 \times 10^6\ \mathrm{J\,kg^{-1}}$.

The results of the calculations are shown in Figs. 6.12 and 6.13. Curves 1 and 2 in Fig. 6.12 are slightly different but still lie within the scatter of experimental data. In general, both figures indicate that the modified ignition model of aluminum particles provides satisfactory agreement with the experimental data on ignition delay as a function of particle size and ignition delay as a function of ambient gas temperature.

6.2.3 Dynamic Conditions

6.2.3.1 Ignition of Metal Particles Behind Reflected Shock Waves

The problem of ignition of fine metal particles in static and dynamic conditions behind planar incident and reflected shock waves was considered theoretically and experimentally in [60, 72, 74–77], and behind detonation and explosion waves in [106, 107]. It was shown in [72, 74] that the consideration of particle motion and low-temperature metal oxidation allows one to reproduce available experimental data on the dependence of the ignition delay time t_ign on the shock wave Mach number M_0. To explain the experimental data on ignition of magnesium particles behind reflected shock waves in a shock tube, a hypothesis on cracking of the oxide layer prior to its melting was put forward

in [108, 109]. Below we provide another explanation for the effects observed in [108,109] within the framework of a model similar to that in [72,74], which takes into account particle dynamics.

Consider a gas–particle suspension of magnesium particles filling the half-space bounded by a rigid wall. After a planar shock wave passes through it, the particles start moving and heating up in the shock-induced flow. After the shock wave is reflected from the rigid wall, the gas temperature increases again, while the gas velocity vanishes, i.e., $u_{\rm g} = 0$. Thus, particles near the wall are subjected to variable dynamic and thermodynamic parameters of the ambient gas. Let the volume fraction of particles be sufficiently small. Then the ignition process can be described by a model similar to that in [72, 74]:

$$mc_{\rm s}\frac{{\rm d}T}{{\rm d}t} = 2\pi r_{\rm s}\lambda Nu(\tilde{T} - T) + Sq\rho_{\rm ox}\left[k_0 C_{\rm ox}\exp(-E/RT) - v\exp(-L'/RT)\right], \tag{6.18}$$

$$m\frac{{\rm d}u}{{\rm d}t} = \frac{1}{2}AC_{\rm D}\rho U\left|U\right|,$$

where u is the particle velocity, $A = \pi r_{\rm s}^2$ is the particle cross-sectional area, $U = u_{\rm g} - u$ is the relative gas–particle velocity, and $C_{\rm D}$ is the particle drag coefficient [74, 110].

The system of (6.18) is supplemented with the initial data

$$t = 0: \quad u = 0, \quad T = T_0, \tag{6.19}$$

which reflect the fact that the velocity and temperature of the particles remain unchanged across the incident shock wave.

The main specific feature of the problem expressed in (6.18) and (6.19) is the presence of multiple stationary states at the variation of a characteristic bifurcation parameter. Let us illustrate this implication of (6.18) and (6.19) for the case when particle vaporization can be neglected and the particle velocity is constant. In this case, there exists a bifurcation parameter $\alpha = c_{\rm s}\tau_3/(q\tau_2)$, where $\tau_3 = r_{\rm s}/(3k_0c_{\rm ox})$ and $\tau_2 = 2c_{\rm s}\rho_{\rm s}r_{\rm s}^2/(3\lambda Nu)$. The turning points of the zero curve at the (T, α)-plane were found for the following constants: $T_- = 1,158\,{\rm K}$, $T_+ = 26,960\,{\rm K}$, $\alpha_- = 5.946\times10^{-13}$, and $\alpha_+ = 1.363\times10^{-5}$. It turned out that at $\alpha > \alpha_-$, e.g., $\alpha = (1+0.01)\alpha_-$, there is no ignition and the particle temperature tends to its final equilibrium state. At $\alpha < \alpha_-$, e.g., $\alpha = (1-0.01)\alpha_-$, particle ignition occurs followed by rapid temperature growth. A comparison with data in [77] for the case of zero particle velocity shows the proximity of predicted and experimental data in terms of the dependence of the ignition delay time on the particle radius.

The results of experimental studies on ignition of gas–particle mixtures of magnesium powders in pure oxygen behind a reflected shock wave were presented in [108] (particles in a shock tube were located initially at a distance of 1 cm from the end wall). For particles with diameter $d_{\rm s0} = 2r_{\rm s0} = 90\,\mu{\rm m}$, the values of $t_{\rm ign}$ are presented for different initial pressures p_0 and shock wave Mach numbers M_0. In variant I, $t_{\rm ign} = 1.4 \pm 0.1$ ms at $M_0 = 4.2$ and

Table 6.3. Results of experiments and computations for a monodisperse mixture

Variant	M_0	p_0 (bar)	$\tilde{T}$ (K)	$\tilde{T}_1$ (K)	D ($\mathrm{m\,s^{-1}}$)	D_1 ($\mathrm{m\,s^{-1}}$)	u_g ($\mathrm{m\,s^{-1}}$)	t_{ign} (ms)	
								Experiment	Computation
I	4.2	0.2	1,265	2,470	1,351	484.5	1,071	1.4 ± 0.1	0.65 (1.3)
II	3.9	0.3	1,129	2,162	1,255	457.6	984.6	2 ± 0.2	1 (2.1)
III	3.4	0.3	924.8	1,698	1,094	414.4	839.3	–	—

There is no ignition in variant III. The values in *parentheses* are t_{ign} values at refined parameters behind the shock wave

Table 6.4. Results of experiments and computations for the polydisperse mixture

Run	d_{s0} (μm)	Experiment		Computation run 1		Computation run 2	
		$\tilde{T}_1$ (K)	t_{ign} (ms)	t_{ign} (ms)	d_{s0} (μm)	t_{ign} (ms)	d_{s0} (μm)
1				0.04	20	0.014	4
	1–40	2,173	0.06	0.12	40	0.070	20
						0.210	40
2		1,470	0.11	0.065	20	0.030	4
				0.19	40	0.150	20
						0.480	40
3				0.23	70	0.300	60
		2,325	0.26	0.44	100	0.600	80
	63–100					0.800	100
4				0.47	70	0.900	60
		1,515	0.6	0.90	100	1.500	80
						2.100	100

$p_0 = 0.2\,\mathrm{bar}$; in variant II, $t_{ign} = 2.0 \pm 0.2$ ms at $\mathrm{M}_0 = 3.9$ and $p_0 = 0.3\,\mathrm{bar}$; in variant III, the particle did not ignite at $M_0 = 3.4$ and $p_0 = 0.3\,\mathrm{bar}$.

Table 6.3 presents the values of the gas temperature behind the incident shock wave, $\tilde{T}$, and the reflected shock wave, $\tilde{T}_1$, velocities D and D_1 of the waves, and the gas velocity behind the incident shock wave for the above values of M_0 and p_0. The numerical results were obtained using two models (see below) and are presented for each of variants I–III. Without consideration of particle velocity variation, no ignition was observed in the calculations in all three variants and the particle temperature attained its stationary value. The model accounting for particle motion yields the following results: $t_{ign} = 0.65$ and 1.0 ms in variants I and II, respectively, while in variant III there was no ignition.

In [108], the experimental data on ignition delay times for polydisperse magnesium powders were also presented. We have performed numerical calculations of the ignition delay time for each of the variants for some selected values of the particle diameter. The results are presented in Table 6.4 (run 1). The chosen values of a characteristic particle diameter in a polydisperse

gas–particle mixture can be seen to yield the upper and lower limits for t_{ign}. The following values of thermophysical parameters were used: $\mu = 2\times10^5\ \text{kg}\,(\text{m}\,\text{s})^{-1}$ and $c_{\text{s}} = 1.2\times10^3\ \text{J}\,(\text{kg}\,\text{K})^{-1}$ (run 1). However, in view of elevated temperatures and pressures behind the incident and the reflected shock wave, there is a need to correct these values. The computations of the ignition delay time with corrected thermophysical data are presented in Table 6.4 (run 2) and in Table 6.3 (numbers in parentheses). The thermophysical data for high-pressure and high-temperature conditions used for the computations reported in Tables 6.3 and 6.4 were taken from [111]. It turns out that taking the dependence of the thermophysical parameters on pressure and temperature into account leads to a better agreement between measured and calculated data.

Thus, the above analyses indicate that the results of the physical experiments reported in [108] on ignition of magnesium particles behind a reflected shock wave in the vicinity of the shock-tube end wall are described satisfactorily by the model accounting for particle motion, low-temperature metal oxidation, and the dependence of the thermophysical properties of the system on temperature and pressure.

The effect of a dense particle cloud on the particle ignition behavior was studied theoretically by Fedorov [112] using the example of a magnesium particle cloud in air. The model included a heterogeneous chemical reaction on the particle surface and was validated against the experimental data on the minimal air temperature required for particle ignition as a function of particle radius. The predicted results are compared with the experimental data in Fig. 6.14.

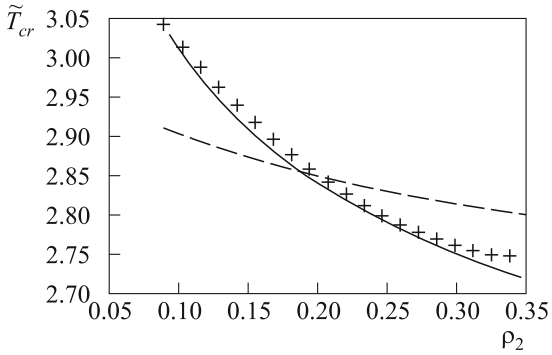

Fig. 6.14. The minimal air temperature $\tilde{T}_{\text{lim}}$ required for ignition of a magnesium particle cloud as a function of cloud density. The particle radius is 5 μm; *crosses* denote experimental data of Matsko et al. [170]; the *dashed curve* corresponds to the calculation with the reaction rate constants derived for oxidation of a single magnesium particle in air; the *solid curve* corresponds to the calculations of magnesium particle cloud ignition by Fedorov [112]

6.2.3.2 Ignition of Metal Particles Behind Incident Shock Waves

Consider now the approaches to mathematical modeling of metal particle ignition in a high-temperature flow behind an incident shock wave. A review of early theoretical and experimental results on particle ignition in steady-state and dynamic conditions is presented elsewhere [87]. Subsequent bibliographic references are presented in [36,54,112–119]. They provide the entire hierarchy of mathematical models of ignition waves in reacting particle suspensions in one- and two-velocity approximations. In the following discussion, two-phase flows with very small concentrations of solid particles are considered. Descriptions of ignition phenomena at finite particle concentrations, when it is necessary to invoke the theory of interpenetrating continua, can be found in the papers cited above.

In the region behind the propagating shock wave, particles accelerate up to the flow velocity and heat up owing to heat exchange with the postshock gas and the oxidation reaction. At a very small particle volume fraction, one can neglect the interaction between particles and the influence of particles on the gas flow. It is implied that the chemical reaction of high-temperature metal oxidation may be activated in the suspension by an incident shock wave. The approximation of "isolated spherical particles" [110] is true and therefore can be adopted. The ignition kinetics (the kinetics of high-temperature oxidation) is assumed to follow the Arrhenius law depending on the oxide film thickness, with the particle radius variation neglected.

The equations governing the flow of such a mixture can be written as

$$\begin{gathered} mc_{\mathrm{s}}\frac{\mathrm{d}T}{\mathrm{d}t} = Q_{\mathrm{chem}} - Q_{\mathrm{conv}} - Q_{\mathrm{phase}} - Q_{\mathrm{rad}} - Q_{int}, \\ m\frac{\mathrm{d}u}{\mathrm{d}t} = -F_{\mathrm{S}} - F_{\mathrm{m}} - F_{\mathrm{B}}. \end{gathered} \tag{6.20}$$

The source terms in the first expression in (6.20) correspond to the heat fluxes due to:

1. Heterogeneous chemical reaction:

$$Q_{\mathrm{chem}} = Sq\rho_{\mathrm{ox}}\frac{\mathrm{d}h}{\mathrm{d}t}.$$

2. Convective heat transfer between particles and gas:

$$Q_{\mathrm{conv}} = S\lambda\, Nu(T - \tilde{T}).$$

3. Particle vaporization:

$$Q_{\mathrm{phase}} = \frac{\lambda}{\rho c_p}\frac{S}{Le}\left(\frac{p_*}{p}\right)\exp\left(-\frac{L}{RT}\right).$$

4. Radiation heat loss:

$$Q_{\mathrm{rad}} = S\varepsilon\sigma(T^4 - \tilde{T}^4).$$

5. Particle heating and melting:

$$Q_{\text{int}} = 4\pi r_{\text{s}}\lambda_{\text{s}}(T - T_0)\exp\left(-\frac{t}{t_{\text{h}}}\right).$$

The source terms in the second expression in (6.20) correspond to the forces acting on the particle:

1. Stokes force:

$$F_{\text{s}} = AC_{\text{D}}\rho\frac{(u - u_{\text{g}})\,|u - u_{\text{g}}|}{2}.$$

2. Force of virtual masses:

$$F_{\text{m}} = -\frac{2}{3}\pi r_{\text{s}}^3\rho\frac{\text{d}u}{\text{d}t}.$$

3. Basset force:

$$F_{\text{B}} = -6r_{\text{s}}^2\sqrt{\pi\rho\mu}\int\limits_0^t (t - \tau)^{-0.5}\frac{\text{d}u}{\text{d}\tau}\text{d}\tau.$$

Le is the Lewis number, c_p is the constant-pressure specific heat of the gas, p_* is the reference pressure, ε is the particle blackness rate, σ is the Stefan–Boltzmann constant, $t_{\text{h}} = r_{\text{s}}^2/3a_{\text{s}}$ is the characteristic time of particle heating, and a_{s} is the thermal diffusivity of the solid.

The following ignition kinetics is specified:

$$\frac{\text{d}h}{\text{d}t} = K_n C_{\text{ox}}^n h^{-n}\exp\left(-\frac{E}{RT}\right), \tag{6.21}$$

where K_n is the preexponential factor and n is the reaction order with respect to the oxidizer: $n = 1$ for aluminum and $n = 0$ for magnesium. The system of (6.20) and (6.21) with supplementary relationships is closed with respect to the functions that are sought.

The parameters characterizing the gas flow can be readily found from standard relationships for the flow behind a shock wave propagating at velocity D. Equations (6.20) and (6.21) written in the frame of reference moving with the shock wave at velocity D must satisfy the following Cauchy conditions:

$$t = t_0: \quad u = D, \quad T = T_0, \quad h = h_0. \tag{6.22}$$

Upon determining the functions $u(x,t)$, $T(x,t)$, and $h(x,t)$, where x is the coordinate, one can find the mean density of the dispersed phase, $\rho_{\text{s}}(x,t)$, from the equation of dispersed-phase mass conservation. Thus, the problem of particle ignition in the shock-induced gas flow can be formulated as follows:

Find functions $u(x,t)$, $T(x,t)$, and $h(x,t) \quad \in C^1(0, t_{\text{ign}})$ *satisfying (6.20) and (6.21) in the region* $[0, t_{\text{ign}})$ *and the Cauchy data (6.22).*

The problem formulated above was solved numerically by Gear's method. The calculations were performed for ignition of magnesium and aluminum particles in a shock wave propagating in gaseous oxygen. In the calculations,

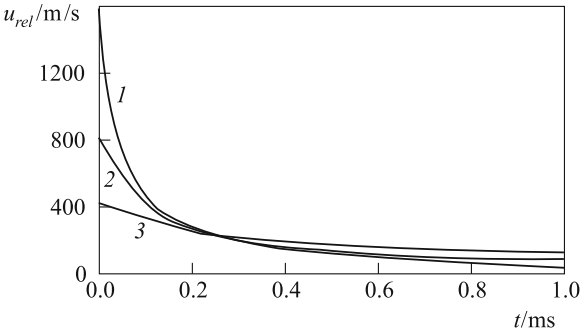

Fig. 6.15. The temporal dependence of the particle slip velocity

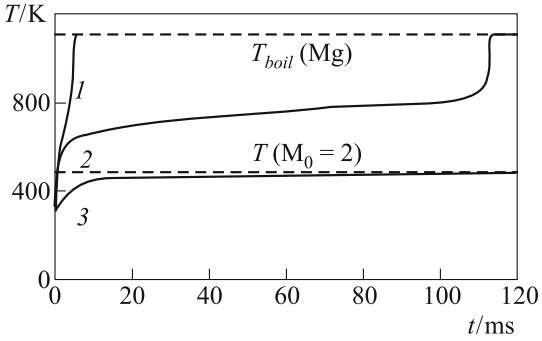

Fig. 6.16. Predicted temperature curves for magnesium particles

the particle size was varied from 1 to 100 μm, the initial pressure was varied from 0.01 to 1 bar, and the shock wave Mach number was varied from 1.1 to 6.0.

The predicted results are shown in Fig. 6.15 as the dependence of the relative particle–gas velocity, $U = u - u_{\rm g}$, in the postshock flow versus time. Both experiment and calculation were suited for $p_0 = 0.135$ bar and $M_0 = 5.0$. In the experiments, ignition of a cloud of particles with a mean diameter of 17 μm was studied. The calculations show that an increase in the shock wave Mach number leads to a reduction of the velocity relaxation zone length. This can be attributed to an increase in the gas density, and hence the drag force. Note that similar calculations without consideration of the Basset force result in a shorter relaxation zone duration by a factor of about 3. Note also that the effect of the force of virtual masses, $F_{\rm m}$, is negligible as $\rho/\rho_{\rm s} \ll 1$.

Analysis of the calculations enables one to find the conditions and mechanisms relevant to particle ignition. It turned out that magnesium particles ignite at $M_0 \in (2.5,\ 2.75)$ depending on the particle size. The predicted time histories of particle temperature $T = T(t)$ are presented in Fig. 6.16 to illustrate the effect of M_0 at $d_{\rm s0} = 100$ μm and $p_0 = 1$ bar. In dynamic

conditions, the limiting medium temperature $\tilde{T}_{\rm cr}$, at which ignition is still possible, is much lower than in the static conditions. Thus, for magnesium particles with $d_{\rm s0} = 100\,\mu$m, $\tilde{T}_{\rm cr} = 640$–$710\,$K behind the incident shock wave, while $\tilde{T}_{\rm cr} = 920\,$K in static conditions. This difference is explained by an increase in the heat flux to the particle owing to higher values of the coefficient for heat transfer between the gas and the particle.

It was found that at $M_0 < 4.5$ magnesium particles ignite according to the thermal explosion mechanism, while at $M_0 > 4.5$ they ignite as a result of fragmentation. The corresponding ignition criteria are the conditions $T \geq T_{\rm mel}$, where $T_{\rm mel}$ is the particle melting temperature, and $We > We_{\rm cr}$, where We is the Weber number (and $We_{\rm cr} \approx 12$ is the critical Weber number at which fragmentation starts). In the calculations, the ignition delay time is taken as the least of the times of fragmentation and ignition by the thermal mechanism. The ignition due to the thermal mechanism was not found under the conditions specified. Note that "thermal explosion" was observed in computations after the particle reached a temperature less than the magnesium melting temperature. Besides comparison of the flow dynamic parameter u, the predicted and measured data of [27] were compared in terms of the dependence of the ignition delay time $t_{\rm ign}$ on the postshock temperature. The latter is shown in Fig. 6.17. With use of the kinetic constants obtained, the computations were carried out, which allowed one to extend the approximation of [27] for the ignition delay time for magnesium particles of different sizes:

$$t_{\rm ign} = A \left(\frac{d_{\rm s0}}{17} \right)^m p_0^n \exp\left(\frac{E_*}{RT} \right),$$

where $A = 1.203 \times 10^4\,{\rm m\,s\,(bar)}^{-n}$, $n = -0.866$, $m = 1.7$, and $E_* = 6.4 \times 10^7\,{\rm J\,kmol}^{-1}$. Similar calculations with aluminum particles showed that aluminum particles ignite following the thermal ignition mechanism (Fig. 6.18). The predicted value of $t_{\rm ign}$ for aluminum particles in dynamic conditions

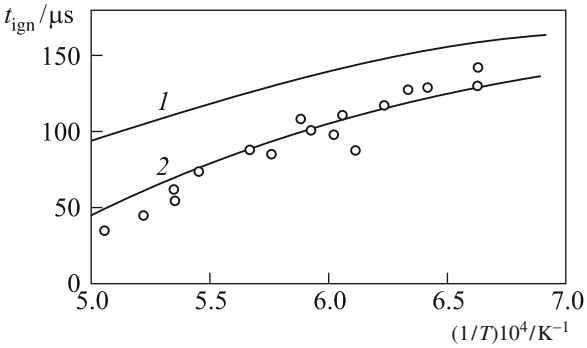

Fig. 6.17. Comparison of measured (*symbols*) and predicted (*solid curves*) data on the dependence of ignition delay time of magnesium particles on the temperature behind the incident shock wave

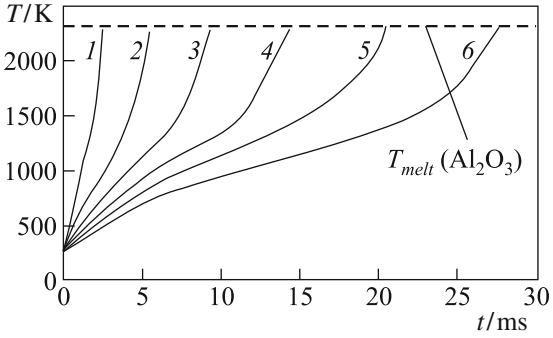

Fig. 6.18. Computed temperature curves for the aluminum particle

proved to be much less than that in static conditions. Aluminum particles with $d_{s0} \leq 100\,\mu$m ignite in the incident shock wave with a Mach number exceeding 3.2–3.7 (depending on the particle size).

6.3 Ignition of Liquid Drops

Single liquid drop and spray behavior behind an incident shock wave differs considerably from single solid particle and particle suspension behavior. It is commonly accepted that hydrocarbon drop ignition occurs in the vapor phase. Therefore, a considerable increase in the specific surface area of drops caused by their aerodynamic deformation and fragmentation in the shock-induced gas flow is considered as one of the most important phenomena affecting interphase mass, momentum, and energy exchange rates, and finally ignition. Interaction of drops with gaseous flow is governed, on the one hand, by liquid properties, the size and the shape of the drops, and the spacing between drops and, on the other hand, by local properties of gas flow. The situation is significantly complicated by the fact that the phases interact with each other dynamically and thermally. There are hundreds of publications in which these interactions have been studied both experimentally and theoretically.

Here, we analyze only those physical and chemical phenomena which are directly relevant to drop ignition behind shock waves. In particular, we are interested in specific features of the molecular mixing of fuel with air at the mixture formation stage and at autoignition of the two-phase mixture behind the shock wave. Liquid fuels considered are low-viscosity n-alkanes or hydrocarbon fuels such as gasoline and kerosene.

6.3.1 Drop Deformation

Drop deformation in the flow is the process which is capable of influencing the interphase mass, momentum, and energy transfer. In theoretical models,

a deformed drop is usually represented as an ellipsoid of revolution with large half-axis b and small half-axis a. The drop deformation degree, Δ, is defined as the ratio of a to radius r_s of a spherical drop of the same volume, $\Delta = a/r_\mathrm{s}$. Note that in the course of deformation, a drop can take a shape resembling either an oblate or a prolate ellipsoid of revolution.

One can distinguish at least four mechanisms of drop deformation that can influence heat and mass transfer with the gas flow: (1) variation of the deformed drop cross-sectional area A, (2) variation of the total surface area of the drop S, (3) variation of the aerodynamic drag coefficient C_D of the deformed drop, and (4) variation of the heat transfer coefficient k_h between the gas and the deformed drop.

The maximal variations of cross-sectional area $A = \pi b^2$ and total surface area S are determined by the maximum possible deformation degree at which deformation is still reversible, i.e., there is still no drop fragmentation. According to [120,121], the maximum drop deformation degree is $\Delta = 0.25$–0.44. Hence, the ratio of cross-sectional areas of the deformed and spherical drops can attain values of 2.25–4. The ratio of S to the surface area of the corresponding spherical drop can attain values of 1.3–2.1.

The aerodynamic drag coefficient C_D for a deformed drop differs from that for a spherical drop. At high Reynolds numbers of relative motion of the drop and gas, C_D is approximately equal to 0.44 [122]. At such conditions, C_D for deformed drops can attain values of 1.6–2.2 [121], 1.8–3.0 [123], or 2.3 [124], i.e., values considerably larger than for a spherical drop.

The heat transfer coefficient k_h also depends on the drop shape. For example, if the deformed drop is characterized by the equivalent Sauter mean diameter $d_\mathrm{eff} = 6V/S$, where V is the ellipsoid volume, then to determine k_h one can use the approximate relationship [125]

$$Nu = \frac{k_\mathrm{h} d_\mathrm{eff}}{\lambda} = 2.0 \exp\left[-2.22\left(\frac{d_\mathrm{eff}}{2b} - 1\right)\right]. \tag{6.23}$$

This relationship indicates that for a deformed drop with $\Delta = 0.25$–0.44, the heat transfer coefficient can exceed the typical value for the spherical particle by a factor of 3–5.4 even at zero relative velocity of gas and the particle, $U = 0$.

Thus, increasing A and C_D can affect the dynamics of drop motion in the gas flow, leading to faster relaxation of the relative velocity U and therefore a reduction in heat and mass transfer. The reverse, an increase of S and k_h, leads to intensification of heat and mass transfer. The net effect of the deformation of the drop on its heating and vaporization in the gas flow depends on specific conditions.

There exist several models of drop deformation [126–130]. In the existing models of drop ignition behind a shock wave, drop deformation is either not taken into account at all [131–136] or regarded using a simplified model, which does not reflect the features discussed above [137–140]. Note that drop

deformation is a complex process including excitation of internal liquid circulations [141, 142] and drop oscillations as a whole. In the course of deformation, a drop can attain asymmetrical shapes which are far from resembling the ellipsoid of revolution [143].

6.3.2 Single Drop Vaporization

In the postshock gas flow, the interfacial strain results in internal liquid circulation in the drop, and the conductive heat transfer is complemented by convective heat transfer [3, 141–143]. Starting from certain values of the liquid Reynolds number, the convective mechanism becomes dominant [3, 142]. Internal liquid circulation in the deformed drop can differ considerably from that in a spherical drop [2, 3]. In [144], a mathematical model of deformed drop heating and vaporization was suggested.

Initially, at time $t = 0$, a spherical drop of radius r_{s0} is placed in the postshock gas flow. Owing to the aerodynamic drag force, the drop accelerates, deforms, heats up, and vaporizes. In addition, internal liquid circulation is induced in the drop. The task is to determine the rate of drop vaporization and the drop lifetime in these conditions. Assume that the drop takes the shape of an ellipsoid of revolution. The properties of the liquid will be denoted by index l and the parameters at the drop surface by index i. In this step, we will restrict ourselves by considering the situations when the drop deformation does not attain the critical stage followed by drop breakup. From Sect. 6.2.3.2, drop breakup occurs at Weber number $We{=}d_{s0}\rho U_0^2/\sigma_l \geq 12$, where σ_l is the surface tension, and $d_{s0} = 2r_{s0}$ is the spherical drop diameter. The critical deformation stage is attained at $\Delta = 0.25$–0.44 or $b/r_s = 1.5$–2.0 [129].

To determine the most important geometrical parameters of the drop – b, a, A, and S – we use the deformation equation [130]:

$$\frac{\mathrm{d}^2 y}{\mathrm{d}t^2} = \frac{C_F}{C_b}\frac{\rho}{\rho_l}\frac{U^2}{r_s^2} - \frac{C_k\sigma_l}{\rho_l r_s^3}y - \frac{C_d\mu_l}{\rho_l r_s^2}\frac{\mathrm{d}y}{\mathrm{d}t}, \tag{6.24}$$

where $y = \delta/(C_b r_s)$ is the dimensionless deformation, δ is the displacement of the drop equator from the equilibrium position in the plane normal to the direction of the relative velocity U, and $C_b = 0.5$, $C_F = 0.333$, $C_k = 8$, and $C_d = 5$ are the dimensionless coefficients. The initial conditions for (6.24) are

$$t = 0: \; y = 0; \; \frac{\mathrm{d}y}{\mathrm{d}t} = 0. \tag{6.25}$$

For an ellipsoid of revolution, the large half-axis b is equal to $b = r_s + \delta = r_s(1 + C_b y)$. The small half-axis a can be determined from the condition of constant drop volume during deformation: $V = (4/3)\pi a b^2 = (4/3)\pi r_s^3$. Parameters A and S can then be readily determined.

The equation of heat balance for the deformed drop can be written in the form

$$c_{\mathrm{l}} m \frac{\mathrm{d}T}{\mathrm{d}t} = Q_{\mathrm{i}-} \tag{6.26}$$

where $m = V\rho_{\mathrm{l}}$ is the drop mass, and $Q_{\mathrm{i}-}$ is the total heat flux from the drop surface to drop interior (index $i-$ means that the value of the heat flux is taken at the drop surface from the liquid side). Heat flux $Q_{\mathrm{i}-}$ is a function of temperature and velocity fields inside the drop, i.e., $Q_{\mathrm{i}-} = f(t, T_{\mathrm{i}}, T, u_{\mathrm{i}}, \ldots)$, where u_{i} is the liquid velocity at the drop surface. Heat flux $Q_{\mathrm{i}+}$ from the gas side (index $i+$ means that the value of the heat flux is taken at the drop surface from the gas side) for the evaporating drop is given by the relationship

$$Q_{\mathrm{i}+} = Q + L\frac{\mathrm{d}m}{\mathrm{d}t},$$

where Q is the full heat flux toward the drop from the gas phase and L is the latent heat of vaporization. Owing to continuity of heat flux, $Q_{\mathrm{i}-} = Q_{\mathrm{i}+}$, and (6.26) takes the form

$$c_{\mathrm{l}} m \frac{\mathrm{d}T}{\mathrm{d}t} = Q + L\frac{\mathrm{d}m}{\mathrm{d}t}. \tag{6.27}$$

The initial conditions for (6.27) are formulated as follows:

$$t = 0: \; T = T_0. \tag{6.28}$$

The heat flux Q in (6.27) is given by the relationship $Q = Sq_{\mathrm{h}}$, where q_{h} is the heat flux per unit surface area of the drop. To determine q_{h} one can apply Newton's law $q_{\mathrm{h}} = k_{\mathrm{h}}(\tilde{T}_{\infty} - T_i)$ with ∞ denoting gas properties at a large distance from the drop surface. Note that Newton's law is applicable only to the steady-state heat transfer. Nevertheless, as shown in [145], it can be applied to problems of transient heat transfer by introducing an effective thermal conductivity of gas. In the standard drop vaporization model [146], it is assumed that $\lambda = \lambda\left(\overline{T}\right)$, where $\overline{T} = \left(\tilde{T} + T_i\right)/2$ is some characteristic gas temperature. The heat transfer coefficient k_{h} in Newton's law is given by [2, 145]

$$k_{\mathrm{h}} = \frac{Nu}{d_{\mathrm{eff}}}\lambda\frac{\ln(1+B)}{B}, \tag{6.29}$$

where B is the mass transfer coefficient. In general, the Nusselt number in (6.29) depends on the drop shape [see (6.23)] and the Reynolds number based on the relative velocity $Re = d_{\mathrm{eff}}\rho\,|U|/\mu$. In the absence of proper relationships for deformed drops, it is worthwhile utilizing the corresponding dependence $Nu = Nu(Re)$ for a spherical drop [147] as a first approximation:

$$Nu = 2.0\,\exp\left[-2.22\left(\frac{d_{\mathrm{eff}}}{2b} - 1\right)\right] + 0.6\,Re^{1/2}Pr^{1/3}, \tag{6.30}$$

where $Pr = \mu/\rho a_{\mathrm{T}}$ is the Prandtl number and a_{T} is the gas thermal diffusivity. Relationship (6.30) indicates that, at high Reynolds numbers, the Nusselt number for a spherical drop in air can attain values up to an order of magnitude higher than 2.0.

The Reynolds number can be determined from the solution of the drop motion equations (6.18) with the initial condition

$$t = 0: \ u = u_0. \tag{6.31}$$

For the evaporating drop, the aerodynamic drag coefficient C_{D} depends not only on the drop shape, but also on the mass transfer coefficient B and on the physical properties of the gas and liquid, which determine the liquid velocity at the drop surface.

The effect of B on C_{D} is usually taken into account as $C_{\mathrm{D}} = C_{\mathrm{D,ne}}/(1+B)$ [2], where $C_{\mathrm{D,ne}}$ is the aerodynamic drag coefficient of a nonevaporating drop. The effect of drop shape on the value of $C_{\mathrm{D,ne}}$ can be taken into account using the relationship [148] $C_{\mathrm{D,ne}} = C_{\mathrm{Ds,ne}}(1+2.632y)$. The aerodynamic drag coefficient of a solid sphere $C_{\mathrm{Ds,ne}}$ is equal to [149]

$$C_{\mathrm{Ds,ne}} = \begin{cases} \dfrac{24}{Re}\left(1 + 0.15\, Re^{0.687}\right) & \text{at } Re < 10^3 \\ 0.44 & \text{at } Re \geq 10^3 \end{cases}.$$

Thus, at high Reynolds numbers and large drop deformations ($y \approx 1$), $C_{\mathrm{D,ne}}$ may attain the value of 1.5 typical for a disk-shaped body. This value is larger by a factor of 3.4 than the value $C_{\mathrm{Ds,ne}} = 0.44$ typical for a spherical body.

The effect of liquid motion on the drop surface on the value of $C_{\mathrm{Ds,ne}}$ can be taken into account by using the results of numerical calculations [143]:

$$\frac{C'_{\mathrm{Ds,ne}}}{C_{\mathrm{Ds,ne}}} = \left(\frac{2 + 3\mu_{\mathrm{l}}/\mu}{3 + 3\mu_{\mathrm{l}}/\mu}\right)\left(1 - 0.03\frac{\mu}{\mu_{\mathrm{l}}} Re^{0.65}\right),$$

where $C'_{\mathrm{Ds,ne}}$ is the aerodynamic drag coefficient of a spherical liquid drop. The latter relationship approximates well the analytical results at low and high Reynolds number, but its application is, in general, limited by the range of viscosity ratios μ_l/μ, studied in [143].

The mass transfer coefficient B is defined as $B = (Y_{\mathrm{v}i} - Y_{\mathrm{v}\infty})/(1 - Y_{\mathrm{v}i})$ [2, 145], where index v relates to the liquid vapor and Y is the mass fraction.

The rate of drop mass variation due to vaporization required in (6.27) is found from the equation

$$\frac{\mathrm{d}m}{\mathrm{d}t} = -Sj, \tag{6.32}$$

where $j = 2\rho D \ln(1+B)/d_{\mathrm{eff}}$ is the vapor mass flow rate per unit drop surface area [2, 145] and D is the binary diffusion coefficient for the gas and vapor.

The initial condition for (6.32) is

$$t = 0: \ m = m_0. \tag{6.33}$$

Many of the relationships discussed above contain, explicitly or implicitly, the drop surface temperature T_i. In particular, T_i plays an important role in determining heat flux $Q_{\mathrm{i}-}$. To determine T_i, the following considerations will be used.

When the mean drop temperature T attains the value of the saturation temperature ("wet-bulb" temperature) $T_\mathrm{i} = T_\mathrm{wb}$, the heat flux to the drop interior vanishes, i.e., $Q_{\mathrm{i}-} = Q_{i+} = 0$, and the entire heat flux Q is consumed for liquid vaporization. The initial period in drop evolution, when $Q_{\mathrm{i}-} \neq 0$ or $T < T_\mathrm{wb}$, is referred to as the transient heating period. The period when $Q_{\mathrm{i}-} = Q_{\mathrm{i}+} = 0$ or $T = T_\mathrm{wb}$ is referred to as the period of quasi-steady drop vaporization. In the latter case, instead of (6.27), one can write $T = T_\mathrm{i} = T_\mathrm{wb}$ and $Q = \ell \mathrm{d}m/\mathrm{d}t$. Denote the duration of the transient heating period as t_h, the duration of the quasi-steady vaporization period as Δt, and the total lifetime of the drop as t_l. Then $t_\mathrm{l} = t_\mathrm{h} + \Delta t$.

In accordance with [144], internal liquid circulation in the drop can result in a considerable decrease of the transient heating period t_h compared with the standard case when only conductive heat transfer is taken into account. At $t \geq t_\mathrm{h}$, internal circulation exerts no effect on the drop vaporization dynamics. This means that at $t > t_\mathrm{h}$ the drop evaporates independently of internal convective flows. Thus, internal liquid circulation can decrease the drop lifetime by no more than the value of t_h. Note that in the standard model of spherical drop vaporization without internal circulation the duration of the transient heating period for heavy hydrocarbon drops can be rather long (up to $t_\mathrm{h} \approx t_\mathrm{l}$), in particular at high gas temperatures and pressures [149].

The effect of internal liquid circulation on drop heating during the transient period can be taken into account by introducing the coefficient of internal heat transfer intensification, $\theta = t_\mathrm{h}/t_\mathrm{h}^\mathrm{o} \leq 1$, i.e., $Q_{\mathrm{i}-} = \theta^{-1} Q_{\mathrm{i}-}^\mathrm{o}$, where index o relates to a spherical drop without internal liquid circulation. To determine θ one can use the results of the numerical solution to the problem of spherical drop heating in the gas flow together with the approximation of constant surface temperature $T_\mathrm{i} = \mathrm{const}$ [144].

To substantiate the possibility of using such an approximation, let us determine the wet-bulb temperature T_wb. Substituting the above relationships into the condition $Q_{\mathrm{i}-} = 0$ gives the following algebraic equation for $T_\mathrm{i} = T_\mathrm{wb}$:

$$Nu\,\lambda(\tilde{T}_\infty - T_\mathrm{i}) = 2\rho D L \frac{Y_\mathrm{vi} - Y_{\mathrm{v}\infty}}{1 - Y_\mathrm{vi}}. \tag{6.34}$$

In (6.34), λ, ρ, D, L, and Y_vi are the functions of temperature T_i; therefore, its solution is found by iteration. To check the validity of (6.34), detailed numerical calculations of spherical drop heating and vaporization were performed using the model in [149], which does not take into account relative motion of the

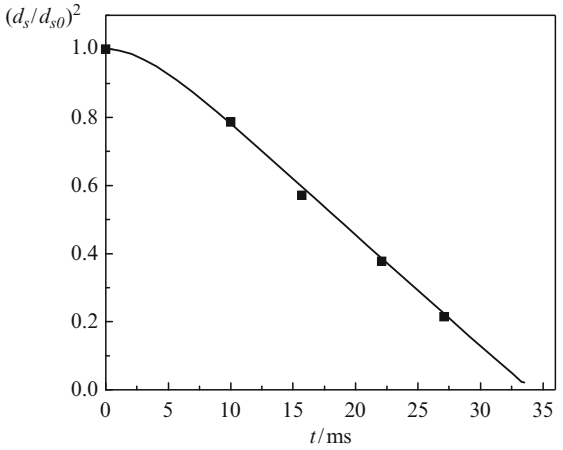

Fig. 6.19. Comparison of predicted (*curve*) and measured (*points*) dynamics of n-heptane drop surface regression at vaporization in air, $d_{s0} = 70\,\mu$m, $T_0 = 293.15\,$K, and $\tilde{T} = 573.15\,$K [149]

drop and gas. In the computational code [149], partial differential equations for both liquid and gas phases are solved using the approximation of multicomponent diffusion for the gas phase and variable thermophysical properties of phases. To demonstrate the predictive capability of the model [149], Fig. 6.19 shows a comparison of predicted and measured drop surface regression curves for an n-heptane drop. In the simplest standard model of drop vaporization based on the quasi-steady vaporization law, the dependence $d^2(t)$ is known to be linear. In the model of [149] this dependence is more complex: owing to liquid thermal expansion the $d^2(t)$ function exhibits nonlinear behavior.

The solid and dashed curves in Fig. 6.20 show the predicted dynamics of surface temperature T_i and mean temperature T for an n-dodecane drop [144]. The horizontal dash-and-dot line corresponds to the solution of (6.34) at $Nu = 2.0$. Termination of the curves in Fig. 6.20 corresponds to complete drop evaporation (lifetime t_l). Recall that the transient heating period duration t_h is the time taken for the mean drop temperature to attain the value of the wet-bulb temperature.

Analysis of Fig. 6.20 as well as the results of calculations at other values of $\tilde{T}$ and p and for other liquids (n-heptane, n-octane, methanol, etc.) result in the following conclusions:

1. The time taken for the drop surface temperature T_i to attain a value close to the wet-bulb temperature T_wb is considerably less than the total drop lifetime t_l, in particular at high gas temperatures $\tilde{T}$.
2. At high gas temperatures, the duration of the transient heating period t_h is comparable with the total drop lifetime t_l.

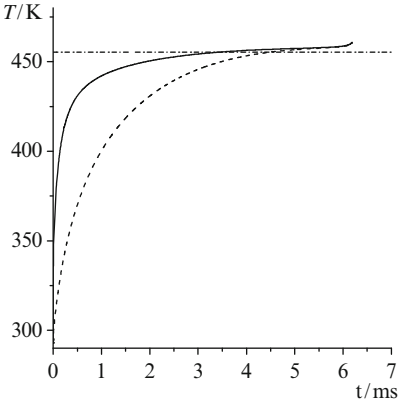

Fig. 6.20. Predicted time histories of surface (*solid curve*) and mean (*dashed curve*) temperatures of a vaporizing *n*-dodecane drop 50 μm in diameter at $T_0 = 293\,\mathrm{K}$, $p = 0.1\,\mathrm{MPa}$, and $\tilde{T} = 1,500\,\mathrm{K}$ [144]. The *dash-and-dot line* corresponds to the wet-bulb temperature found from (6.34)

3. Equation (6.34) provides a good estimate for the wet-bulb temperature T_{wb} over a wide range of gas temperatures and pressures, as well as for the physical properties of the liquid.

If the drop is placed in the postshock gas flow, the values of the wet-bulb temperature will be somewhat different from the value relevant to drop vaporization in a quiescent atmosphere. This is evident from (6.34). At $Re \neq 0$, the Nusselt number in (6.34) can be estimated on the basis of (6.30) for a spherical drop.

To understand how the Nusselt number affects the wet-bulb temperature, additional calculations have been performed. Variation of the wet-bulb temperature with Nusselt number is most pronounced at high pressures and low gas temperatures. Nevertheless, the wet-bulb temperature for liquid drops in the gas flow can differ by no more than 30–40 K compared with the quiescent conditions with $Nu = 2$. Fig. 6.21 demonstrates this implication for *n*-dodecane drops.

Thus, the results obtained allow one to adopt an important assumption that the drop surface temperature T_{i} attains the value of T_{wb} instantaneously, i.e., $T_{\mathrm{i}} = T_{\mathrm{wb}} = \mathrm{const}$. This assumption makes it possible to simplify considerably the modeling of drop heating, using (6.34) to determine the wet-bulb temperature at $Nu = 2$. To find the value of θ, one can use the results in [144].

Figure 6.22 shows the predicted dependencies of the mean *n*-heptane drop temperature on the normalized time t/t_{h}^{o} at different liquid Reynolds numbers $Re_{\mathrm{l}} = \rho_{\mathrm{l}} u_{\mathrm{i}} r_{\mathrm{s}}/\mu_{\mathrm{l}}$ [144]. The calculations were performed using the approach in [144]. Clearly, internal circulation leads to a significant reduction of the transient heating period t_{h}. To generalize the results, detailed calculations of drop heating in constant and variable dynamic conditions were

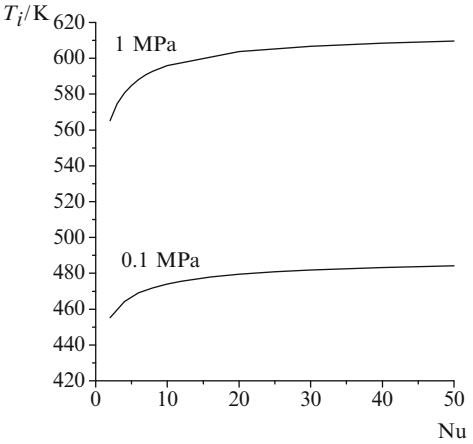

Fig. 6.21. Predicted dependencies of the wet-bulb temperature $T_{\rm wb}$ on the Nusselt number Nu for n-dodecane drops at $\tilde{T} = 1,500\,\mathrm{K}$ and $p = 0.1$, and 1 MPa [149]

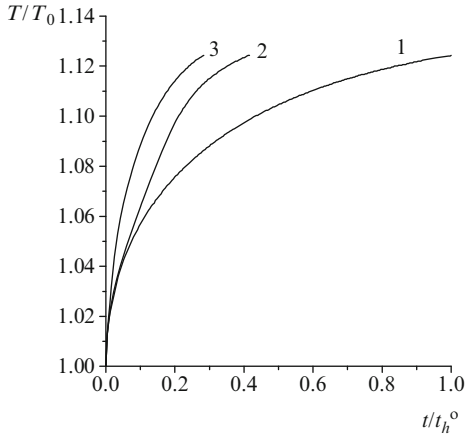

Fig. 6.22. Predicted dependencies of the mean temperature of spherical n-heptane drop on normalized time at $T_0 = 300\,\mathrm{K}$, $\tilde{T} = 750\,\mathrm{K}$, $p = 0.1\,\mathrm{MPa}$, and $d_{s0} = 200\,\mu\mathrm{m}$ [149]. Curve 1 corresponds to $Re_l = 0$, curve 2 to $Re_l = 1.3$, and curve 3 to $Re_l = 13$

performed. In constant dynamic conditions, the relative velocity was kept constant ($U = U_0$), whereas in variable dynamic conditions drop heating was calculated with regard to drop motion according to (6.18) with initial conditions (6.31). The following correlation for the mean coefficient θ was suggested in [144]:

$$\begin{aligned} &\theta = 1 && \text{at} \quad Re_l \le Re_l^*, \\ &\theta = C_1 \log Re_l + C_2 && \text{at} \quad Re_l^* < Re_l < Re_l^{**}, \\ &\theta = C_3 \log Re_l + C_4 && \text{at} \quad Re_l > Re_l^{**}, \end{aligned} \tag{6.35}$$

Table 6.5. Characteristic Reynolds numbers $Re_l = \rho_l u_i r_s / \mu_l$

Liquid	Re_l^*	Re_l^{**}
n-Heptane	0.59	11.60
n-Dodecane	0.19	3.74

Table 6.6. Coefficients in approximation relationships for θ

Liquid	C_1	C_2	C_3	C_4
n-Heptane	−0.410	0.910	−0.182	0.670
n-Dodecane	−0.395	0.700	−0.193	0.600

where Re_l^* and Re_l^{**} are some characteristic values of the Reynolds number. Their values and the values of the constants C_1, C_2, C_3, and C_4 for n-heptane and n-dodecane drops are presented in Tables 6.5 and 6.6. Thus, (6.35) allows one to account for the effect of internal liquid circulation on the heat and mass transfer of spherical liquid drops with gas flow at $t < t_h$.

To model deformed drop heating, one can assume, in addition to the assumptions adopted in [144], that drop deformation is quasi-static, i.e., the characteristic time required for the establishment of internal motion is small compared with the characteristic heating time of the drop. The validity of this assumption was checked by 3D numerical simulation of transient heating of deformed liquid drops. The mathematical statement of the problem for the deformed drop was similar to that for a spherical drop [142, 144], with one exception. Since the analytical solution for the internal flow field is available only for a spherical drop, the corresponding flow fields in the ellipsoidal drops were found from the steady-state solution of the Navier–Stokes equations with special boundary conditions on the drop surface.

On the basis of the calculated velocity fields inside the deformed drops, the equation of convective thermal conductivity was solved. As a result, a coefficient of heat transfer intensification for deformed drops θ' was derived. The calculations revealed that $\theta' \approx \theta\theta_f$, where $\theta_f = t_h^e / t_h^o$ (index e relates to the deformed drop without internal liquid circulation) is a function of drop shape only and is virtually the same for liquids with different physical properties (n-heptane, n-octane, n-dodecane, water, and methanol) at different intensities of internal liquid circulation. The results of the calculations were approximated by the second-order polynomial

$$\theta_f = -0.78 + 3.67\Delta - 1.89\Delta^2 \text{ at } \Delta < 1 \tag{6.36}$$

for the oblate ellipsoid of revolution

$$\theta_f = 0.65 + 0.77\Delta - 0.42\Delta^2 \text{ at } \Delta > 1 \text{ and} \tag{6.37}$$

for the prolate ellipsoid of revolution. The approximation error in (6.36) and (6.37) is less than 6%.

Coefficient $\theta_{\rm f}^{-1}$ can be treated as an additional correction factor to the heat flux $\dot{Q}_{\rm i-}$, i.e.,

$$\dot{Q}_{\rm i-} = \dot{Q}^{\rm o}_{\rm i-}(\theta\theta_{\rm f})^{-1}, \tag{6.38}$$

where θ and $\theta_{\rm f}$ are given by (6.35) and (6.36) or (6.37).

Differential equations (6.24), (6.27), (6.18), and (6.32) with initial conditions (6.25), (6.28), (6.31), and (6.33), as well as the additional relationships presented above allow one to predict the behavior of a liquid drop in the gas flow with regard to drop deformation, motion, transient heat transfer, and vaporization, and therefore to determine the drop lifetime. As compared with the standard vaporization model of a spherical drop, (6.23)–(6.37) include at least eight supplementary factors which can affect the drop lifetime in the gas flow. These are (1) internal liquid circulation, which affects the duration of the transient heating period from the initial temperature T_0 to the wet-bulb temperature $T_{\rm wb}$, (2) variation of drop surface area S, (3) variation of the heat transfer coefficient $k_{\rm h}$ owing to drop deformation, (4) variation of the heat transfer coefficient $k_{\rm h}$ owing to relative motion of the drop and gas, (5) variation of the deforming drop cross-sectional area A, (6) variation of the aerodynamic drag coefficient $C_{\rm D}$ owing to drop vaporization, (7) variation of $C_{\rm D}$ owing to drop deformation, and (8) variation of $C_{\rm D}$ due to liquid motion at the drop surface.

All these factors can be considered as corrections to a standard model. Since corrections 1–4 relate to the heat balance equation and corrections 5–8 relate to the drop motion equation, they can be conditionally referred to as "thermal" and "dynamic" corrections, respectively. These corrections can be readily introduced into the standard model [146]. Below we show some examples of calculations with and without these corrections. The problem was solved by the Runge–Kutta method of the fourth order for drops of various primary hydrocarbons at different temperatures and pressures of ambient air and at different Weber numbers determining drop deformation. Thermophysical properties of liquids were treated as functions of pressure and temperature.

The results of calculations with corrections 1–8 were compared with the results predicted by the model in [146] at $U \neq 0$ ($We_0 \neq 0$). The calculations revealed that the most pronounced effect on the drop lifetime is produced by "thermal" corrections 1–4, whereas "dynamic" corrections 5–8 play an insignificant role.

Figure 6.23 shows the predicted time histories of "fine" ($d_{\rm s0} = 25\,\mu$m) n-dodecane drops at $\tilde{T} = 1,000\,$K, $T_0 = 300\,$K, and $p = 1\,$MPa, and different Weber numbers. Solid curves correspond to the model in [146] and dashed curves to the modified model in [146] with "thermal" corrections 1–4 [144].

Analyzing the computational results at different values of d_{s0}, $\tilde{T}$, p, and We, one comes to the following conclusions regarding the effect of "thermal" corrections 1–4 on the drop lifetime:

1. Corrections can result in a considerable reduction of drop lifetime (up to a factor of 2.5).

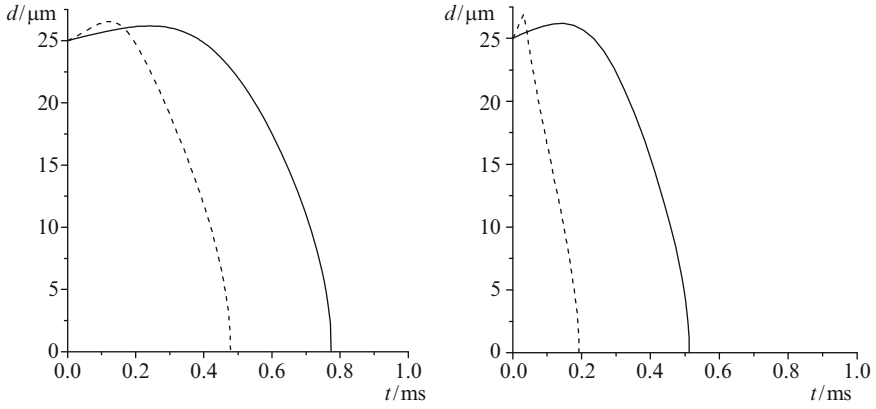

Fig. 6.23. Time histories of *n*-dodecane drop diameter predicted by the standard model (*solid curves*) and the modified standard model with "thermal" corrections 1–4 (*dashed curves*) at $d_{s0} = 25\,\mu\text{m}$, $\tilde{T} = 1,000\,\text{K}$, $T_0 = 300\,\text{K}$ and $p = 1\,\text{MPa}$ [144]. **a** $We_0 = 0.2$; **b** $We_0 = 12$

2. The effect of corrections on drops of less volatile fuel is more pronounced.
3. The effect of corrections increases with Weber number We.
4. The effect of corrections increases with pressure p.
5. The effect of corrections increases with gas temperature $\tilde{T}$.
6. The variation of d_{s0} is not virtually reflected in the effect of corrections.

The less pronounced effect of "thermal" corrections on the volatile fuel drop lifetime is explained by a shorter transient heating period t_h.

6.3.3 Drop Breakup

From physical reasoning and dimensional analysis, breakup is governed by the following basic dimensionless numbers representing ratios of the forces: aerodynamic force to surface tension, or Weber number $We = \rho U^2 d_s/\sigma_l$, aerodynamic force to viscous force in the gas phase, or Reynolds number $Re = \rho\,|U|\,d_s/\mu$, and viscous force to surface tension in the liquid phase, or Ohnesorge number $Oh = \mu_l/(\rho_l \sigma_l d_s)^{1/2}$. The Ohnesorge number comes into play when the viscosity of a liquid is high; therefore, when breakup of inviscid liquids (such as hydrocarbons) for which $Oh < 0.1$ is considered, its effect on mass transfer can be neglected. Generally, depending on the Weber number, the breakup modes appear as shown in Fig. 6.24 [150].

The figure illustrates schematically the sequence of breakup stages representing only their major features, many details have been omitted. Although the conditions for critical Weber numbers and for each particular breakup mode reported in various publications differ, the discrepancy is not that significant to deserve special discussion. In a strong shock wave spreading in sprays, the main droplet breakup mode is a combination of stripping (Fig. 6.24d)

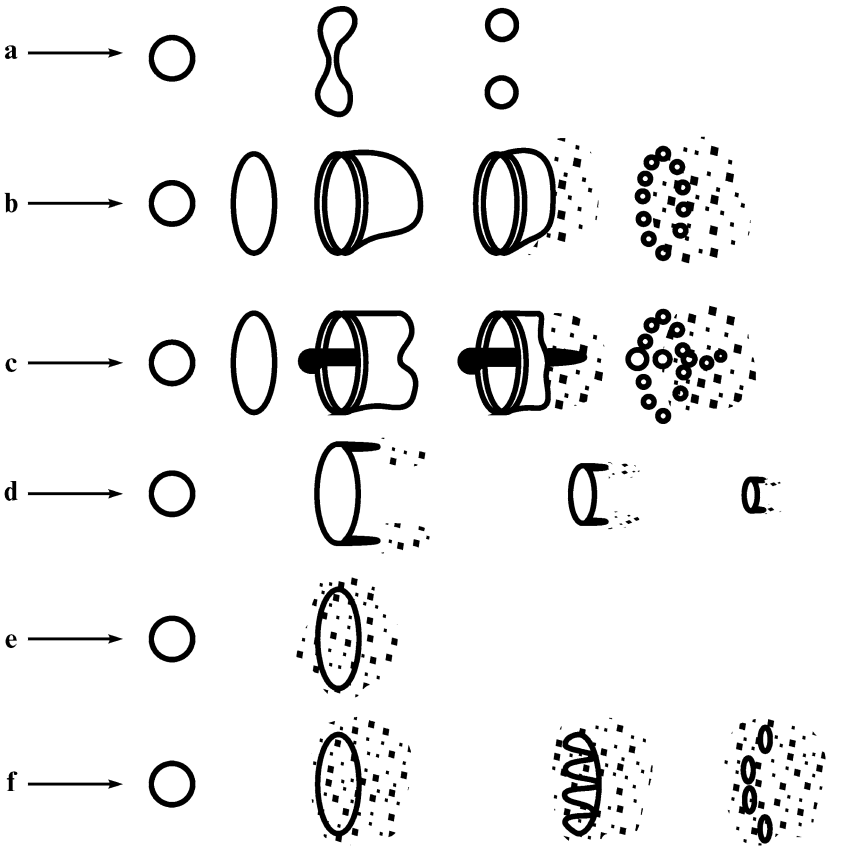

Fig. 6.24. Mechanisms of breakup of low-viscosity liquid drops observed experimentally [150]: **a** vibrational breakup $We < 12$, **b** bag breakup $12 < We < 50$, **c** bag-and-stamen breakup $50 < We < 100$, **d** sheet stripping $100 < We < 350$, **e** wave crest stripping $350 < We < 2,670$, and **f** catastrophic breakup $We > 2,670$. The *arrows* show the flow direction

and Rayleigh–Taylor (Fig. 6.24e) instability modes. These modes produce two sorts of secondary drop: micromist, as a result of disintegration of the stripped sheet, and larger drops arising after perforation of the parent drop with gaseous "fingers" due to Rayleigh–Taylor instability and the disintegration of the perforated disk.

From linear analysis, there is a minimum wavelength of instability waves $\lambda_{\mathrm{w}} = 2\pi \left(\sigma_{\mathrm{l}}/\rho_{\mathrm{l}} a_{\mathrm{d}}\right)^{1/2}$ (where a_{d} is the drop acceleration) below which their amplitude does not grow [151]; hence, drops of size less than λ_{w} are not subjected to Rayleigh–Taylor instability. According to [151], behind a shock wave with $M = 3.0$, λ_{w} ranges between 23 and 63 μm. Unfortunately, available experimental data pertain to larger drops; therefore, breakup patterns of fine drops require additional experimental verification.

Breakup modes inherent in lower Weber numbers are important for weak shock waves. Usually they do not result in such a dramatic increase of the evaporating surface area as do the stripping and Rayleigh–Taylor instability modes. But there is one process where these modes can significantly change the burning process. This is the transition from deflagration of a spray to detonation, which is significantly stimulated by sending weak shock waves into a burning spray.

6.3.4 Cloud of Breakup Fragments

One of the most important questions relevant to the drop ignition phenomenon behind a shock wave is how fast the fuel is mixed with the oxidizer on a molecular level. The answer to this question presumes knowledge of (1) the total breakup times and (2) the state and geometry of the two-phase cloud arising after the breakup. The representative time of drop deformation, and hence breakup, following from dimensional analysis is $t^* = d_\mathrm{s}\left(\rho_\mathrm{l}/\rho\right)^{1/2}/U$; therefore, for convenience the total breakup time is usually expressed in t^* units. The reduced breakup times τ for low-viscosity liquids range between 3.5 and 6. Pilch and Erdman [150] reported empirical formulas relating τ to Weber number:

$$
\begin{aligned}
&\tau = 6\left(We - 12\right)^{-0.25} \text{ at } 18 \geq We \geq 12,\\
&\tau = 2.45\left(We - 12\right)^{-0.25} \text{ at } 45 \geq We \geq 18,\\
&\tau = 14.1\left(We - 12\right)^{-0.25} \text{ at } 351 \geq We \geq 45,\\
&\tau = 0.766\left(We - 12\right)^{-0.25} \text{ at } 2,670 \geq We \geq 351,\\
&\tau = 5.5 \text{ at } We \geq 2,670.
\end{aligned}
$$

Thus, the fluid in the wake of a disintegrated drop is a mixture of the free-stream gas, fuel vapor, and secondary droplets of various sizes. Photographic studies fail to provide information about the state of the material in the wake of the drop because of strong light scattering by dispersed material. Even X-ray diagnostics [152] furnish data on the overall density of the mixture while indicating nothing about the structure and aggregate state of the mixture.

Figure 6.25 shows a photograph of a shattered water drop 0.3 mm in diameter in the shock-induced airflow behind the shock wave of Mach number 2.4. The totally opaque wake of the drop consists of very fine droplets. The amount of air entrained in the wake at $\tau = 3.1$ is estimated at about 450 times the volume of the original drop. If it were a hydrocarbon drop, rather than water, the equivalence ratio Φ averaged over the wake would be about 5. On the basis of a qualitative understanding of the drop breakup mechanism, one can only speculate that the cloud behind the drop has a shape close to conical and the main part of the fragments is concentrated at its periphery.

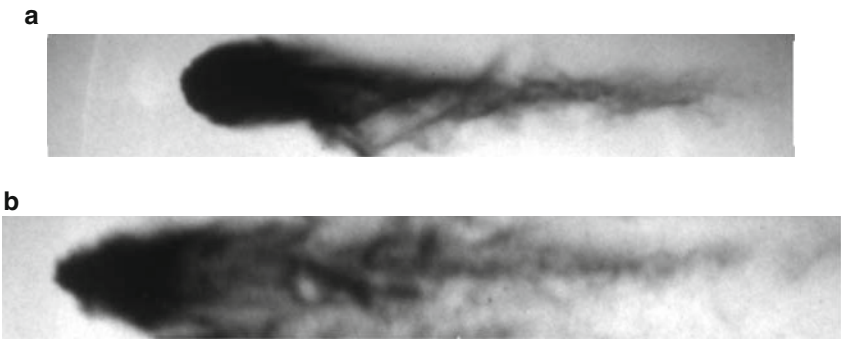

Fig. 6.25. Water drop (0.3 mm in diameter) shattered behind a shock wave with Mach number 2.4 at $\tau = 2.5$ **a** and 3.1 **b**, respectively. The initial air pressure is 1 atm

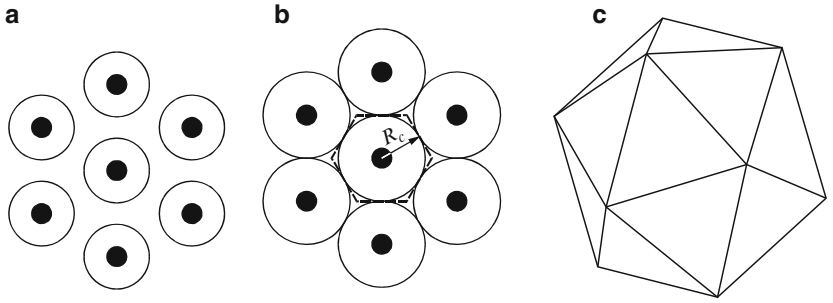

Fig. 6.26. Elementary cell for the uniform monodisperse drop suspension [153,154]. *Black circles* denote drops. *Circumferences around drops* characterize the spread of diffusion fluxes from individual drops. In **a**, spray effects are absent, while in **b** spray effects start to appear. The *dashed line* bounds the elementary cell with zero mass and energy fluxes through its surface. R_c is the characteristic cell size (half-distance between drops). In **c**, the 3D elementary cell is shown in the form of a regular polyhedron with 20 faces

6.3.5 Vaporization of Drops in Clouds

Consider a uniform monodisperse suspension of liquid fuel drops [153, 154]. In such a suspension, all drops have the same diameter and are located at the same distance from each other. The black circles in Fig. 6.26a and b show schematically the drops distributed equidistantly over the plane. The circumferences around the drops characterize the penetration depth of diffusion fluxes, i.e., the conditional boundaries of the regions in which vapor concentration and gas temperature differ from their values in the undisturbed surroundings. The parameters of the surroundings remain stationary until the circumferences do not touch each other (Fig. 6.26a). When the diffusion fluxes from neighboring drops meet each other (Fig. 6.26b), all parameters in the

interdrop space start varying in time. Obviously, at the process stage shown in Fig. 6.26a, the spray effects are absent (in the approximation of constant pressure). The spray effects begin to develop at the stage shown in Fig. 6.26b.

Owing to symmetry considerations, an elementary cell in the form of a hexahedron shown by the dashed line in Fig. 6.26b can be constructed around each drop. The mass, momentum, and energy fluxes through the faces of this cell should evidently be zero. The characteristic size of the cell R_c is the half-distance between drops. In 3D space, the elementary cell has the shape of a regular polyhedron with 20 faces in the form of equilateral triangles with face length R_c (Fig. 6.26c). Thus, drop behavior in the suspension can be modeled by solving the governing conservation equations for a single drop with symmetrical boundary conditions at the polyhedron faces. Polyhedron volume and surface area are equal to $V_c = (5\sqrt{2}/3)R_c^3$ and $S_c = 5\sqrt{3}R_c^2$, respectively.

To visualize the flow pattern in such an elementary cell, a transient 3D problem on the flow evolution around a porous sphere modeling an evaporating drop was solved in [153, 154]. The flow field in the computational domain appeared to be very close to the 1D spherically symmetric field. The distortions of the 1D flow field were observed only in the vicinity to the polyhedron vertices where some tangential energy fluxes and insignificant convective flows took place. In view of this, the 3D problem can be reduced to a 1D formulation with zero-flux boundary conditions at the surface of the elementary sphere of radius R_{sc}, volume $V_{sc} = \frac{4}{3}\pi R_{sc}^3$ and surface area $S_{sc} = 4\pi R_{sc}^2$. Using the condition of equal volumes of the elementary sphere and polyhedron $V_{sc} = V_c$, one can readily obtain the radius of the elementary sphere as $R_{sc} = (5\sqrt{2}/4\pi)^{1/3}R_c \approx 0.826R_c$. It appears that the surface areas of the elementary sphere and the polyhedron differ only by 1%, i.e., $S_{sc}/S_c \approx 0.99$. Despite the fact that the adopted approximation does not take into account the tangential mass, momentum, and energy fluxes existing at the periphery of the polyhedron cell, one can anticipate that the approximate solution of the problem will reflect the main features of heat and mass transfer phenomena in drop suspensions.[1]

The statement of the 1D spherically symmetrical problem is the same as that reported in [153, 154]. The model is based on nonstationary differential equations of conservation of mass and energy in liquid and gas phases with variable thermophysical properties. In the statements, a concept of multicomponent diffusion of reactive species is used for the mixture containing fuel vapor, oxygen, nitrogen, and various combustion products. The effect of liquid surface tension on drop evaporation rate is also taken into account. The model is formulated for constant-pressure conditions in the gas–drop system, i.e., $p = p_0 = \text{const}$.

[1] These implications are also valid for a localized region in a suspension with uniform spatial distribution of monodisperse drops. In realistic nonuniform two-phase flows with polydisperse drops, one can also distinguish localized regions with such prerequisites owing to dynamic stratification of drop size fractions.

Initially, at $t = 0$, the radius of an elementary polyhedron cell R_c can be found on the basis of the mass content of liquid in the unit volume of a drop suspension, $\eta \ll \rho_l$, and the initial drop radius r_{s0}:

$$R_c \approx \left(4\pi/5\sqrt{2}\right)^{1/3} r_{s0} \left(\rho_l/\eta\right)^{1/3} \approx 1.211 r_{s0} \left(\rho_l/\eta\right)^{1/3}, \tag{6.39}$$

or on the basis of the fuel–air ratio $\Phi = \eta/(\phi_{st}\rho)$:

$$R_c \approx \left(4\pi/5\sqrt{2}\right)^{1/3} r_{s0} \left[\rho_l/\left(\rho\Phi\varphi_{st}\right)\right]^{1/3} \approx 1.211 r_{s0} \left[\rho_l/\left(\rho\Phi\varphi_{st}\right)\right]^{1/3}, \tag{6.40}$$

where ϕ_{st} is the stoichiometric fuel–air ratio.[2] The radius of the spherical elementary cell can be derived from (6.39) and (6.40):

$$R_{sc} \approx r_{s0} \left(\rho_l/\eta\right)^{1/3} \approx r_{s0} \left[\rho_l/\left(\rho\Phi\phi_{st}\right)\right]^{1/3} \tag{6.41}$$

At normal conditions, for stoichiometric mixtures of hydrocarbon fuels with air $\rho = 1.19\,\mathrm{kg\,m^{-3}}$, $\rho_l = 700$–$800\,\mathrm{kg\,m^{-3}}$, $\phi_{st} \approx 0.06$, and $\Phi = 1$; hence, $\eta = \eta_{st} \approx 0.07$–$0.08\,\mathrm{kg\ m^{-3}}$, $R_c/r_{s0} \approx 25$–27, and $R_{sc}/r_{s0} \approx 21$–22. At elevated pressures, for example, at the end of the compression stroke in a diesel engine ($\rho_g \approx 30\,\mathrm{kg\,m^{-3}}$), $R_c/r_{s0} \approx 9$ and $R_{sc}/r_{s0} \approx 8$.

Since the statement of the problem implies that $p = \mathrm{const}$, R_{sc} (and R_c) is time-dependent, i.e., $R_{sc} = R_{sc}(t)$. The value of $R_{sc}(t)$ should be determined in the course of the solution allowing the boundary of the spherical elementary cell $r = R_{sc}$ to move with gas. Thus, the boundary conditions at $r = R_{sc}$ are written in the form

$$r = R_{sc}(t): \quad \frac{\partial \tilde{T}}{\partial r} = 0, \quad \frac{\partial Y_j}{\partial r} = 0 (j = 1, 2, \ldots, M), \tag{6.42}$$

where M is the number of gaseous species. The conditions (6.42) differ from the conditions for a single isolated drop [155] as the mass and energy fluxes vanish at a finite distance $r = R_{sc}$ from the drop rather than at $r \to \infty$.

The initial conditions at $t = 0$ are written as

$$\begin{gathered} r_s(0) = r_{s0} \\ r < r_{s0}, \quad T(r,0) = T_0 \\ r > r_{s0}, \quad \tilde{T}(r,0) = \tilde{T}_0 \\ r_{s0} < r \le R_{sc}, \quad Y_j(r,0) = Y_{j0} \quad j = 1, 2, \ldots, M \end{gathered} \tag{6.43}$$

Conditions (6.43) make a provision for nonzero initial vapor content Y_{v0} in the gas phase. For numerical solution of the problem, a finite-difference scheme and iterative procedure are used. The details are reported elsewhere [153–155].

Analysis of drop evaporation in dense suspensions shows [153, 154] that the drop vaporization rate and lifetime in suspension may differ considerably compared with those relevant to a single drop placed in an unconfined

[2] η and Φ can be treated as local parameters in nonuniform drop suspensions.

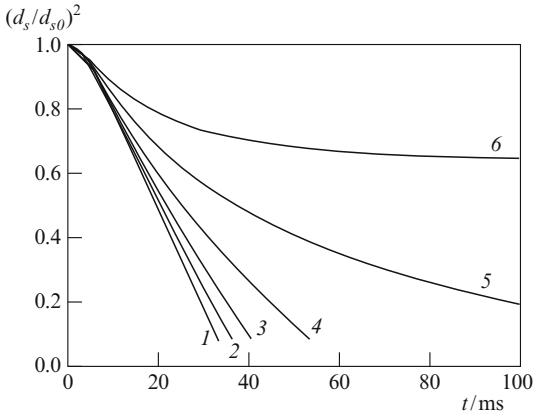

Fig. 6.27. Predicted dynamics of drop surface area for *n*-tetradecane drop suspensions evaporating in air at different fuel–air ratios Φ (distance between drops R_c/r_{s0}) at $d_{s0} = 70\,\mu$m, $T_0 = 293.15\,$K, $\tilde{T} = 573.15\,$K, and $p = 0.1\,$MPa [153, 154]. *1* $\Phi = 9.5$ ($R_c/r_{s0} \to \infty$), *2* $\Phi = 0.6$ (40.0), *3* $\Phi = 1.2$ (31.5), *4* $\Phi = 2.4$ (25), *5* $\Phi = 4.75$ (20), and *6* $\Phi = 9.5$ (15.7)

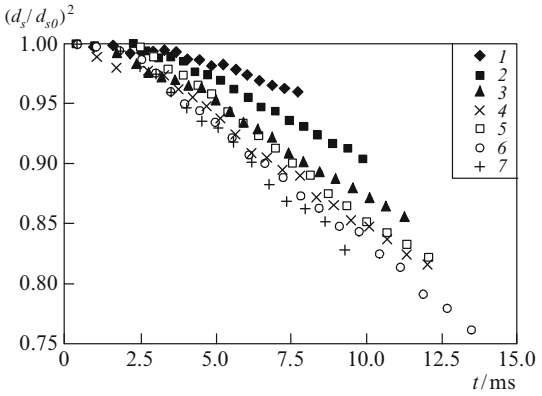

Fig. 6.28. Measured vaporization dynamics of monodisperse ethanol drops in the linear array issued vertically upward along the thermal boundary layer at the vertical heated plate [171]. Points *1*–*7* correspond to different spacings between drops R_c/r_{s0}: *1* 2.6, *2* 5, *3* 7.2, *4* 9.4, *5* 11.5, *6* 13.6, and *7* 15.8

atmosphere. Figure 6.27 shows the predicted drop surface regression curves for *n*-tetradecane drops in suspensions of different densities. Three important findings follow from Fig. 6.27: (1) the inclusion of spray effects results in slower drop vaporization; (2) the quasi-steady drop vaporization law is, in general, not valid; and (3) for each liquid there exists a fuel–air ratio Φ_m (or η_m) such that at $\Phi > \Phi_m$ (or $\eta > \eta_m$), drops evaporate only partly. The first and second findings have been confirmed experimentally. For example, Fig. 6.28 shows the

results of measurements [140] of ethanol drop vaporization dynamics in linear arrays with different spacings between drops. It is seen that a decrease in the drop spacing leads to a decrease in the drop vaporization rate just at the beginning of the process and the dependence of d_s^2/d_{s0}^2 on time deviates more greatly from the straight line. Note that the screening effect of neighboring drops in the linear array is considerably smaller than that in the schematics of Fig. 6.26b and c.

It is natural to anticipate that similar effects are inherent in the micromist behind a shattered parent drop. Unfortunately, this stage of the process has not been sufficiently well studied to allow reliable relationships for calculation of its rate to be proposed.

6.3.6 Kinetic Mechanisms of Drop Ignition and Combustion

To study gas-phase autoignition behind a shock wave, detailed reaction mechanisms are widely used. As for the fuel drops and sprays, detailed reaction mechanisms have not been used so far except in several recent publications, e.g., [156]. This is caused by the fact that the kinetic mechanisms of high hydrocarbons are very complex and, in addition to chemical complications, drop combustion is accompanied by complex physical processes. Therefore, for modeling n-alkane drop ignition and combustion, reduced or overall reaction mechanisms are usually applied [154, 157, 158]. A reaction mechanism in [154,157,158] contains ten reactions with ten species (fuel, O_2, N_2, CO, CO_2, H_2, H_2O, NO, soot, and generalized radical). The mechanism was validated on the problems of premixed laminar flame propagation and a laminar counterflow diffusion flame, as well as fuel drop autoignition and combustion [154, 157–161]. It was found to be well applicable to the description of high-temperature oxidation of n-alkanes at temperatures exceeding 1,200–1,300 K. At temperatures below 900 K, the kinetics of n-alkane oxidation changes and so-called multistage behavior accelerating the chemical process start to appear. To model multistage autoignition, more complex kinetic mechanisms are required.

There are several publications on detailed and semiempirical reaction mechanisms for heavy hydrocarbons. For example, in [162] oxidation mechanisms of n-heptane and isooctane were suggested. The mechanism [162] is composed of two reaction blocks: a detailed mechanism of oxidation of C_1–C_2 hydrocarbons and an overall mechanism of low-temperature oxidation and decomposition of n-heptane and isooctane. In [163], a kinetic mechanism for low-temperature n-tetradecane oxidation was developed, and is also composed of two reaction blocks. The first block is the detailed reaction mechanism of oxidation of C_1–C_2 hydrocarbons. It includes 119 reversible elementary reactions with 29 species. This block is the same as that used in [162]. The second block is the overall mechanism of low-temperature oxidation and decomposition of $C_{14}H_{30}$. It contains 15 reactions with seven new species.

6.3.7 High-Temperature Drop Ignition

High-temperature autoignition of n-heptane drops was modeled in [154, 157, 158] using the overall kinetic mechanism. For a single drop in microgravity conditions, satisfactory agreement between predicted and measured [164,165] ignition delay times was obtained (Table 6.7). In the calculations, the initial temperature of the drops was 293 K. The ambient air temperature was assumed to be spatially uniform. The size of the computational domain around the drop R_{sc} was sufficiently large compared with the initial drop radius r_{s0}, so the values of all parameters on the external boundary were constant in the course of the calculations.

After a certain time, referred to as the ignition delay time, t_{ign}, at a certain distance from the drop surface, autoignition of fuel vapor was detected in the calculations. The ignition delay time t_{ign} was defined as the time interval for the rate of maximal temperature rise to attain a predefined value of $T'_{max} = 10^6\,\mathrm{K s^{-1}}$. Other reasonable definitions were also used, but they resulted in very similar values of t_{ign}. Figure 6.29 shows predicted dependencies of the

Table 6.7. Comparison of predicted and measured autoignition delay times for isolated n-heptane drops at a pressure of 0.1 MPa under microgravity conditions [154, 158]

Initial drop diameter (μm)	Air temperature (K)	t_{ign} (s)	
		Measured	Calculated
700	1,000	0.30 [164]	0.19
1,000	960	0.58 [165]	0.48

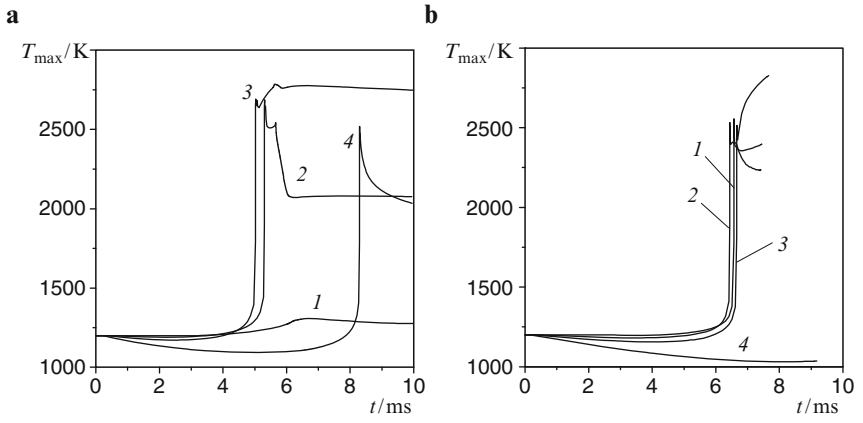

Fig. 6.29. Predicted dependencies of maximal temperature in the vicinity of n-heptane **a** and n-tetradecane **b** drops at autoignition conditions. Initial data: $d_{s0} = 50\,\mu\mathrm{m}$, $T_0 = 293.15\,\mathrm{K}$, $\tilde{T} = 1,200\,\mathrm{K}$, and $p = 0.1\,\mathrm{MPa}$. *1* $\Phi = 0$ (single drop), *2* $\Phi = 0.5$, *3* $\Phi = 1.0$, and *4* $\Phi = 2.0$

maximal temperature in the vicinity of an n-heptane (Fig. 6.29a) and an n-tetradecane (Fig. 6.29b) drop at $T_0 = 293.15\,\mathrm{K}$, $\tilde{T} = 1,200\,\mathrm{K}$, and $p = 0.1\,\mathrm{MPa}$. A single n-heptane drop fails to ignite at these conditions, while a single n-tetradecane drop ignites (see curves 1). Curves 2–4 correspond to $\Phi = 0.5$, 1.0, and 2.0 and demonstrate the spray effect on autoignition of drop suspensions of these two fuels. For n-heptane drop suspensions, the shortest ignition delay is attained in the stoichiometric mixture (curve 3 in Fig. 6.29a). Fuel-rich drop suspensions of n-heptane ($\Phi = 2.0$) ignite only after complete drop vaporization. For n-tetradecane drop suspensions, the shortest ignition delays are attained in fuel-lean suspensions (curve 2 in Fig. 6.29b, $\Phi = 0.5$). Fuel-rich n-tetradecane suspensions ($\Phi = 2.0$) fail to ignite, at least in 10 ms. Thus, autoignition of drop suspensions is very sensitive to the suspension density and liquid fuel properties.

Following [157, 158], let us introduce the concept of normalized mass content of the jth species, $I_j(t)$, as the ratio of the total mass of this component in the gas phase at time t to the initial drop mass, $m_0 = (4/3)\,\pi r_{\mathrm{s}0}^3 \rho_{\mathrm{l}}$, i.e.,

$$I_j(t) = m_0^{-1} \int_{r(t)}^{R_{\mathrm{sc}}} 4\pi\xi^2 Y_j(\xi, t)\mathrm{d}\xi.$$

As before, index v will be used for fuel vapor. It is instructive to distinguish between fuel which is initially in the liquid phase and fuel which is initially in the vapor phase. The former and the latter will be marked by indices vd and vg, respectively. Thus,

$$I_{\mathrm{v}}(t) = I_{\mathrm{vd}}(t) + I_{\mathrm{vg}}(t).$$

The first term on the right-hand side of this equation relates to the part of I_{v} corresponding to the fuel which is initially contained in the liquid drop. The second term relates to the part of I_{v} which is initially contained in the vapor phase, e.g., owing to preliminary partial drop vaporization. By definition, the prevaporization degree is equal to $I_{\mathrm{vg}}(0)$. The normalized fuel content varies with time because of two processes: drop vaporization and chemical reaction. When a liquid drop evaporates completely but the fuel does not react chemically, the value of I_{vd} tends to unity. If there are gas-phase reactions of fuel oxidation, then fuel vapor is depleted in the course of the reactions and the value of I_{v} decreases (in the case of a single drop, I_{v} tends to zero).

Figure 6.30a presents an example of predicted time histories of a squared drop diameter $d^2(t)$ at autoignition of a single n-hexane drop. At completion of the ignition delay time ($t_{\mathrm{ign}} = 160\,\mu\mathrm{s}$), the $d^2(t)$ curve exhibits a kink and the dependence becomes linear. The drop lifetime is about $250\,\mu\mathrm{s}$. Figure 6.30b shows the corresponding dependencies $I_{\mathrm{j}}(t)$ for different species: fuel (C_6H_{14}), CO, H_2, CO_2, and H_2O at $I_{\mathrm{vg}}(0) = 0$. It is seen that during the ignition delay the fuel vapor accumulates in the gas phase (curve C_6H_{14}). After autoignition, some of fuel vapor burns out rapidly and then the rate of fuel vapor consumption stabilizes and becomes nearly constant. This stage

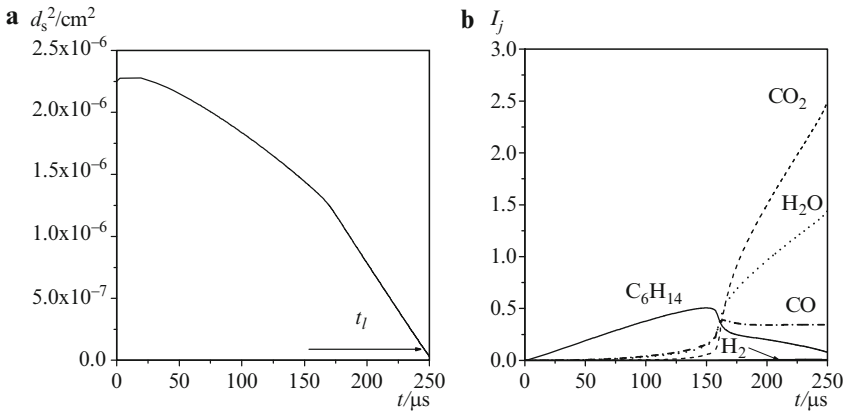

Fig. 6.30. Predicted time histories of a squared *n*-hexane drop diameter **a** and normalized mass contents of various combustion products in the gas phase **b**; t_l is the drop lifetime; $d_{s0} = 15\,\mu m$, $\tilde{T} = 1,500\,K$, and $p = 3\,MPa$ [157, 158]

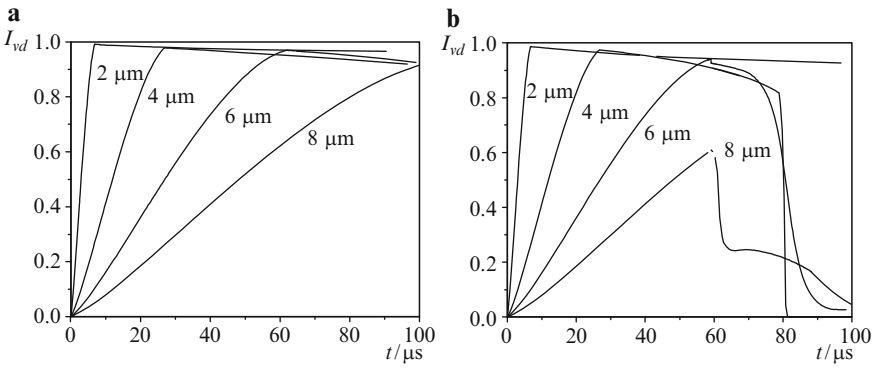

Fig. 6.31. Predicted time histories of normalized mass content of fuel I_{fd} for fine *n*-heptane drops of initial diameter 2, 4, 6, and 8 μm at $\tilde{T} = 1,500\,K$ and $p = 3\,MPa$: **a** $I_{fg} = 0$ and **b** 0.25 [157, 158]

corresponds to the diffusion-controlled combustion of the drop. CO_2 and H_2O accumulate with time, while the yields of other products (CO and H_2) are insignificant.

Figure 6.31a shows the predicted time history of the normalized mass content of fuel vapor I_{vd} (at $I_{vg} = 0$) in a stoichiometric suspension of fine *n*-heptane drops of initial diameter 2, 4, 6, and 8 μm in air. Such drops exhibit very short velocity relaxation times behind incident shock waves. In view of this, their ignition can be approximately treated as ignition in a quiescent oxidizing atmosphere. Drops of an initial diameter 2 μm first evaporate very fast ($t_l = 5.8\,\mu s$) and then the normalized fuel vapor content decreases very

slowly over 100 μs, i.e., the oxidation reaction is slow. The analysis shows that owing to fast drop evaporation, the temperature in the elementary sphere of radius R_{sc} around the initial drop decreases by about 300 K, i.e., to a value less than 1,225 K. At such a low temperature, the oxidation reaction takes considerably longer than 100 μs. It is seen from Fig. 6.31a that all the specific features found for 2-μm drops are valid for drops 4, 6, and 8 μm in diameter.

The drop lifetime decreases considerably if the gas phase initially contains fuel vapor, e.g., owing to partial drop prevaporization. In this case, $I_{vg} \neq 0$. Figure 6.31b shows predicted time histories of I_{vd} for stoichiometric suspensions of fine *n*-heptane drops of initial diameter 2, 4, 6, and 8 μm in air at $I_{vg}(0) = 0.25$. Such a value of $I_{vg}(0)$ corresponds to the case when 25% of the total fuel mass is initially in the vapor phase.

When comparing Fig. 6.31a and b, one notices that at $I_{vg} \neq 0$, the $I_{vd}(t)$ curves exhibit a new feature: starting from a certain time instant, the value of the normalized mass content of fuel decreases drastically, i.e., autoignition occurs. For example, at $I_{vg}(0) = 0.25$ (Fig. 6.31b), the drops of diameter 6 μm are ignited at $t = 60$ μs owing to fast oxidation of prevaporized fuel. After the autoignition event, the rate of fuel burnout slows and a transition to diffusion-controlled drop combustion is observed. At $t = 100$ μs, there is only 2.5% unburned fuel. Autoignition of prevaporized fuel in the stoichiometric suspension with drops 8 μm in diameter occurs approximately at the same time: in 60 μs. However, in 100 μs, nearly 4.6% of the fuel remains unburned. Autoignition of drops 4 μm in diameter occurs with a delay time of about 80 μs (the strong influence of initial cooling caused by fast vaporization appears); however, toward 100 μs, the fuel is completely burned. Drops 2 μm in diameter are ignited with an ignition delay exceeding 100 μs. The dynamics of suspension ignition change with increasing prevaporization degree. At $I_{vg}(0) = 0.5$, the drops 2, 4, and 6 μm in diameter burn out completely in 100 μs, while the $8-$μm drops burn out only partly: about 2.5% of the fuel remains unburned. Even at $I_{vg}(0) = 0.75$, 8-μm drops burn out incompletely in 100 μs (about 1.5% of the fuel remain unburned). It is interesting that larger drops (6 and 8 μm) exhibit combustion modes with several autoignition events [157, 158].

6.3.8 Low-Temperature Drop Ignition

In the calculations of low-temperature drop autoignition, the semiempirical kinetic mechanism of *n*-tetradecane was used [163]. The calculations were performed for the stoichiometric drop suspension, i.e., the radius of the computational domain R_{sc} around a drop was equal to the radius of the stoichiometric elementary sphere.

Figure 6.32 shows examples of predicted time histories of squared drop diameter $(d_s/d_{s0})^2$, maximal gas temperature $\tilde{T}_{max}$, normalized mass content of hydroxyl, and normalized mass contents of alkylhydroperoxide and hydrogen peroxide at autoignition of an *n*-tetradecane drop with $d_{s0} = 20$ μm at $p = 2.5$ MPa and $\tilde{T} = 650$ K.

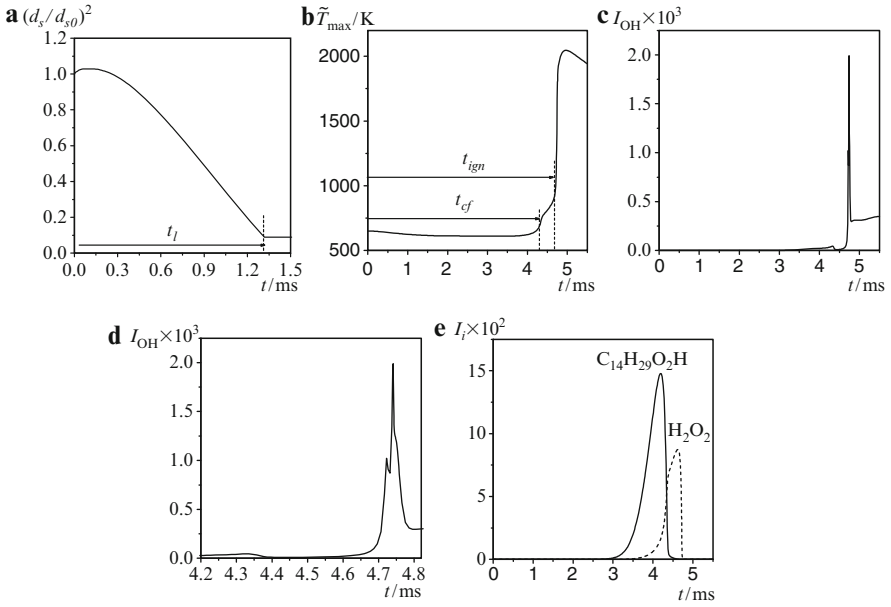

Fig. 6.32. Predicted time histories of the squared drop diameter $(d_s/d_{s0})^2$ **a**, maximum gas temperature $\tilde{T}_{max}$ **b**, normalized mass content of OH **c**, **d**, and normalized mass contents of $C_{14}H_{29}O_2H$ and H_2O_2 **e** at autoignition of an n-tetradecane drop with $d_{s0} = 20\,\mu m$ ($p = 2.5\,MPa$ and $\tilde{T} = 650\,K$) [163]

The drop lifetime t_l was determined as the time for the drop mass to decrease by a factor of 30. The arrow in Fig. 6.32a indicates the calculated drop lifetime with $d_{s0} = 20\,\mu m$ ($t_l \approx 1.32\,ms$). It is seen from Fig. 6.32b that at the beginning of the process the maximal gas temperature around the drop (at the external boundary of the computational domain) decreases owing to drop vaporization and heating. Until a time of 1.7 ms, the value of $\tilde{T}_{max}$ decreases by about 40 K and further temperature decrease stops owing to the drop vanishing and a growing heat release caused by chemical reactions. Autoignition occurs in two stages. At first, a cool flame comes into effect after a delay time of $t_{cf} = 4.33\,ms$, which is accompanied by a temperature rise of about 200 K. Then a hot explosion occurs with a total delay time of $t_{ign} = 4.71\,ms$, which is accompanied by a temperature rise to approximately 2,200 K.

Comparing Fig. 6.32a and b one can see that $t_{cf} > t_l$ for the drop with $d_{s0} = 20\,\mu m$. This means that fine drops completely evaporate before the development of the cool flame, and the cool-flame oxidation of fuel vapor proceeds in a relatively large volume. Such conditions are close to the conditions of cool-flame oxidation in a homogeneous mixture, where it was discovered and observed repeatedly. Further analysis of Fig. 6.32b and c or d (Fig. 6.32d is a zoomed view of Fig. 6.32c) indicates that the temperature rise in the

cool flame coincides with the hydroxyl concentration buildup. On the other hand, when comparing Fig. 6.32c or d with e, one notices that the buildup of hydroxyl concentration coincides with decomposition of alkylhydroperoxide. In homogeneous mixtures, the latter process is responsible for a cool flame appearance. Note that at completion of the total ignition delay in Fig. 6.32d ($t_{\rm ign} = 4.71$ ms), one can clearly see a local maximum in hydroxyl concentration, coinciding with hydrogen peroxide decomposition (owing to the reaction $H_2O_2 = OH + OH$ in the block of the detailed reaction mechanism of oxidation of C_1–C_2 hydrocarbons). In homogeneous mixtures, this process is responsible for a blue flame appearance. The blue flame appearance is not evident on the temperature curve of Fig. 6.32b because it virtually coincides with a hot explosion.

Figure 6.33 presents the predicted dependencies of the total ignition delay $t_{\rm ign}$ and cool flame ignition delay $t_{\rm cf}$ on the initial drop diameter $d_{\rm s0}$ at $p = 2.5$ MPa and $\tilde{T} = 650$ K. In addition to curves $t_{\rm ign}(d_{\rm s0})$ and $t_{\rm cf}\,(d_{\rm s0})$, Fig. 6.33 shows the predicted dependence of the drop lifetime on the initial drop diameter $t_{\rm l}(d_{\rm s0})$. As shown, $t_{\rm cf} > t_{\rm l}$ only for drops with $d_{\rm s0} < 35\,\mu$m. At $d_{\rm s0} < 35\,\mu$m, the total ignition delay is a weak function of drop diameter and the cool-flame ignition delay $t_{\rm cf}$ is a main contributor to $t_{\rm ign}$. Note that the use of the temperature curve for determining $t_{\rm cf}$ becomes complicated for drops with $d_{\rm s0} > 30\,\mu$m because the temperature curve starts to resemble the curve of single-stage high-temperature oxidation.

Consider now the case when $t_{\rm cf} > t_{\rm l}$ in the example of autoignition of an n-tetradecane drop $d_{s0} = 40\,\mu$m in diameter at $p = 2.5$ MPa and

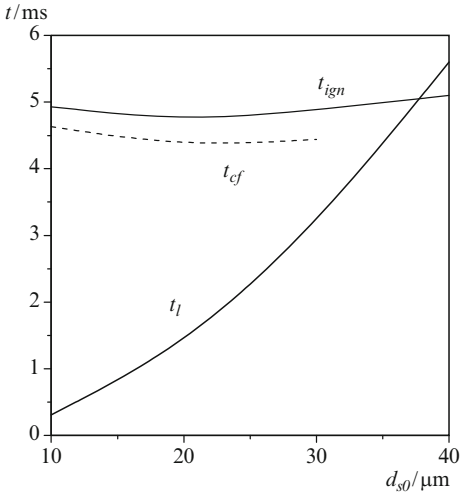

Fig. 6.33. Predicted dependencies of the total ignition delay $t_{\rm ign}$, ignition delay of the cool flame $t_{\rm cf}$, and drop lifetime $t_{\rm l}$ on initial drop diameter $d_{\rm s0}$ at $p_0 = 2.5$ MPa and $T_{\rm g0} = 650$ K [163]

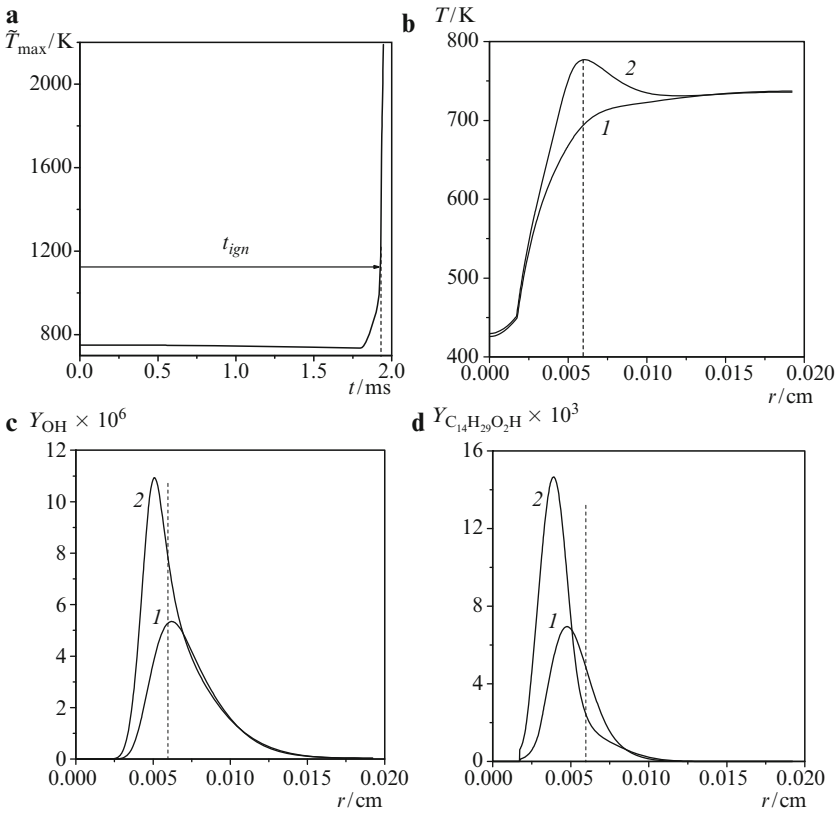

Fig. 6.34. Predicted time histories of maximum gas temperature $\tilde{T}_{\max}$ **a**, instantaneous radial distributions of temperature **b**, and mass fractions of hydroxyl Y_{OH} **c** and alkylhydroperoxide $Y_{\mathrm{C_{14}H_{29}O_2H}}$ **d** at $t = 1.75$ (curves *1*) and 1.85 ms (curves *2*) at *n*-tetradecane drop autoignition ($d_{s0} = 40\,\mu$m, $p_0 = 2.5$ MPa and $T_{g0} = 750$ K) [163]

$\tilde{T} = 750$ K. It follows from Fig. 6.34a that the total ignition delay in this case is $t_{\mathrm{ign}} = 1.94$ ms (shown by an arrow). At the instant of autoignition the surface area of the drop decreased by about 20% and nearly 30% of the drop mass has evaporated. The cool flame is not evident at the temperature curve $\tilde{T}_{\max}(t)$. It cannot be distinguished in the time histories of normalized mass contents of hydroxyl and alkylhydroperoxide. This is caused by a significant nonuniformity of the temperature and concentration fields around the drop. Nevertheless, careful analysis of these fields reveals that all features relevant to cool flame development in homogeneous mixtures are exhibited locally.

Figure 6.34b–d shows the instantaneous radial distributions of temperature, and mass fractions of hydroxyl Y_{OH} and alkylhydroperoxide $Y_{\mathrm{C_{14}H_{29}O_2H}}$ at time instants $t = 1.75$ (curves 1) and 1.85 ms (curves 2). It follows from

Fig. 6.34b that before ignition, at a time instant between $t = 1.75$ and 1.85 ms, a localized temperature rise occurs at a distance $r = 0.006$ cm from the drop center (denoted by the dashed line). This temperature rise corresponds to a runaway reaction owing to a localized increase in the hydroxyl mass fraction at the same distance from the drop center (Fig. 6.34c), which, in turn, is caused by a localized decomposition of alkylhydroperoxide (Fig. 6.34d). A special computational experiment indicates that, when starting from $t = 1.75$ ms, the active decomposition products of alkylperoxide in the reaction $C_{14}H_{29}O + OH$ are replaced by considerably less reactive initial species $C_{14}H_{30} + O_2$, the reaction slows down sharply instead of being a runaway reaction, and the localized temperature rise is replaced by mixture cooling caused by drop vaporization. Thus, the reaction proceeds in a way similar to that in a homogeneous mixture, but locally. This is the reason why the cool-flame stage cannot be distinguished in the time histories of characteristic parameters such as maximum temperature of normalized mass contents of the various species.

6.3.9 Ignition of Disintegrating Drops

The characteristic breakup time of relatively large liquid drops behind a strong shock wave relevant to spray detonations is usually very small compared with the ignition delay. Whatever the prevailing mechanism of liquid drop atomization behind a shock wave, ignition occurs in the boundary layer surrounding the wake of the drop, which, according to experimental observations, is nearly conical in shape. Thus, both numerical simulations and evidence derived from shock-tube experiments suggest three major stages of the ignition and combustion process: (1) drop breakup, (2) ignition of the mixture at the wake periphery, and (3) diffusion-controlled fuel burning in the wake.

The rate control can be determined from simple considerations. Breakup of drops 100 μm in diameter is completed within less than 10 μs after the shock wave spreading at a velocity of $1,600\,\mathrm{m\,s^{-1}}$ at atmospheric pressure: the total breakup time of smaller drops is even shorter. However, the pressure measured behind detonation waves in sprays of low-volatility fuels shows that the so-called von Neumann spike, where the contribution of the reaction heat to flow characteristics is insignificant, lasts no less than 100 μs [166]. Hence, the heat release rate behind fuel–air detonation waves in sprays with physically attainable drop sizes is controlled by the other two stages.

Mixture autoignition is reasonably assumed to occur at the periphery of the cloud arising in the course of drop breakup because the gas in the wake is colder than the free-stream gas and fuel–oxidizer mixture. Therefore, the capability for autoignition most probably exists at the boundary between the free-stream and stripped droplet material. Rough estimates [167] show that the amount of fuel mixed with air in this boundary layer is small: no more than 16% over the total breakup time for 100-μm particles.

Autoignition in the boundary layer is controlled by chemical kinetics and may occur either during or after breakup subsequent to an induction period,

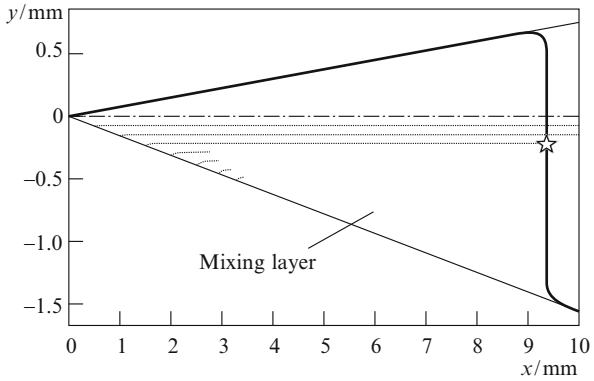

Fig. 6.35. Predicted autoignition location in the planar, isothermal, turbulent mixing layer of a fine fuel spray with air [168, 169]. *Thin solid lines* show the boundaries of the mixing layer. The *thick solid curve* denotes the locus of the limiting normalized preexplosion heating $R\tilde{T}/E = 0.05$. *Dashed curves* show the predicted mean trajectories of notional particles in the mixing layer. The *star* denotes the self-ignition location, where the notional particle residence time t is equal to the ignition delay t_{ign}

which can be calculated approximately using the free-stream temperature and pressure. For example, Fig. 6.35 shows the predicted autoignition location (denoted by a star) in the planar, isothermal, turbulent mixing layer of a fine fuel spray in air [168, 169]. In the calculations, the following values of the governing parameters were used: air density $30\,\text{kg}\,\text{m}^{-3}$, fuel density $850\,\text{kg}\,\text{m}^{-3}$, activation energy $8,800\,\text{cal}\,\text{mol}^{-1}$, temperature 900 K, pressure 4 MPa, and fuel spray velocity at the nozzle exit $100\,\text{m}\,\text{s}^{-1}$. Ignition occurs at the periphery of the mixing layer at a distance of about 9 mm from the layer origin and 1.2 mm from the outer (air) boundary of the layer. Although the study in [168, 169] dealt with diesel spray, the results obtained can be readily applied to the autoignition phenomenon in the conelike mixing layer attached to shattered drops behind a shock wave.

6.4 Concluding Remarks

Current understanding of the physical and chemical processes accompanying solid and liquid particle ignition behind shock waves is based on the simplified treatment of various interactions between particles and the shock-induced flow. Analysis of these interactions indicates that the phenomena encountered are very complex and interrelated. Even simple particle/drop ignition models exhibit numerous scenarios of particle/drop temperature evolution behind incident and reflected shock waves. For liquid drops, the phenomena of drop breakup combined with the formation of a mixing layer of micromist droplets

with air, micromist vaporization, ignition, and combustion exhibit many features that have not yet been studied. The essential role is played by various local rather than averaged processes, implying that a multidimensional treatment of the problem is inevitably required.

References

1. Beckstead, M.W.: A summary of aluminum combustion. RTO-EN 023 Paper presented at the RTO/VKI special course on internal aerodynamics in solid rocket propulsion, Rhode-Saint-Genese, 27–31 May 2002
2. Law, C.K.: Recent advances in droplet vaporization and combustion. Prog. Energy Combust. Sci. **8**, 171–201 (1982)
3. Sirignano, W.A.: Fuel droplet vaporization and spray combustion theory. Prog. Energy Combust. Sci. **9**, 291–322 (1983)
4. Bachalo, W.D.: Injection, dispersion, and combustion of liquid fuels. In: Proceedings 25th Symposium (International) on Combustion, pp. 333–344. The Combustion Institute, Pittsburgh (1994)
5. Mashayek, F., Pandya, R.V.R.: Analytical description of particle laden flows. Prog. Energy Combust. Sci. **29**, 329–378 (2003)
6. Brzustowski, T.A., Glassman, I.: Vapor phase. diffusion flames. In: Wolfhard, H.G., Glassman, I., Green, L. (eds.) Heterogeneous Combustion, pp. 75–115. Academic, New York (1964)
7. Klyachko, L.A.: Ignition of particle group with heterogeneous reaction. Teploenergetika **8**, 65 (1966)
8. Khaikin, B.I., Bloshenko, V.N., Merzhanov, A.G.: On the ignition of metal particles. Combust. Explos. Shock Waves **6**, 412–422 (1970)
9. Aldushin, A.P., Bloshenko, V.N., Seplyarskii, B.S.: Ignition of metal particles with a logarithmic oxidation law. Combust. Explos. Shock Waves **9**, 423–428 (1973)
10. Law, C.K.: A simplified theoretical model for the vapor-phase combustion of metal particles. Combust. Sci. Technol. **7**, 197–212 (1973)
11. Varshavskii, G.A.: Drop combustion. Trans. NII-1 **6**, 30 (1945)
12. Godsave, G.A.E.: Studies of the combustion of drops in a fuel spray – the burning of single drops of fuel. In: Proceedings 4th Symposium (International) on Combustion, pp. 818–830. Williams & Wilkins, Baltimore (1953)
13. Spalding, D.B.: The combustion of liquid fuels. In: Proceedings 4th Symposium (International) on Combustion, pp. 847–864. Williams & Wilkins, Baltimore (1953)
14. Goldsmith, M., Penner, S.S.: On the burning of single drops of fuel in an oxidizing atmosphere. Jet Propuls. **24**(4), 245 (1954)
15. Frank-Kamenetskii, D.A.: Diffusion and Heat Transfer in Chemical Kinetics. Nauka, Moscow (1961)
16. Twardus, E.M., Brzustowski, T.A.: The interaction between two burning fuel droplets. Arch. Processow Spal. **8**, 347–358 (1977)
17. Dwyer, H.A., Nirschl, H., Kerschl, P., Denk, V.: Heat, mass, and momentum transfer about arbitrary groups of particles. In: Proceedings 25th Symposium (International) on Combustion, pp. 389–396. The Combustion Institute, Pittsburgh (1994)

18. Marberry, M., Ray, A.K., Leung, K.: Effect of multiple particle interactions on burning droplets. Combust. Flame **57**, 237 (1984)
19. Cuadros, J., Linares, J., Sivasankaran, K., Seetharamu, K.N., Natarajan, R.: Numerical investigation of the interference effects between two burning fuel spheres. Int. J. Heat Mass Transfer **39**, 3949–3957 (1996)
20. Chiu, H.H., Liu, T.M.: Group combustion of liquid droplets. Combust. Sci. Technol. **17**, 127–142 (1977)
21. Correa, S.M., Sichel, M.: The group combustion of a spherical cloud of monodisperse fuel droplets. In: Proceedings 19th Symposium (International) on Combustion, pp. 856–863. The Combustion Institute, Pittsburgh (1983)
22. Nigmatulin, R.I.: Dynamics of Multiphase Media, vol. 1. Nauka, Moscow (1987)
23. Borisov, A.A., Kogarko, S.M., Kozenko, V.P.: Detonation limits of methane–oxygen mixtures diluted with argon or helium. Combust. Explos. Shock Waves **2**, 55 (1967)
24. Nettleton, M.A., Stirling, R.: The ignition of clouds of particles in shock-heated oxygen. Proc. R. Soc. Lond. A **300**, 62–77 (1967)
25. Macek, A., Semple, J.M.: Combustion of boron particles at atmospheric pressure. Combust. Sci. Technol. **1**(3), 181–191 (1969)
26. Ryzhik, A.B., Yurmanov, Yu.A., Limonov, B.S., et al.: Ignition of dispersed magnesium behind shock waves. Phys. Aerodispersed Syst. **9**, 115 (1973)
27. Fox, T.W., Rackett, C.W., Nicholls, J.A.: Shock wave ignition of magnesium powders. In: Proceedings 11th International Shock Tubes and Waves Symposium, pp. 262–268, Seattle (1978)
28. Cohen, A., Decker, L.: Shock tube ignition of nitrocellulose and nitramines. In: Proceedings 10th JANAF Meeting, CPIA Publ., Laurel, MD (1978)
29. Cohen, A., Decker, L.: Shock tube ignition of nitrocellulose. In: Proceedings 12th Symposium (International) Shock Tubes, Jerusalem, 16–19, pp. 514–520 July 1979
30. Kauffman, C.W., Wolanski, P., Ural, E., et al.: Shock wave initiated combustion of grain dust. In: Proceedings Symposium (International) on Grain Dust, pp. 164–190, Manhattan (1979)
31. Breipohl, G., Lester, T.W., Merklin, J.F.: Shock tube studies of the mechanism of grain dust ignition. In: Proceedings Symposium (International) on Grain Dust, pp. 191–211, Manhattan (1979)
32. Seeker, W.R., Lester, T.W., Merklin, J.F.: Shock tube. techniques in the study of pulverized coal ignition and burnout. Rev. Sci. Instrum. **51**(11), 1523–1531 (1980)
33. Ural, E.A., Sichel, M., Kauffman, C.W.: Shock wave ignition of pulverized coal. In: Treanor, C.E., Hall, J.G. (eds.) Shock Tubes and Waves, pp. 809–817. State University of New York Press, Albany (1981)
34. Wolanski, P.: Problems of dust explosions. In: Proceedings 1st Specialists Meeting (International) of the Combustion Institute, pp. 497–502, Bordeaux (1981)
35. Wolanski, P.: Fundamental problems of dust explosions. In: Lee, J.H.S., Guirao C.M. (eds.) Fuel–Air Explosions, pp. 349–373. University of Waterloo Press, Waterloo (1982)
36. Borisov, A.A., Gelfand, B.E., Tsyganov, S.A., et al.: Ignition of dusts behind shock waves. Chem. Phys. Rep. **2**(8), 40 (1983)
37. Borisov, A.A., Gelfand, B.E., Timofeev, E.I., et al.: Ignition of dust suspensions behind shock waves. In: Bowen, J.R., Manson, N., Oppenheim, A.K.,

Soloukhin, R.I. (eds.) Dynamics of Shock Waves, Explosions, and Detonations. Progress in Astronautics and Aeronautics, vol. 94, pp. 332–339. American Institute of Aeronautics and Astronautics, New York (1984)
38. Sichel, M., Baek, S.W., Kauffman, C.W., et al.: The shock wave ignition of dusts. AIAA J. **23**(9), 1374–1380 (1985)
39. Boiko, V.M., Lotov, V.V., Papyrin, S.V.: Ignition of metal powders in reflected shock waves. Arch. Combust. **8**(2), 101–114 (1988)
40. Li, S.C., Williams, F.A., Takahashi, F.: In: Proceedings 22nd Symposium (International) on Combustion, pp. 1951–1960. The Combustion Institute, Pittsburgh (1988)
41. Wolanski, P.: Deflagration and detonation combustion of dust mixtures. In: Kuhl, A. L., Leyer, J.-C., Borisov, A.A., Sirignano, W.A. (eds.) Dynamics of Deflagrations and Reactive Systems: Heterogeneous Combustion. Progress in Astronautics and Aeronautics, vol. 132, pp. 3–31. American Institute of Aeronautics and Astronautics, New York (1991)
42. Boiko, V.M., Papyrin, S.V., Poplavskii, S.V.: Mechanism of dust ignition in incident shock waves. Combust. Explos. Shock Waves **29**(3), 389–394 (1993)
43. Boiko, V.M., Papyrin, S.V., Poplavskii, S.V.: Ignition mechanism of coal suspension in shock waves. In: Kuhl, A.L., Leyer, J.-C., Borisov, A.A., Sirignano, W.A. (eds.) Dynamic Aspects of Explosion Phenomena. Progress in Astronautics and Aeronautics, vol. 154, pp. 278–290. American Institute of Aeronautics and Astronautics, New York (1993)
44. Roberts, T.A., Burton, R.L., Krier, H.: Ignition and combustion of aluminum/magnesium alloy particles in O_2 at high pressures. Combust. Flame **92**(1–2), 125–143 (1993)
45. Geng, J.H., van de Ven, A., Zhang, F., et al.: A new setup to measure ignition delay of a dust suspension behind an incident shock wave. In: Xufan, D., Wolanski, P. (eds.) Proceedings 6th Colloquium (International) on Dust Explosions, pp. 309–314. Northeastern University Press, Shenyang (1994)
46. Spalding, M. J., Krier, H., Burton, R. L.: Boron suboxides measured during ignition and combustion of boron in shocked $Ar/F/O_2$ and $Ar/N_2/O_2$ mixtures. Combust. Flame **120**, 200–210 (2000)
47. Servaites, J., Krier, H., Melcher, J. C., et al.: Ignition and combustion of aluminum particles in shocked $H_2O/O_2/Ar$ and $CO_2/O_2/Ar$ mixtures. Combust. Flame **125**, 1040–1054 (2001)
48. Dreizin, E.L., Trunov, M.A., Suslov, A.V.: General trends in metal particles heterogeneous combustion. Combust. Sci. Technol. **90**, 79–99 (1993)
49. Dreizin, E.L., Trunov, M.A.: Surface phenomena in aluminum combustion. Combust. Flame **101**, 378–382 (1995)
50. Temos, J., Pratt, H.R.C., Stevens, G.W., Dreizin, E.L.: Experimental study of stages in aluminum particle combustion in air. Combust. Flame **105**(4), 541–556 (1996)
51. Molodetsky, I.E., Vicenzi, E.P., Dreizin, E.L., Law, C.K.: Phases of titanium combustion in air. Combust. Flame **112**(4), 522–532 (1998)
52. Dreizin, E.L.: Experimental study of aluminum particle flame evolution in normal and micro-gravity – progress in astronautics and aeronautics. Combust. Flame **116**(3), 323–333 (1999)
53. Dreizin, E.L., Berman, C.H., Vicenzi, E.P.: Condensed-phase modifications in magnesium particle combustion in air. Combust. Flame **122**(1), 30–42 (2000)

54. Trunov, A., Schoenitz, M., Zhu, X., et al.: Effect of polymorphic phase transformations in Al_2O_3 film on oxidation kinetics of aluminium powders. Combust. Flame **140**, 310–318 (2005)
55. Takeno, T., Yuasa, S.: Ignition of magnesium and magnesium-aluminum alloy by impinging hot-air stream. Combust. Sci. Technol. **21**, 109–121 (1980)
56. Fassel, W.M., Papp, C.A., Hildenbrand, D.L., Sernka, R.P.: The experimental nature of the combustion of metal powders. In: Summerfield, M. (ed.) Solid Propellant Rocket Research, pp. 259–270. Academic, New York (1960)
57. Gusachenko, E.I., Stesik, L.N., Fursov, V.P., et al.: Combust. Explosion Shock Waves **10**, 548 (1974)
58. Shevtsov, V.I., Fursov, V.P., Stesik, L.N.: Combust. Explos. Shock Waves **12**, 859 (1976)
59. Cassel, H.V., Liebman, I.: The cooperative mechanism in the ignition of dust dispersions. Combust. Flame **3**(4), 467–472 (1959)
60. Cassel, H.V., Liebman, I.: Combustion of magnesium particles, II. Ignition temperatures and thermal conductivities of ambient atmospheres. Combust. Flame **7**(1), 79–81 (1963)
61. Lermant, J.C., Yip, S.: A generalized Semenov model for thermal ignition in nonuniform temperature systems. Combust. Flame **7**(1), 21–30 (1963)
62. Gurevich, M.A., Stepanov, A.M.: Metal particle ignition. Combust. Explos. Shock Waves **3**, 334–342 (1968)
63. Gurevich, M.A., Stepanov, A.M.: The limiting conditions of metal particle ignition. Combust. Explos. Shock Waves **4**, 189–185 (1970)
64. Khaikin, B.I., Bloshenko, V.I., Merzhanov, A.G.: On the ignition of metal particles. Combust. Explos. Shock Waves **4**, 474–488 (1970)
65. Ezhovsky, G.K., Mochalova, A.S., Ozerov, E.S., et al.: Ignition and combustion of magnesium particle. In: Combustion and Explosion, pp. 234–240. Nedra, Moscow (1972)
66. Ezhovsky, G.K., Ozerov, E.S.: Ignition of powder-like magnesium. Combust. Explos. Shock Waves **6**, 845–851 (1974)
67. Gremyachkin, V.M., Istratov, O.I.: Combust. Explos. Shock Waves **11**, 366 (1974)
68. Bloshenko, V.I., Merzhanov, A.G., Khaikin, B.I.: On the question of determining the kinetic parameters of high-temperature oxidation of magnesium. Combust. Explos. Shock Waves **5**, 682–688 (1976)
69. Derevyaga, M.V., Stesik, L.N., Fedorin, N.A.: Experimental investigation of critical conditions for magnesium ignition. Combust. Explos. Shock Waves **6**, 44–49 (1978)
70. King, M.K.: Modeling of single-particle aluminum combustion in O_2–N_2 atmospheres. In: Proceedings 17th Symposium (International) on Combustion, pp. 1317–1328. The Combustion Institute, Pittsburgh (1979)
71. Fursov, V.I., Shevtsov, V.I., Gusachenko, E.I., et al.: The role of the process of evaporation of high-volatile metals in the mechanism of their high-temperature oxidation and ignition. Combust. Explos. Shock Waves **3**, 3–12 (1980)
72. Medvedev, A.E., Fedorov, A.V., Fomin, V.M.: Mathematical modeling of metal particle ignition in the high-temperature flow behind a shock. Combust. Explos. Shock Waves **18**(3), 261–265 (1982)
73. Medvedev, A.E., Fedorov, A.V., Fomin, V.M., et al.: Mathematical modeling of ignition process of aerodispersed systems. In: Proceedings 3rd International School of Industrial Dust Explosions, pp. 65–79, Turava (1982)

74. Boiko, V.M., Fedorov, A.V., Fomin, V.M., et al.: Ignition of small solid particles behind shock waves. In: Bowen, J.R., Manson, N., Oppenheim, A.K., Soloukhin, R.I. (eds.) Shock Waves, Explosions, and Detonations. Progress in Astronautics and Aeronautics, vol. 87, pp. 71–87. American Institute of Aeronautics and Astronautics, New York (1983)
75. Kazakov, Yu.V., Medvedev, A.E., Fedorov, A.V., et al.: Mathematical modelling of ignition in dusty gases. Arch. Combust. **7**(1–2), 7–17 (1987)
76. Fedorov, A.V., Tetenov, E.V., Veyssiere, B.: Ignition of a suspension of metal particles with an actual explosion. I. Statement of the problem and solution in a self-modeling approximation. Combust. Explos. Shock Waves **27**(5), 527–532 (1991)
77. Petukhova, E.V., Fedorov, A.V.: Ignition of magnesium particles near the end of a shock tube. Combust. Explos. Shock Waves **27**(6), 778–780 (1991)
78. Fedorov, A.V.: Physical and Mathematical Modeling of Ignition of Fine Magnesium Particles. Preprint no. 12–94, pp. 1–30. Institute of Theoretical and Applied Mechanics of the Siberian Branch of the Russian Academy of Sciences, Novosibirsk (1994)
79. Makino, A.: An approximation explicit expression for the combustion rate of a small carbon particle. Combust. Flame **90**, 143–154 (1992)
80. Zhou, W., Yetter, R.A., et al.: A comprehensive physical and numerical model of boron particle ignition. In: Proceedings 26th Symposium (International) on Combustion, pp. 1909–1918. The Combustion Institute, Pittsburgh (1996)
81. Hayhurst, A.N.: The mass transfer coefficient for oxygen reacting with a carbon particle in a fluidized or packed bed. Combust. Flame **121**(4), 679–688 (2000)
82. Foertsch, D., Schnell, U., Hein, K.R.G.: The mass transfer coefficient for the combustion of pulverized carbon particles. Combust. Flame **126**, 1662–1668 (2001)
83. Tao, H.: Shock wave ignition of aluminum particles. J. Phys. IV **12**(7), 105–112 (2002)
84. Meinkoh, D.: Liquid oxide surface layer in metal combustion. Combust. Theory Modelling **8**, 315–338 (2004)
85. Vilyunov, V.N.: Theory of Ignition of Condensed Substances. Nauka, Novosibirsk (1984)
86. Gosteev, Yu.A., Fedorov, A.V.: Magnesium-particle ignition (distributed model). Combust. Explos. Shock Waves **32**(4), 363–369 (1996)
87. Borovikov, M.B., Goldschleger, U.I.: Critical phenomena in a system with two parallel exo-and endothermal reactions. Dokl. USSR Acad. Sci. **261**(2), 392 (1981)
88. Meinkoehn, D.: Metal particle ignition and oxide layer instability. In: Borisov, A., Frolov, S., Kuhl, A. (eds.) Progress in Combustion and Detonation, pp. 180–181. Torus, Moscow (2004)
89. Ranz, W.E., Marshall, W.R., Jr.: Evaporation from drops, part I. Chem. Eng. Prog. **48**(3), 141–146 (1952)
90. Avdeev, K.A., Frolov, F.S., Frolov, S.M.: Effect of transient heat transfer on metal particle ignition. In: Roy, G., Frolov, S., Sinibaldi, J. (eds.) Pulsed and Continuous Detonations, pp. 72–83. Torus, Moscow (2006)
91. Avdeev, K.A., Frolov, F.S., Frolov, S.M., Basara, B.: Effect of transient heat transfer on metal particle ignition. In: Hanjalic, K., Nagano, Y., Jakirlic, G. (eds.) Turbulence, Heat and Mass Transfer, vol. 5, pp. 581–584. Begell House, New York-Wallingford (UK) (2006)

92. Gilmore, R.: Catastrophe Theory for Scientists and Engineers. Wiley-Interscience, New York (1981)
93. Fedorov, A.V.: Numerical and analytical study of magnesium particle ignition. Combust. Explos. Shock Waves **32**(1), 64–72 (1996)
94. Merzhanov, A.G.: Thermal theory of metal particle ignition. AIAA J. **13**(2), 209–214 (1975)
95. Grigor'ev, Yu.M., Vakina, Z.G.: Critical ignition conditions for metals with a logarithmic oxidation law. Combust. Explos. Shock Waves **15**(1), 51–53 (1979)
96. Alekseeva, T.I., Gurevich, M.A., Ozerov, E.S.: Ignition of an aluminum particle. Tr. Leningr. Politekh. Inst. **280**, 98–106 (1967)
97. Gurevich, M.A., Ozerov, E.S., Yurinov, A.A.: Effect of an oxide film on the inflammation characteristics of aluminum. Combust. Explos. Shock Waves **14**(4), 448–451 (1978)
98. Gurevich, M.A., Ozerova, G.E., Stepanov, A.M.: Heterogeneous ignition of an aluminum particle in oxygen and water vapor. Fiz. Goreniya Vzryva **6**(3), 326–335 (1970)
99. Friedman, R., Macek, A.: Ignition and combustion of aluminum particles in hot ambient gases. Combust. Flame **6**, 9–19 (1962)
100. Pokhil, P.F., Belyaev, A.F., Frolov, Yu.V., et al.: Combustion of Powdered Metals in Active Media. Nauka, Moscow (1972)
101. Boiko, V.M., Lotov, V.V., Papyrin, A.N.: Ignition of gas suspensions of metallic powders in reflected shock waves. Combust. Explos. Shock Waves **25**(2), 193–199 (1989)
102. Gurevich, M.A., Lapkina, K.I., Ozerov, E.S.: Limiting ignition conditions of an aluminum particle. Fiz. Goreniya Vzryva **6**(2), 172–176 (1970)
103. Fedorov, A.V., Kharlamova, Yu.V.: Ignition of an aluminum particle. Combust. Explos. Shock Waves **39**(5), 544–547 (2003)
104. Grigor'ev, Yu.M., Gal'chenko, Yu.A., Merzhanov, A.G.: Investigation of the rate of the high-temperature reaction between aluminum and oxygen using the ignition method. Combust. Explos. Shock Waves **9**(2), 162–167 (1973)
105. Gear, C.W.: The automatic integration of ordinary differential equations. Comput. Struct. **20**(6), 915–920 (1985)
106. Afanasieva, K.A., Levin, V.A.: Ignition of aluminum particles behind detonation and explosion waves. Chem. Phys. Rep. **3**(9), 1328–1332 (1984)
107. Fedorov, A.V., Tetenov, E.V., Veyssiere, B.: Dynamics and ignition of metal particles dispersed in atmosphere at a real explosion. Preprint no. 6–90. Institute of Theoretical and Applied Mechanics of the Siberian Branch of the Russian Academy of Sciences, Novosibirsk (1990)
108. Boiko, V.M., Papyrin, A.N.: On the ignition of magnesium particles behind reflected shock waves. In: Proceedings VIII All-Union Symposium Combustion and Explosion, pp. 65–68, Chernogolovka, 13–17 Oct 1986
109. Rosenband, V.: Thermo-mechanical aspects of the heterogeneous ignition of metals. Combust. Flame **137**(3), 366–375 (2004)
110. Yanenko, N.N., Soloukhin, R.I., Fomin, V.M., et al.: Supersonic Two-Phase Flows in Conditions of the Particles Velocity Non-Equilibrium. Nauka, Novosibirsk (1980)
111. Zubarev, V.N., Kozlov, A.D., Kuznetsov, V.M., et al. Thermophysical properties of technically important gases. Reference Book, p. 232. Energoatomizdat, Moscow (1989)

112. Fedorov, A.V.: Ignition of gaseous suspensions in an interacting continuum regime. Combust. Explos. Shock Waves **34**(4), 418–425 (1998)
113. Medvedev, A.E., Fedorov, A.V., Fomin, V.M.: Ignition of metal particles in high-temperature flow behind the shock wave. Preprint no. 33. Institute of Theoretical and Applied Mechanics of the Siberian Branch of the Russian Academy of Sciences Siberian Branch, Novosibirsk (1981)
114. Fedorov, A.V., Fomin, V.M.: Modeling of detonation flows in reacting gas-particle mixtures. In: Borisov, A., Frolov, S., Kuhl, A. (eds.) Progress in Combustion and Detonation, pp. 329–330. Torus, Moscow (2004)
115. Fedorov, A.V., Fomin, V.M.: Numerical study of flows of reacting composite mixtures. J. Appl. Mech. Tech. Phys. **40**(2), 300–307 (1999)
116. Fedorov, A.V., Gosteev, Yu.A.: A numerical study of ignition of magnesium samples in spherical and cylindrical symmetry. In: Proceedings 16th International Colloquium on the Dynamics of Explosions and Reactive Systems, pp. 299–302. AGH, Cracow (1997)
117. Gosteev, Yu.A., Fedorov, A.V.: Ignition of a cloud of metal particles in the continuum regime I. Adiabatic flow. Combust. Explos. Shock Waves **35**(5), 493–500 (1999)
118. Gosteev, Yu.A., Fedorov, A.V.: Ignition of a cloud of metal particles in the continuum regime. II. Nonadiabatic flow. Combust. Explos. Shock Waves **35**(6), 684–689 (1999)
119. Gosteev, Y.A., Fedorov, A.V.: Mathematical study of thermal explosion of a magnesium particle with allowance for metal evaporation. Combust. Explos. Shock Waves **34**(2), 151–158 (1998)
120. Wierzba, A.: Deformation and breakup of liquid drops in a gas stream at nearly critical Weber numbers. Exp. Fluids **9**(1–2), 59–64 (1990)
121. Gelfand, B.E., Gubin, S.A., Kogarko, S.M.: Specific features of the breakup of viscous liquid drop. Eng. Phys. J. **25**(3), 467 (1973)
122. Olim, M., Igra, O., Mond, M., Ben-Dor, G.: A general attenuation law of planar shock waves propagating into dusty gases. In: Groenig, H. (ed.) Shock Tubes and Waves, pp. 217–225. HI, Aachen (1987)
123. Simpkins, P.G., Bales, E.L.: Water-drop response to sudden accelerations. J. Fluid Mech. **55**(4), 629–639 (1972)
124. Boiko, V.M., Papyrin, A.N., Poplavskii, S.V.: Dynamics of droplet breakup in shock waves. J. Appl. Mech. Tech. Phys. **28**, 263–269 (1987)
125. Wadewitz, A., Specht, E.: Limit value of Nusselt number for particle of different shape. Int. J. Heat Mass Transfer **44**, 967–975 (2001)
126. Gordon, G.D.: Mechanism and speed of breakup of drops. J. Appl. Phys. **30**, 1759 (1959)
127. Volynskii, M.S., Lipatov, A.S.: Deformation and breakup of drops in gas flow. Eng. Phys. J. **18**(5), 838 (1970)
128. Davidson, V.E.: On drop deformation in gas flow. In: Belyaev, N.M., et al. (eds.) Jets and Flow in Tubes, pp. 3–35, Dnipropetrovsk(1974)
129. Detkovskii, D.A., Frolov, S.M.: Model of the deformation of a liquid droplet in a gas flow. J. Appl. Mech. Tech. Phys. **35**(6), 911–919 (1994)
130. O'Rourke, P.J., Amsden, A.A.: The TAB method for numerical calculation of spray droplet breakup. SAE Pap. 872089 (1987)
131. Borisov, A.A., Gelfand, B.E., Gubin, S.A., et al.: Detonation reaction zone in two-phase mixtures. Combust. Explos. Shock Waves **6**, 327–336 (1970)
132. Zhdan, S.A.: Calculation of a spherical heterogeneous detonation. Combust. Explos. Shock Waves **12**(4), 586–594 (1976)

133. Eidelman, S., Burkat, A.: Evolution of a detonation wave in a cloud of fuel droplets. I – influence of igniting explosion. AIAA J. **18**(9), 1103–1109 (1980)
134. Burkat, A., Eidelman, S.: Evolution of a detonation wave in a cloud of fuel droplets. II – influence of fuel droplets. AIAA J. **18**(10), 1233–1236 (1980)
135. Sichel, M.: In: Oran, E.S., Boris, J.P. (eds.) Numerical Approaches to Combustion Modeling. Numerical modeling of heterogeneous detonations. Progress in Astronautics and Aeronautics, vol. 135, pp. 447–458. American Institute of Aeronautics and Astronautics, New York (1991)
136. Gubin, S.A., Sichel, M.: Calculations of the detonation velocity of a mixture of liquid fuel droplets and a gaseous oxidizer. Combust. Sci. Technol. **17**(3–4), 109–111 (1977)
137. Borisov, A.A., Gelfand, B.E., Gubin, S.A, et al.: On drop deformation in the reaction zone of two-phase detonation. J. Appl. Mech. Tech. Phys. **5**, 39 (1970)
138. Borisov, A.A., Gelfand, B.E., Gubin, S.A., et al.: The reaction zone of two-phase detonations. Astronaut. Acta **15**, 411 (1970)
139. Zhdan, S.A.: Calculation of heterogeneous detonation taking into account deformation and breakdown of fuel droplets. Combust. Explos. Shock Waves **13**(2), 217–221 (1977)
140. Voronin, D.V., Zhdan, S.A.: Calculation of heterogeneous detonation initiation for a hydrogen-oxygen mixture in an explosion tube. Combust. Explos. Shock Waves **20**(4), 461–465 (1984)
141. Prakash, S., Sirignano, W.A.: Liquid fuel droplet heating with internal circulation. J. Heat Mass Transfer **21**, 885–895 (1978)
142. Smetanyuk, V.A., Frolov, S.M.: Hydrocarbon fuel drop vaporization and combustion. III: drop heating in gas flow with regard for internal liquid circulation. Khim. Fiz. **23**(7), 40 (2004)
143. Helenbrook, B.T., Edwards, C.F.: Quasi-steady deformation and drag of uncontaminated liquid drops. Int. J. Multiphase Flow **28**(10), 1631–1657 (2002)
144. Frolov, S.M., Smetanyuk, V.A.: Heat and mass transfer of a drop with gas flow. Khim. Fiz. **25**(4), 42 (2006)
145. Frolov, S.M., Frolov, F.S., Basara, B.: Mathematical model for transient droplet vaporization. In: Roy, G., Frolov, S., Starik, A. (eds.) Nonequilibrium Processes. Combustion and Detonation, vol. 1, pp. 179–193. Torus, Moscow (2005)
146. Dukowicz, J.K.: Quasi-steady droplet phase change in the presence of convection. Informal report LA7997-MS. Los Alamos Science Laboratory, Los Alamos (1979)
147. Liu, A.B., Mather, D., Reitz, R.D.: Modeling the effects of drop drag and breakup on fuel sprays. SAE Pap. 930072 (1993)
148. Clift, R., Grace, J.R., Weber, M.E.: Bubbles, Drops and Particles. Academic, New York (1978)
149. Frolov, S.M., Posvianskii, V.S., Basevich, V.Ya., et al.: Hydrocarbon fuel drop vaporization and combustion. II: nonempirical model of drop vaporization with regard for multicomponent diffusion. Khim. Fiz. **23**(4), 75 (2004)
150. Pilch, M., Erdman, C.: Use of breakup time data and velocity history data to predict the maximum size of stable fragments for acceleration-induced breakup of a liquid drop. Int. J. Multiphase Flow **13**, 741–757 (1987)
151. Joseph, D.D., Belanger, J., Beavers, G.S.: Vaporization of a liquid drop suddenly exposed to a high-speed airstream, July 15, 2003, http://www.aem.umn.edu/research/Aerodynamic_Breakup/

152. Reinecke, W.G., Waldman, G.D.: A study of drop breakup behind strong shocks with applications to flight. Technical report SAMSO-TR-70142. Avco Systems Division, Wilmington, MA (1970)
153. Frolov, S.M., Basevich, V.Ya., Posvianskii, V.S., et al.: Hydrocarbon fuel drop vaporization and combustion. IV: drop vaporization with regard for spray effects. Khim. Fiz. **23**(7), 49 (2004)
154. Frolov, S.M., Basevich, V.Ya., Belyaev, A.A., et al.: Modeling of drop vaporization and combustion with regard for spray effects. In: Roy, G.D., Frolov, S.M., Starik, A.M. (eds.) Combustion and Pollution: Environmental Effect, pp. 117–132. Torus, Moscow (2005)
155. Basevich, V.Y., Belyaev, A.A., Evlampiev, A.V., et al.: Hydrocarbon fuel drop vaporization and combustion. I: nonempirical model of single-component drop vaporization. Khim. Fiz. **21**(3), 58 (2002)
156. Yang, J.-R., Wong, S.C.: On the suppression of negative temperature coefficient (NTC) in autoignition of n-heptane droplets. Combust. Flame **132**(3), 475–491 (2003)
157. Frolov, S.M., Basevich, V.Ya., Posvianskii, V.S.: Limiting drop size and prevaporization degree required for spray detonation. In: Roy, G.D., Frolov, S.M., Shepherd, J. (eds.) Application of Detonation to Propulsion, pp. 110–119. Torus, Moscow (2004)
158. Basevich, V.Ya., Frolov, S.M., Posvianskii, V.S.: Existance conditions for stationary heterogeneous detonations. Khim. Fiz. **24**(7), 60 (2005)
159. Basevich, V.Ya., Belyaev, A.A., Frolov, S.M.: Overall kinetic mechanisms for modeling turbulent reactive flows. Part I: main chemical process of heat release. Chem. Phys. Rep. **17**(9), 112 (1998)
160. Basevich, V.Ya., Belyaev, A.A., Frolov, S.M.: Overall kinetic mechanisms for modeling turbulent reactive flows. Part II: nitrogen oxide formation. Chem. Phys. Rep. **17**(10), 71 (1998)
161. Evlampiev, A.V., Frolov, S.M., Basevich, V.Ya., et al.: Overall kinetic mechanisms for modeling turbulent reactive flows. Part IV: diffusion combustion. Chem. Phys. Rep. **20**(11), 21 (2001)
162. Basevich, V.Ya., Belyaev, A.A., Brandstaetter, W., et al.: Kinetic scheme for modeling autoignition of iso-octane and n-heptane blends in air. Combust. Explos. Shock Waves **30**(6), 15 (1994)
163. Basevich, V.Ya., Frolov, S.M., Posvianskii, V.S., et al.: Low-temperature drop autoignition. Khim. Fiz. **24**(5), 71 (2005)
164. Takei, M., Kobayashi, H., Niioka, T.: Ignition experiment of a blended-fuel droplet in a microgravity field. Int. J. Microgravity Res. Appl. Microgravity Sci. Technol. **VI**(3), 184–187 (1993)
165. Niioka, T., Kobayashi, H., Mito, D.: Ignition experiments on droplet array in normal and microgravity environments. In: Proceedings IUTAM Symposium Mechanics and Combustion of Droplets and Sprays Proceedings, pp. 367–377, Tainan (1994)
166. Roy, G.D., Frolov, S.M., Borisov, A.A., Netzer, D.W.: Pulse detonation propulsion: Challenges, current status, and future perspective. Prog. Energy Combust. Sci. **30**, 545–672 (2004)
167. Borisov, A.A., Komissarov, P.V., Kulikov, A.V., et al.: Kinetics of heat release in heterogeneous mixtures. Chem. Phys. Rep. **17**(3), 49 (1998)

168. Frolov, S.M., Scripnik, A.A., Kavtaradze, R.Z.: Modeling of diesel spray ignition. In: Roy, G.D., Frolov, S.M., Starik, A.M.: Combustion and Atmospheric Pollution, pp. 220–227. Torus, Moscow (2003)
169. Scripnik, A.A., Frolov, S.M., Kavtaradze, R.Z., et al.: Modeling of autoignition in liquid fuel spray. Khim. Fiz. **23**(1), 54 (2004)
170. Matsko, A.M., Kopeika, K.M., Polishchuk, D.I., et al.: Effect of external heat transfer on the critical conditions for ignition of gaseous suspension of magnesium particles. Phys. Aerodispersed Syst. **20**, 53–56 (1980)
171. Atthasit, A., Doue, N., Biscos, Y., et al.: Influence of drop concentration on the dynamics and evaporation of a monodisperse stream of drops in evaporation regime. In: Roy, G.D., Frolov, S.M., Starik, A.M. (eds.) Combustion and Atmospheric Pollution, pp. 214–219. Torus, Moscow (2003)